Multiphysics Modeling and Reliability of Magnetic Components in Power Electronics Applications

Shen, Zhan

Publication date:
2020

Document Version
Publisher's PDF, also known as Version of record

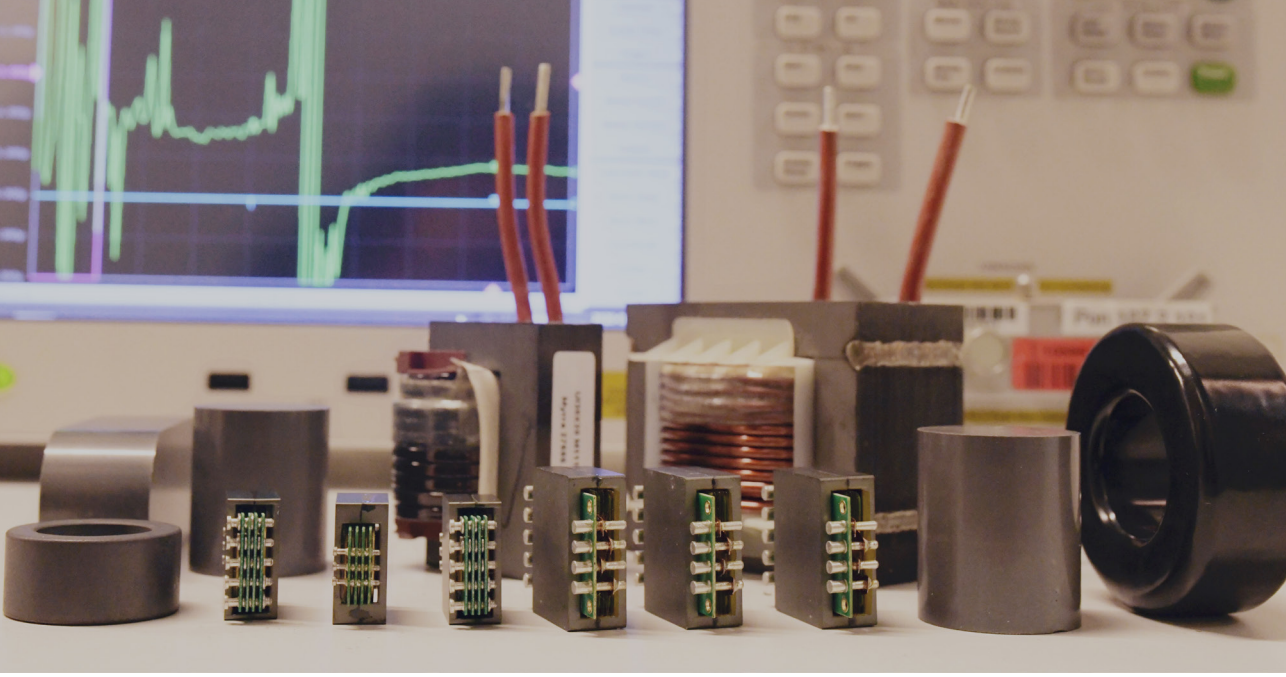

MULTIPHYSICS MODELING AND RELIABILITY OF MAGNETIC COMPONENTS IN POWER ELECTRONICS APPLICATIONS

BY
ZHAN SHEN

DISSERTATION SUBMITTED 2020

AALBORG UNIVERSITY
DENMARK

Multiphysics Modeling and Reliability of Magnetic Components in Power Electronics Applications

Ph.D. Dissertation

Zhan Shen

Dissertation submitted Feb., 2020

Dissertation submitted: Feb., 2020

PhD supervisor: Prof. Huai Wang
Aalborg University, Denmark

Assistant PhD supervisor: Prof. Frede Blaabjerg
Aalborg University, Denmark

PhD committee: Associate Professor Sanjay Kumar Chaudhary (chair.)
Aalborg University

Professor William Gerard Hurley
National University of Ireland

Associate Professor Qiang Li
Virginia Polytechnic Institute and State University

PhD Series: Faculty of Engineering and Science, Aalborg University

Department: Department of Energy Technology

ISSN (online): 2446-1636
ISBN (online): 978-87-7210-600-7

Published by:
Aalborg University Press
Langagervej 2
DK – 9220 Aalborg Ø
Phone: +45 99407140
aauf@forlag.aau.dk
forlag.aau.dk

Printed in Denmark by Rosendahls, 2020

Abstract

Magnetic components are critical devices in power electronics applications, which provide the function of galvanic isolation, filtering, energy storage, and energy transfer, etc. In emerging and future applications, power electronic magnetics may need to be designed to their electro-thermal limits to reduce the size and cost further. To do it confidently, more precise electromagnetic-thermal and reliability models are necessary for the decision making in the model-based design. The parameter shift of magnetic components is also a concern that could alter the operation points of the power electronic converters. So degradation modeling is also of interest, even if magnetic components have not reached the end-of-life. In recent decades, there is a lot of research on modeling. However, how to model power electronic magnetic components precisely considering reliability is still an open question.

To address this issue, this project proposes a number of models urgently demanded in the multiphysics field, and explores the degradation and reliability of power electronics magnetic components. The impedance and power loss modeling are firstly studied in both electric and magnetic fields. Then the thermal modeling is investigated to obtain the temperature distribution. Finally, a thermal Accelerated Lifetime Testing (ALT) of planar transformers is performed. The degradation mechanism is analyzed, and the lifetime model of planar transformers is proposed at the first time to the best knowledge.

In electric field modeling, the stray capacitance of inductors, which induces inrush charging current and high-frequency oscillations, is studied at first. The capacitance model considers the core/shield-related capacitance and is applicable for inductors with the grounded or floating core/shield. Moreover, the criteria to determine the core/shield-related capacitance is also investigated. Finally, the stray capacitance of the compact orthocyclic winding is studied, and its difference with the normal winding is also compared.

In high-density and high-frequency applications, special winding configurations, e.g., the partial layer winding and the orthocyclic winding, require precise magnetic field modeling. Omission or inappropriate calculation of winding parameters leads to additional losses, circuit oscillations, and even abnormal operations. This project models the power loss of the special wind-

ings and the leakage inductance of the orthocyclic winding. Case studies are provided to verify those models and investigate their difference compared with the normal winding.

The temperature distribution of planar magnetics is usually uneven, and the calculation of hot-spot temperature is essential in the thermal modeling and optimization. To obtain the temperature of each print circuit board winding and the core, a thermal network is proposed considering the thermal coupling between them and the ambient. Using thermal Computational Fluid Dynamics (CFD) simulations or analytical formulas, the parameters of the network are calculated. Based on that, a thermal impedance matrix is obtained, which can be further integrated in the design algorithm conveniently.

Normally, magnetics are regarded relatively more reliable compared with other devices in power electronics. However, as the increase of power density, operating frequency, and temperature of magnetics, there are degradation reports of magnetic core and insulation material, while a systematic study for the whole magnetic component is still missing. This project conducts the research on the reliability of power electronic magnetics. Accelerated Lifetime Testing (ALT) of planar transformers is performed, and rich data during the thermal degradation process are recorded, e.g., the primary inductance and resistance, leakage inductance, short-circuit resistance, and inception voltage in partial discharge tests. Based on the degradation results, the likely failure mechanisms are analyzed, and the lifetime model of the tested planar transformers is finally obtained.

The proposed multiphysics models have been verified by simulation and experimental results in six case studies, and the reliability model is also based on degradation testing results. Combining the existing and proposed multiphysics models, the conventional electro-magnetic-thermal design procedure of magnetic components is extended by considering the stray capacitance of inductors, parasitics of special winding configurations, and temperature distribution of planar transformers. Finally, with the degradation and lifetime model, a reliability-oriented design and optimization procedure can be proposed in the future, which will contribute to reducing the design margin, product cost, and system-level wear-out failure of magnetic components in power electronics applications.

Resumé

Magneter er de kritiske komponenter i effektelektronik. I nye og fremtidige applikationer kan det være nødvendigt, magnetiske komponenter kan muligvis være designet til deres elektro-termiske grænser for at reducere størrelsen og omkostningerne yderligere. For at gøre det med sikkerhed er det nødvendigt med mere præcise elektromagnetiske-termiske og pålidelighedsmodeller for beslutningstagningen i det modelbaserede design. Parameterforskyvningen af magnetiske komponenter er også et problem, der kan ændre driftspunkterne for de elektroniske strømkonvertere. Så nedbrydningsmodellering er også af interesse, selvom magnetiske komponenter ikke har nået slutningen af levetiden.

For at tackle dette problem, undersøges i dette projekt ved multi-fysik modellering, magneters indflydelse på pålidelighed i effektelektronik. Impedans- og tabsmodelleringen undersøges først i både elektriske og magnetiske felter, og derefter undersøges problemerne med termisk kobling og netværksmodellering for beregning af temperaturfordelingen og til sidst udføres den termiske nedbrydningstest af planar magnets, nedbrydningsmekanismen analyseres, og levetidsmodellen foreslås første gang.

Ved elektrisk feltmodellering undersøges først induktansers stray capacitance, der inducerer inskoblingsstrømstød og højfrekvenssvingninger. Kapacitansmodellen overvejer core/shield relaterede kapacitans og gælder for induktorer med jordede eller flydende kerne. Derudover undersøges også kriterierne for core/shield relateret kapacitet. Endelig studeres stray capacitance i den orthocykliske vikling og sammenlignes med den normale ortogonale viklingskonfiguration, som er af referenceværdien for viklingsdesignet.

I applikationer med høj energidensitet og høj frekvens er der behov for specielle viklingskonfigurationer, fx delvis lagvikling og den ortocykliske vikling. Udeladelse eller upassende beregning af viklingsparametrene fører til yderligere tab, kredsløbsoscillationer og endda fejlfunktion. Dette projekt studerer den ækvivalente vekselstrømsmodstand for flere specielle viklinger i magnetfelter. Der foreslås også en modificeret formel for lækageinduktansen til den ortocykliske vikling. Der udarbejdes case studies for at verificere disse ligninger og undersøge deres forskel sammenlignet med den normale

vikling.

Temperaturfordelingen er ofte uens i planar magnets og beregningen af hot-spot-temperaturen er afgørende i termisk modellering og optimering. For at beregne temperaturen på hvert printkredsløb og kerne foreslås et termisk netværk baseret på den termiske kobling mellem dem og omgivelserne. Med flere CFD –simuleringer opnås ækvivalent diagrammer. Den termiske impedansmatrix opnås, som yderligere kan bruges til den modelbaserede termiske design og iterationsoptimeringsprocedure.

Magnetkomponenter betragtes normalt som relativt pålidelige sammenlignet med andre enheder i elektroniske convertere. Med stigningen i effekttæthed, driftsfrekvens og temperatur rapporteres der dog om termisk nedbrydning med hensyn til magnetisk kerne- og isoleringsmateriale, mens en systematisk undersøgelse fra systemniveau for effektelektronik stadig mangler. Dette projekt udførte den første Accelerated Lifetime Testing (ALT) af planar magnets med stor mængde registrerede data under den termiske nedbrydningsproces, for eksempel den primære induktans og modstand, lækageinduktans, kortslutningsresistens, startspænding i delvise udladningstest osv. Baseret på nedbrydningsresultaterne analyseres de sandsynlige fejlkilder. Med antagelsen af livstidskriterierne: primær induktionsfaldsprocent opnås den termiske relaterede levetidsmodel for den testede planar transformer.

De multifysiske modeller, der er foreslået i dette projekt, er verificeret ved simulering og eksperimenter, og pålidelighedsmodellen er også baseret på resultaterne af nedbrydningstest. Ved at kombinere de eksisterende og foreslåede multifysiske modeller udvides den konventionelle effektelektroniske designprocedure, ved at overveje stray capacitance for induktorer, specielle viklingskonfigurationer og temperaturfordeling i planar magnets. Endelig kan man med pålidelighedsmodellen foreslå et pålidelighedsorienteret design og optimering af effektelektronik i fremtiden, hvilket kan reducere designmargenen, produktomkostningerne og nedbrydning af magneter på systemniveau.

Preface

This Ph.D. thesis is a summary of the Ph.D. project "Design and Reliability of Magnetic Components of Power Electronic Converters" conducted in Center of Reliable Power Electronics (CORPE), Department of Energy Technology, Aalborg University, Denmark.

Firstly, I would also like to express the deepest gratitude to my supervisor, Professor Huai Wang, for his professional and patient guidance. I greatly appreciate his support through technical discussions, instructive advice, and precious opportunities for both my research and career. I do believe this support will be of great treasure for my future life. Likewise, I would like to thank my co-supervisor, Professor Frede Blaabjerg. He provides me enthusiasm guidance and outstanding opportunity and impacts me with his open-mindedness and earnestness during my whole academic career.

My special gratitude goes to Prof. David J. Perreault for his kindness and inspiring discussion during my study abroad in Massachusetts Institute of Technology (MIT), USA. Also, thanks to Dr. Alex J. Hanson and the members of the "magnetic team" for the inspiration and fun in the discussion. Many thanks to the colleagues at MIT and Northeastern University for their hospitality in my life in Boston.

I would like to express my gratitude to all my local and external colleagues at the Department of Energy Technology, Aalborg University, for their fruitful discussion and support. Special thanks go to Dr. Yanfeng Shen, Dr. Qian Wang, Dr. Haoran Wang, Mr. Bochen Liu, and Dr. Zian Qin for their support in this project in every aspect. I am also grateful to my colleagues and old friends from Southeast University and RWTH Aachen University.

Finally, my most sincere gratitude goes to my parents. Your endless encouragement and love made me who I am today.

Zhan Shen
Aalborg University, February 7, 2020

Contents

Report

Chapter 1

Introduction

1.1 Background and Motivation

1.1.1 Magnetic Components in Power Electronics Applications

Power electronics play a more and more critical role in the generation, transmission, and distribution of traditional and renewable energy, and also the efficient use of electricity. Magnetic components, e.g., inductors and transformers, are key components in modern power electronics systems [1–3]. They provide the function of energy storage and transfer, and are widely adopted in various applications, e.g., isolation [4–6], filters [7, 8], planar and integrated magnetics [9–12], wireless power transfer [13, 14], integrated point-of-load (POL) converters [15, 16].

Emerging magnetic materials help magnetic components to increase the operating frequency and obtain significant benefits, e.g., volume, cost, and weight reduction, as in Fig. 1.1 [5, 6]. Theoretical study proves that even in Very High Frequency (VHF) range, i.e., 30-300 MHz, there are opportunities to further decrease the size of magnetics with low-permeability radio-frequency materials [17, 18]. On the other hand, the increase of frequency and decrease of size bring thermal and insulation challenges [3, 19]. Those issues may affect the reliability of magnetic components, especially in outdoor and severe applications, e.g., photovoltaics (PV), offshore and onshore wind farms, automotive, aeronautics, and astronautics.

From a survey of 56 effective responses from different industry companies, 6% of companies consider that inductors are the most reliability-critical components in their power electronics products [20]. Nevertheless, there is limited systematic reliability study of power electronic magnetic components in literature. The state-of-art research mainly focuses on the sub-component level, e.g., magnetic cores [21–31], insulation materials [32–34], and print-

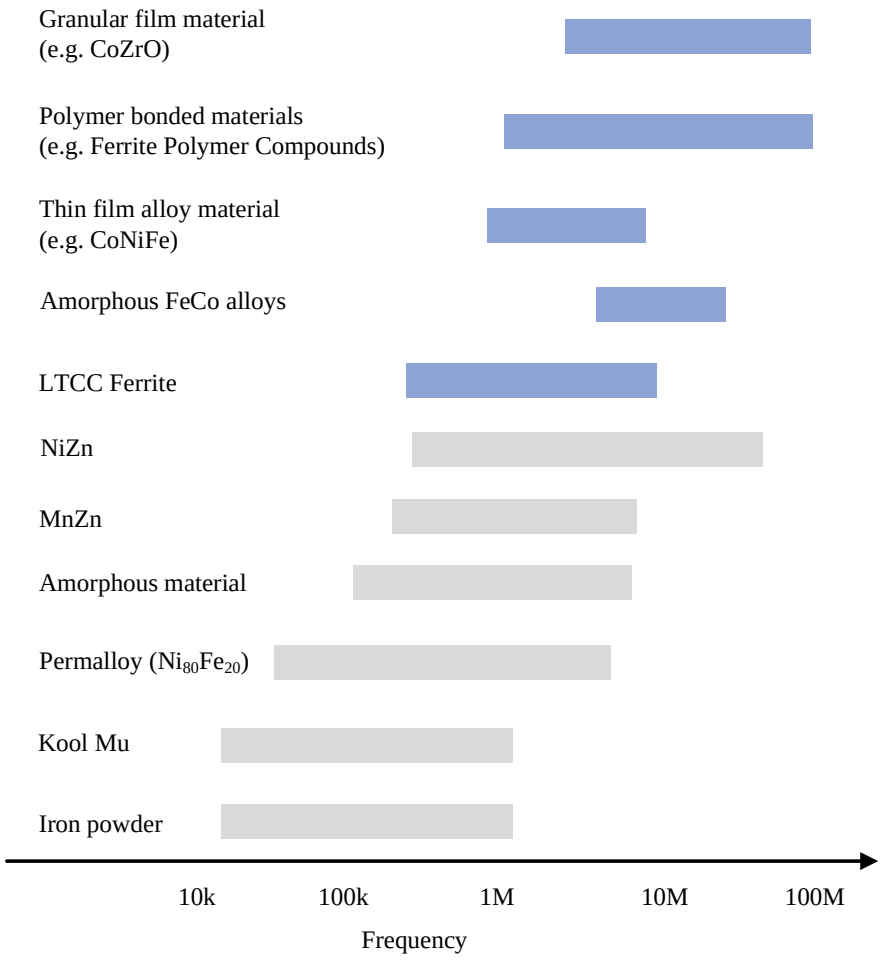

Fig. 1.1: Advances of magnetic materials and their typical frequency range. The gray color indicates the commercial materials and the light blue color indicates the emerging materials. [16]

circuit-boards [35–38]. The reliability research on the power transformers [39–43] and electric machines [44–49] is of reference value. However, they cannot be applied for magnetic components in power electronics applications directly.

Moreover, even though magnetic components are widely considered relatively more reliable than power semiconductor devices and capacitors, the parameter shifts due to wear-out may alter the operation points along the operation time even before they reach the end-of-life. The estimation of such parameter shift (e.g., inductance drop) requires the investigation of the wear-

out mechanisms and degradation modeling, even there is no critical failure of magnetic components within the service lifetime of power electronic converters.

Finally, with the trend of increasing operating frequency and power density, future power electronic magnetic components may need to be designed to their electro-magnetic-thermal limits. New challenges emerge, which require more precise multiphysics and lifetime models to support the design margin reduction.

1.1.2 Project Motivation

Most power electronics magnetics are customized devices, and their performances highly rely on precise modeling and robust design. Current cost pressure and future requirements from application fields bring new challenges [50, 51]:

- Magnetic components can contribute to reliability issues in power electronic systems;
- Even without critical failure, the parameters shift of magnetics during the degradation may also affect the circuit operation;
- Emerging applications (e.g., outdoor and severe applications) require extreme high reliable power electronic devices;
- The advances in wide-band-gap devices pushes up the switching frequency and enables the more and more compact design with competitive cost. It decreases the size, and also limits the loss, temperature, insulation, and reliability design margin. More precise models, i.e., electric field, magnetic field, thermal, and reliability models, are needed for the model-based design;
- Planar magnetics are preferred in high-frequency applications for its feature of low profile, low manufacturing cost, and high power density. However, those features also bring reliability challenges. Moreover, the print-circuit-board (PCB) windings are regarded more vulnerable than wiring windings, especially under thermal stresses;

Some of those challenges may not be critical issues to today's applications, and existing models may already be good enough for the design practice today. However, it is necessary to prepare for future challenges. This Ph.D. project is to study the corresponding multiphysics modeling, i.e., electric field, magnetic field, thermal, and degradation modeling of magnetic components in power electronics applications. Several critical modeling challenges are under urgent demand to be addressed, and therefore they are emphasized during the study.

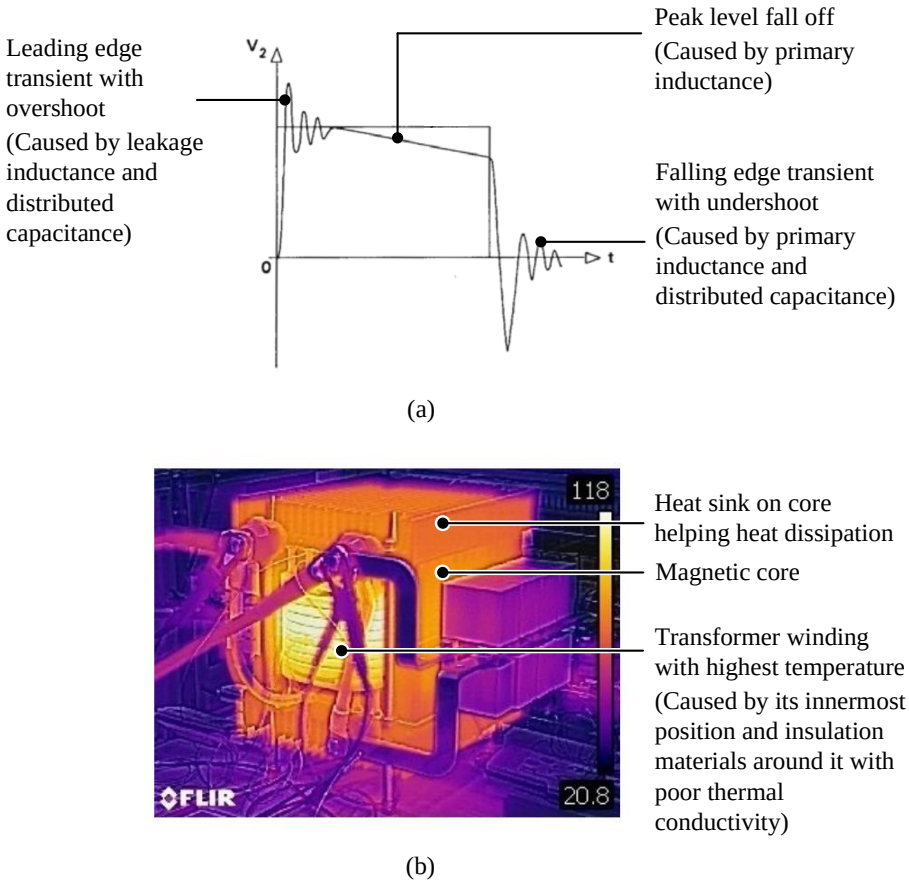

Fig. 1.2: Examples of the impacts of the transformer parasitics to their performance. (a) Transformer pulse response determined by its impedance. (b) Temperature distribution of a medium frequency transformer determined by its loss and thermal design. [52, 53]

The electric field modeling is for insulation stress and stray capacitance. The electrical stress is used in the insulation design, which is normally obtained through electric field simulations or empirical formulas. For novel or complex configurations, only the simulation is possible, which is adopted in this study. The stray capacitance induces current and voltage oscillations during transients, as illustrated in Fig. 1.2(a). It brings over-voltage problems to power devices and also generates additional losses [54]. Current models consider the stray capacitance of the winding [55–63] and the capacitance between the one-layer winding and the core [64–66]. In future power electronics applications, the switching frequency increases, which is more and more

close to the oscillation frequency induced by the stray capacitance. To avoid abnormal operations and improve the circuit performance, a more precise capacitance model considering the core, grounding, and different winding configurations is necessary.

The magnetic field modeling obtains the losses, i.e., core and winding loss, and inductance, e.g., the primary main inductance and the leakage inductance. Core loss is one of the primary heat sources of magnetics. It is non-linear, unevenly distributed, and also varies with core structure and winding configurations. The classic empirical Steinmetz equation [67] is based on the curve fitting of experimental results in sinusoidal waveforms scenarios. Current research modifies and extends it to arbitrary waveforms [68–74], while the Improved Generalized Steinmetz equation (iGSE) is widely accepted among them [70]. For future applications, those models are still applicable, and the challenges are in the measurement [18, 75]. The winding loss is another heat source. The winding is normally at the highest temperature because of the poor thermal conductivity of insulation materials around it, as illustrated in Fig. 1.2(b). Therefore the winding loss modeling is essential for temperature calculation and control. The inductance of magnetics are important to shape the current and voltage waveform (c.f. 1.2(a)), and provide the soft-switching elements to certain circuits [4]. It is also to be studied in this project.

To control the temperature of magnetics, precise thermal modeling is essential. The core and winding are the major heat sources, as in Fig. 1.2(b). Moreover, the insulation is regarded as the most vulnerable sub-component under thermal stress. A thermal network modeling, including all those subcomponents, is necessary. Further, the planar transformers are preferred in high frequency applications. They are with severe thermal issues compared with wiring magnetics due to its high energy density and relative more vulnerable print-circuit-board (PCB) winding. Therefore they are chosen as the focus of the thermal study.

With all the challenges now and in the future, multiphysics modeling is essential, especially for those discussed with urgent demands.

Furthermore, there are also more and more reliability issues in power electronic magnetic components, as exampled in Fig. 1.3. In (a), the failure in medium frequency transformer results from the poor insulation and leads to an inner short-circuit. In (b), the print circuit board (PCB) and the insulation layer degrades in the high-temperature storage reliability test. In this project, the planar transformer is used in the reliability case study due to its higher-density requirements and higher-temperature stresses compared with other wiring magnetics. The reliability study of line-frequency power transformers and electrical machines are normally focusing on the insulation system [42, 43, 45, 46]. So the insulation may also be a challenge for planar transformers. Also, the reliability of the emerging high-frequency core materials

(a)

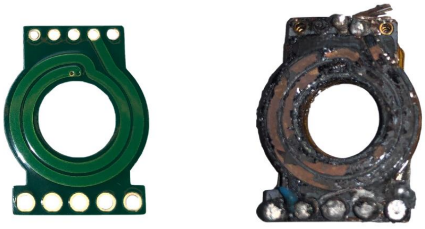

New Aged

Print-circuit-board (PCB) winding

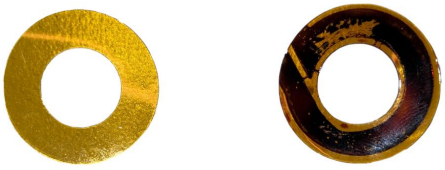

New Aged

Insulation layer

(b)

Fig. 1.3: Parts of a failed medium frequency transformer (a) and comparison of new and aged planar transformer sub-components (b). [76]

is under investigation. Moreover, the PCB winding in planar transformers is regarded as less reliable compared with conventional insulation wires. The impact of the PCB degradation on planar magnetics is still not clear. Furthermore, the shift of parasitic parameters (e.g., inductance drop and resistance raise) during the service life may alter the operation point and cause localized overheat problems. So even though the planar transformer does not reach the end-of-life, the study on the degradation process is also of significance value. Those sub-issues should be investigated in order to prepare for future power electronics requirements and challenges.

1.2 Project Objectives and Limitations

1.2.1 Study Questions

To address the challenges in the high frequency and high density power electronic magnetic components, a general question is raised in this Ph.D. project:

- Q0: How to model magnetic components precisely in power electronics considering the reliability during the service life?

starting from the general question, several sub-questions are addressed in the study:

- Q1: How to model the parasitics in power electronic magnetics?

  In general, the parasitics include the stray capacitance in the electric field modeling, and core loss, winding loss, and inductance in the magnetic field modeling.

  Future power electronics goes to even higher frequency, while there is an urgent demand for a more precise stray capacitance model considering necessary aspects, e.g., the core, shield, grounding, winding placements.

  The iGSE model [70] for core loss is applicable to the existing and also emerging magnetic materials. It is adopted in this study directly. So core loss modeling is not emphasized in this project.

  Dowell's equation [77] is widely used for the resistance and leakage inductance of normal windings. However, it may not be applicable anymore for special windings configurations, e.g., the partial layer winding and orthocyclic winding. The partial layer winding is necessary to control the number of winding turns precisely, and the orthocyclic winding configuration frequently appears in round wire windings. More precise resistance and leakage inductance model are essential, especially with the design-to-limit requirements in the future.

- Q2: How to calculate the temperature distribution and hot-spot temperature of planar transformers?

  Compared with wiring magnetics, the planar transformer has a more compact structure and vulnerable PCB winding. So it is chosen as the focus in the thermal modeling study. The Computational Fluid Dynamics (CFD) simulation offers accurate results. However, it is time-consuming. Therefore, an accurate and generic thermal model, which is also easy to be implemented in a design algorithm, is needed.

- Q3: How to perform the degradation testing for planar transformers?

  Again, the planar transformer is chosen as the specimen in the degradation resting, due to its compact structure, relative vulnerable PCB winding, and limited design margin. Unlike the multiphysics modeling, the degradation modeling of power electronics magnetic components only relies on the degradation testing results, while no analytical and simulation method is available. Also, it is still not clear which parameter can be used as the degradation and end-of-life indicator. Therefore all possible parameters should be recorded.

- Q4: How to model the degradation and lifetime of the planar transformer, what is the degradation mechanism, and what is the end-of-life criteria?

  The end-of-life indicator and criteria should be determined as a first step, which highly depends on the application field requirements and the understanding of failure mechanisms. The choosing of a lifetime model also relies on the results of degradation analysis. Until now, a clear understanding and scientific consensus of those issues are not reached yet.

1.2.2 Objectives

To answer the selected research questions, this study defines four objectives in the electro-magnetic-thermal-reliability field:

- O1: Impedance and loss modeling of magnetics in the elector-magnetic field considering special winding configurations

  An improved stray capacitance model of the inductor considering the impact of the core, shield, and grounding will be investigated. The power loss models of the partial layer winding will also be studied. Moreover, the parasitic parameter models (stray capacitance, ac resistance, and leakage inductance) of the orthocyclic winding will be investigated by modifying existing models. The difference between the normal and orthocyclic windings will be compared to guide the design.

- O2: Thermal modeling of planar transformers considering the internal winding structure

  A thermal-network model will be proposed to calculate the temperature of each winding and core in the planar transformer. Several reasonable assumptions are made for the planar transformer with compact structure. A thermal matrix is extracted, which can be further implemented in the design procedure.

- O3: Long-term Accelerated Lifetime Testing (ALT) for power electronics magnetics

  The long-term ALT is essential for the degradation modeling of power electronics magnetic components. The thermal stress will be applied at the first step, and one type of planar transformers is used as the specimens. All possible parameters, which could indicate the degradation and become the end-of-life indicator, are tested and recorded during the degradation process. Those parasitics include the primary inductance and resistance, the leakage inductance, short-circuit resistance, and the inception voltage obtained in the partial discharge test.

- O4: Degradation analysis and lifetime modeling of power electronic magnetics

  Based on the ALT results, the likely degradation mechanism of the planar transformer can be studied. Currently, there is no consensus of the degradation indicator parameter and end-of-life criteria for the power electronic magnetics. Therefore, the assumed indicator and criteria are used, and a lifetime modeling procedure of planar magnetics is introduced and used in a case study.

1.2.3 Project Limitations

This Ph.D. project studies the multiphysics and reliability modeling of magnetic components in power electronics applications. There are several limitations:

- L1: Impedance and loss model studied in this work mainly focus on special windings techniques in wiring magnetics. In the high-frequency range, the impacts of the PCB winding are also important. However, they are not included.

- L2: The long-term ALT considers only the thermal stress. Other reliability stressors, e.g., voltage and humidity, are not investigated.

- L3: The degradation analysis is based on one type of samples in ALT, and there is no comprehensive corresponding research available in public-domain literature to our best knowledge. Therefore, the interpretation of the failure mechanisms are based on the limited information only, i.e., the parasitics change and optical observation. A further confirmation of the failure mechanisms requires advanced testing methods such as x-ray diffraction and secondary ion mass analysis, which may be done in the future.

1.3 List of Dissemination

The research dissemination during the Ph.D. study is shown below in the forms of journal papers and conference publications. Parts of them are used in the Ph.D. thesis, i.e., J1, J2, J3, J4, C1, C2, C3, and C4.

Journal Papers

J1. **Z. Shen**, H. Wang, Y. Shen, Z. Qin and F. Blaabjerg, "An Improved Stray Capacitance Model for Inductors" *IEEE Trans. Power Electron.*, vol. 34, no. 11, pp. 11153-11170, Nov. 2019.

J2. **Z. Shen** and H. Wang, "Parasitics of Orthocyclic Windings in Inductors and Transformers" *IEEE Trans. Power Electron.*, under review, 2020.

J3. **Z. Shen**, Z. Li, L. Jin, and H. Wang, "An Approximation Model of AC Resistance for Inductor and Transformer Windings with Partial Layers" *IEEJ Trans. Ind Appl.*, under review, 2020.

J4. **Z. Shen**, Q. Wang, and H. Wang, "Degradation Testing and Analysis of Planar Transformers" *IEEE Trans. Power Electron.*, under preparation, 2020.

- Y. Shen, H. Wang, **Z. Shen**, Y. Yang, and F. Blaabjerg, "A 1-MHz Series Resonant DC-DC Converter With a Dual-Mode Rectifier for PV Microinverters" *IEEE Trans. Power Electron.*, vol. 34, no. 7, pp. 6544-6564, July 2019.

Conference Papers

C1. **Z. Shen**, Z. Li, L. Jin, and H. Wang "An AC Resistance Optimization Method Applicable for Inductor and Transformer Windings with Full Layers and Partial Layers" in *Proc. IEEE APEC Exposit.*, pp. 2542–2548, Mar. 2017.

C2. **Z. Shen**, Y. Shen, B. Liu, and H. Wang "Thermal Coupling and Network Modeling for Planar Transformers" in *Proc. IEEE ECCE*, pp. 3527–3533, Sept. 2018.

C3. **Z. Shen**, Q. Wang, Y. Shen, and H. Wang, "First Observations in Degradation Testing of Planar Magnetics" in *Proc. IEEE APEC Exposit.*, pp. 1436-1443, Mar. 2019.

C4. **Z. Shen**, Q. Wang, and H. Wang, "Degradation Analysis of Planar Magnetics" in *Proc. IEEE APEC Exposit.*, accepted, Mar. 2020.

- **Z. Shen**, H. Wang, Y. Shen, Z. Qin and F. Blaabjerg, "Winding Design of Series AC inductor for Dual Active Bridge Converters" in *Proc. IEEE APEC Exposit.*, pp. 565–570, Mar. 2018.
- **Z. Shen**, Y. Shen, Z. Qin and H. Wang, "Modeling and Optimization of Orthocyclic Windings for Transformers in Dual Active Bridge Converters" in *Proc. IEEE ECCE Asia*, pp. 1925–1930, May 2018.
- H. Wang, H. Wang, and **Z. Shen**, "Reliability of Capacitors and Magnetic Components in Power Electronic Applications" in *Proc. Int. Conf. Integ. Power Electron. Sys.*, VDE, accepted, Mar. 2020.
- J. Yuan, **Z. Shen**, Y. Yang, A. Mostaan and F. Blaabjerg, "Design and Analysis of a Novel Trans-inverse DC-DC Converter" in *Proc. IEEE Wksp. Control Model. Power Electron.*, pp. 1-5, June 2019.

- Z. Qin, **Z. Shen**, F. Blaabjerg, and P. Bauer, "Modelling, Analysis and Mitigation of the Transformer Current Ringing in Dual Active Bridge Converters" in *Proc. IEEE ECCE*, pp. 650-655, Sept. 2018.
- Y. Shen, H. Wang, **Z. Shen**, Y. Yang, and F. Blaabjerg, "Series Resonant DC-DC Converter With Dual-Mode Rectifier for PV Microinverters" in *Proc. IEEE ECCE Asia*, pp. 1788–1792, May, 2018.
- Y. Shen, H. Wang, **Z. Shen**, F. Blaabjerg, and Z. Qin, "An Analytical Turn-on Power Loss Model for 650-V GaN eHEMTs" in *Proc. IEEE APEC Exposit.*, pp. 913–918, Mar. 2018.
- Z. Qin, **Z. Shen**, and F. Blaabjerg, "Modelling and Analysis of the Transformer Current Resonance in Dual Active Bridge Converters" in *Proc. IEEE ECCE*, pp. 4520-4524, Oct. 2017.

1.4 Thesis Outline

The outcomes during the Ph.D. period are documented in the Ph.D. thesis, which includes a report and selected publications. The report summarizes the research outcome during the Ph.D. project, while the selected publications include the published/submitted journal and conference articles. A brief illustration of their relationship is shown in Fig. 1.4.

The report in the thesis is to answer the general study question Q0, while each chapter studies the sub-questions (Q) and realize the sub-objectives (O). It follows the modeling procedure of the electrical field, magnetic field, thermal, and reliability, respectively, and proposes corresponding models in each field.

Chapter 1 is the introduction of the background, motivation, objectives to achieve, and limitations of this study. Chapter 2 discusses the electric field modeling for study question Q1 and objective O1, where the stray capacitance of inductors and orthocyclic windings are studied. In Chapter 3, the magnetic field modeling is described. According to Q1 and O1, the special winding configurations, i.e., partial layer winding and orthocyclic winding, are of significant impact to the precise loss and impedance modeling. So their winding loss and leakage inductance model are investigated. The thermal model in Chapter 4 calculates the temperature distribution of planar magnetics for Q2 and O2. Chapter 5 introduces the reliability research conducted in this project. The first section is to answer study question Q3 by reaching the objective O3: long-term Accelerated Lifetime Testing (ALT). With the test results, the second and third section performs the degradation analysis and the lifetime modeling for Q4 and O4. The last chapter concludes this report, where the contributions are summarized, and new research opportunities and challenges are also listed.

This thesis performs 6 case study in the electro-magnetic-thermal modeling research, and uses 24 of one kind planar transformers as the 7th reliability case study. The relevant case study number, proposed models, and prototype numbers are summarized in Table 1.1. As the scope of this study, most of the prototypes are designed, modeled, and tested for above 100 kHz applications. Finally, most of the models proposed in this thesis are generic. Therefore the core material, core size, and winding configurations are chosen randomly, e.g., Case 1: Ind. I1, I2, I3, I4, I5, I8, or

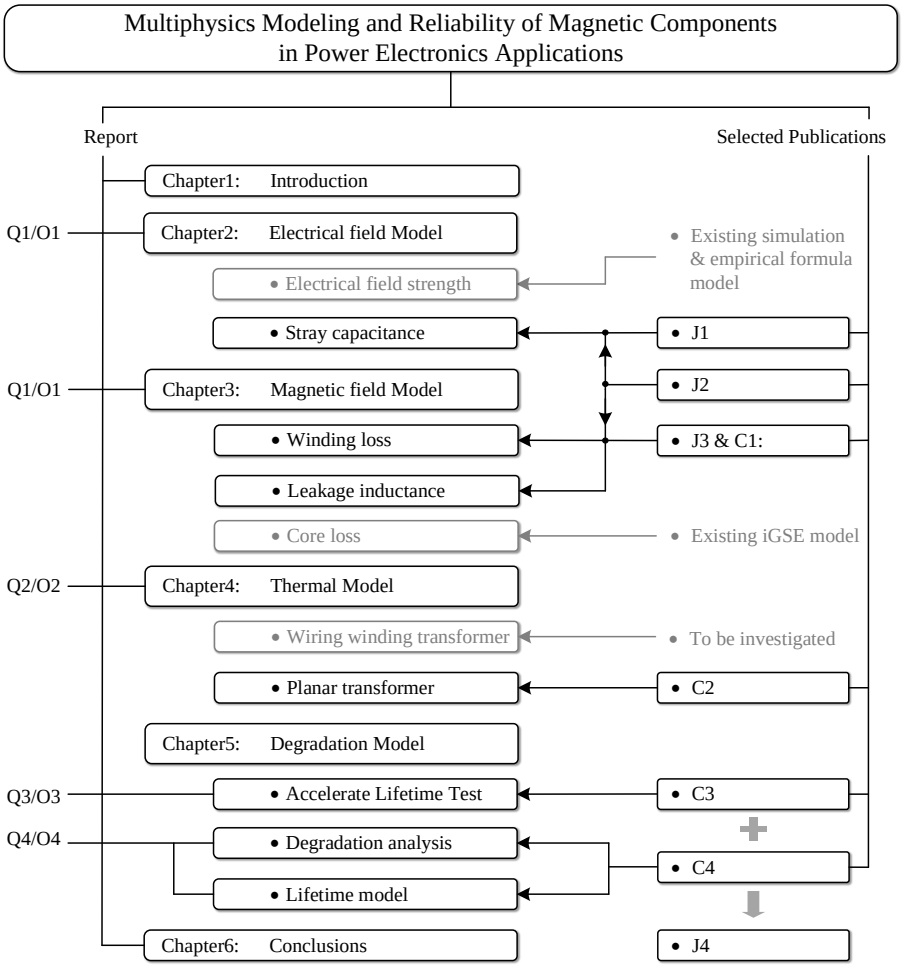

Fig. 1.4: Thesis structure and related publications. Study questions Q1 to Q4 and objectives O1 to O4 refer to Section 1.2. Publication titles J1 to J4 refer to Section 1.3.

according to a specific application scenario, e.g., Case 6: a planar transformer for a micro-inverter application in [6]. The lifetime model proposed in case 7 is for one kind of planar transformers in the testing. However, it is also of reference value to other kinds of planar magnetics and even wiring magnetics.

Table 1.1: Case study, proposed models, and relevant prototype numbers in this report

Case	Proposed models	Prototypes
1	Stray capacitance of inductors	Ind. I1, I2, I3, I4, I5, I8
2	Stray capacitance of Ow.	Ind. L2, L3, L4, L5, L8 & Ind. L2o, L3o, L4o, L5o, L8o
3	Ac resistance of partial layer winding	Tx. P1, P2, P3, P4
4	Ac resistance of Ow.	Tx. O1, O2, O3, O1o, O2o, O3o
5	Leakage inductance of Ow.	Tx. O1, O2, O3, O1o, O2o, O3o
6	Thermal network model of planar Tx.	Planar Tx. for a micro-inverter
7	Lifetime model of planar Tx.	Planar Tx. No. 1, 2,.., 24

Ind. : Inductor
Tx. : Transformer
Ow. : Orthocyclic winding

Chapter 2

Electric Field Modeling: Stray Capacitance of Inductors and Orthocyclic Windings

2.1 Background

This chapter studies the electrical field modeling of magnetic components. With the discussed urgent demands in the research field, the stray capacitance model of inductors and orthocyclic windings are investigated. An improved stray capacitance model is proposed for inductors considering the core/shield-related capacitance. The criteria in which scenarios the core/shield-related capacitance should be considered are also obtained. Moreover, compensating equations are used to modify the stray capacitance equation for compact orthocyclic windings. Finally, the difference between the compact normal and orthocyclic winding in terms of the stray capacitance is investigated to guide the winding design.

The stray capacitance of magnetics causes high-frequency oscillations, inrush charging current, and inductive impedance drop in the circuit. It might decrease efficiency, arise EMI problems, and affect the performance of the power electronic circuits if not modeled precisely and controlled appropriately [54].

Fig. 2.1(a) shows the equivalent circuit of an inductor. L is the inductance, C_{ind} is the stray capacitance, R_{p} and R_{w} are the equivalent resistance modeling the magnetic core and winding loss, respectively. Fig. 2.1(b) and (c) gives a brief illustration of the stray capacitance C_{ind}. It consists of the intra-winding capacitance C_{wwT} and the capacitance between the winding and core/shield C_{cwT}. Various models of C_{wwT} are summarized and compared in [63]. It is negligible when the distance between the core and winding is significant. However, if there is a low window space factor and the

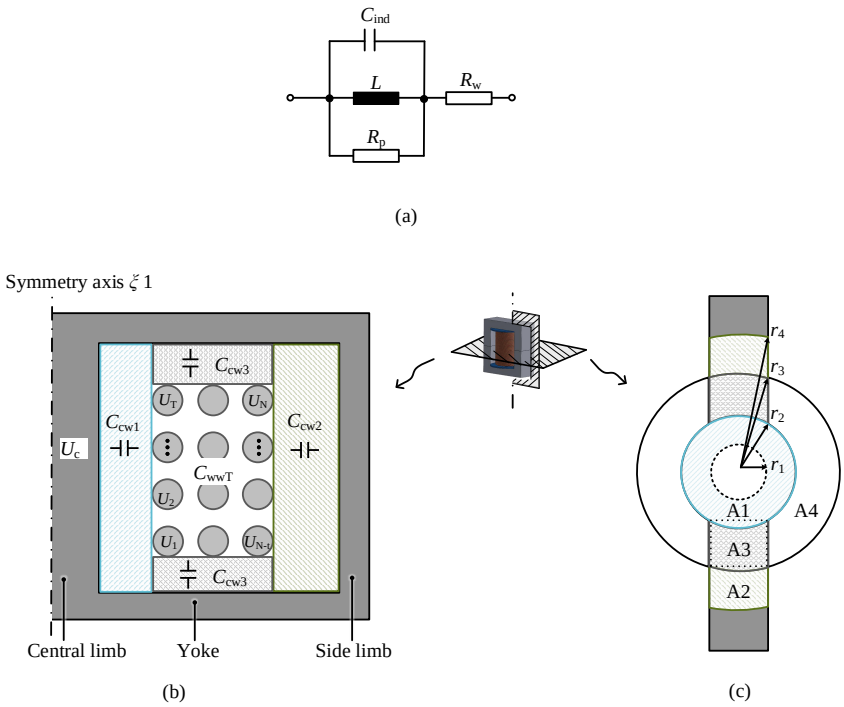

Fig. 2.1: An inductor and its stray capacitance. (a) is the equivalent circuit of an inductor. (b) and (c) are the cross-section and top view of an inductor with ETD core. C_{cw1} , C_{cw2}, C_{cw3}, and C_{wwT} are the central limb, side limb, yoke, and intra-winding capacitance, respectively, A1, A2, A3, and A4 are their electrical energy storage area, respectively. [J1], [78]

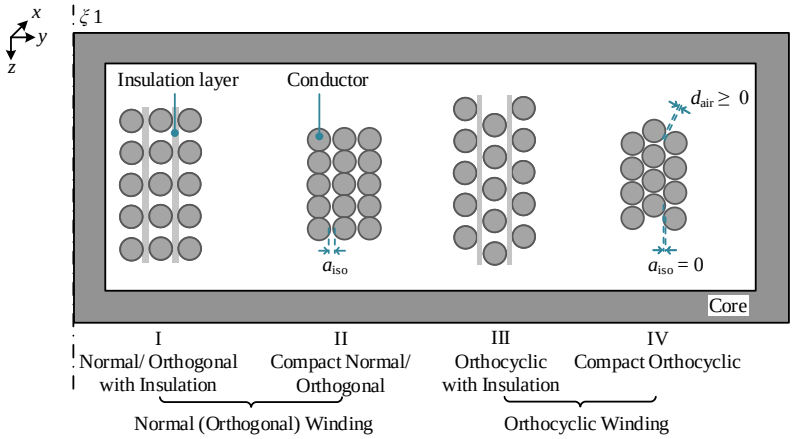

Fig. 2.2: Four types of typical winding types. d_{air} is the air gap width. a_{iso} is the insulation distance between two winding layers. [J2], [79]

outer limb/shield is close to the winding [80, 81], or the winding is directly winded on the core [64–66], or the facing area of the core/shield and winding increases especially in planar magnetics [82], C_{cwT} contributes to a significant proportion to the whole stray capacitance. Until now, a comprehensive research on the analytical model of C_{cwT} for inductors is missing. Therefore, an improved stray capacitance model is proposed in this study, which is also published in [J1], [78, 83].

Usually, the winding is designed and modeled as the normal orthogonal winding, which is illustrated in Fig. 2.2 as type I & II. However, for round wires, there is a curved edge from the cross-section of each turn. They are unstable when placing them on each other. Therefore, the designed type I & II winding becomes type III & IV in reality. Normally, the error or tolerance coefficients are used to explain the difference between them. However, for high-density applications with precise modeling requirements, those coefficients may not suitable anymore. A capacitance model considering the orthocyclic winding at the modeling stage is essential.

The study in [22] uses the parallel-plate and cylindrical models to calculate the orthocyclic winding with the modified concept of effective distance between layers. However, errors up to 60% are observed in [63]. In [64, 84], the stray capacitance model of the compact orthocyclic winding is obtained when the air gap $d_{\mathrm{air}} = 0$. However, in reality, $d_{\mathrm{air}} = 0$ is also difficult to achieve. There is irregular curvature in each turn, which leads to $d_{\mathrm{air}} > 0$. On the other hand, the stray capacitance value is susceptible to the air-gap distance, especially when the distance is small. Therefore, the model in [64, 84] normally overestimates the capacitance value, and a modification is necessary. A recent study in [85] uses a generic method to obtain the probabilistic distribution of the stray capacitance in different possible positions. In this project, the concept of the equivalent permittivity and wire diameter are proposed to calculate the compact orthocyclic windings, as they are reported in [J2], [79].

2.2 Analytical Modeling: Stray Capacitance of Inductors with Cores

- General Equations
  The stray capacitance of inductors with cores includes the intra-winding capacitance C_{ww}, central limb capacitance C_{cw1}, side limb capacitance C_{cw2}, and top and bottom yoke capacitance C_{cw3}. Multiplying them with the corresponding coefficients k_{ww}, k_{cw1}, k_{cw2}, and k_{cw3} obtains the total stray capacitance C_{ind}

$$\begin{aligned} C_{\mathrm{ind}} &= \underbrace{k_{\mathrm{ww}} \cdot C_{\mathrm{ww}}}_{C_{\mathrm{wwT}}} + \underbrace{k_{\mathrm{cw1}} \cdot C_{\mathrm{cw1}} + k_{\mathrm{cw2}} \cdot C_{\mathrm{cw2}} + k_{\mathrm{cw3}} \cdot C_{\mathrm{cw3}}}_{C_{\mathrm{cwT}}} \\ &= \sum k_x \cdot C_x \qquad\qquad x = \mathrm{ww}, \mathrm{cw1}, \mathrm{cw2} \text{ and } \mathrm{cw3} \end{aligned} \tag{2.1}$$

  where, C_x is named as inherent capacitance, k_x is the corresponding potential coefficient. $C_{\mathrm{cw}i}$ are applicable for both the core-to-winding and shield-to-winding capacitance. The derivation of each equation is given below, and they are also summarized in Fig. 2.3 together with the corresponding parameter definitions.

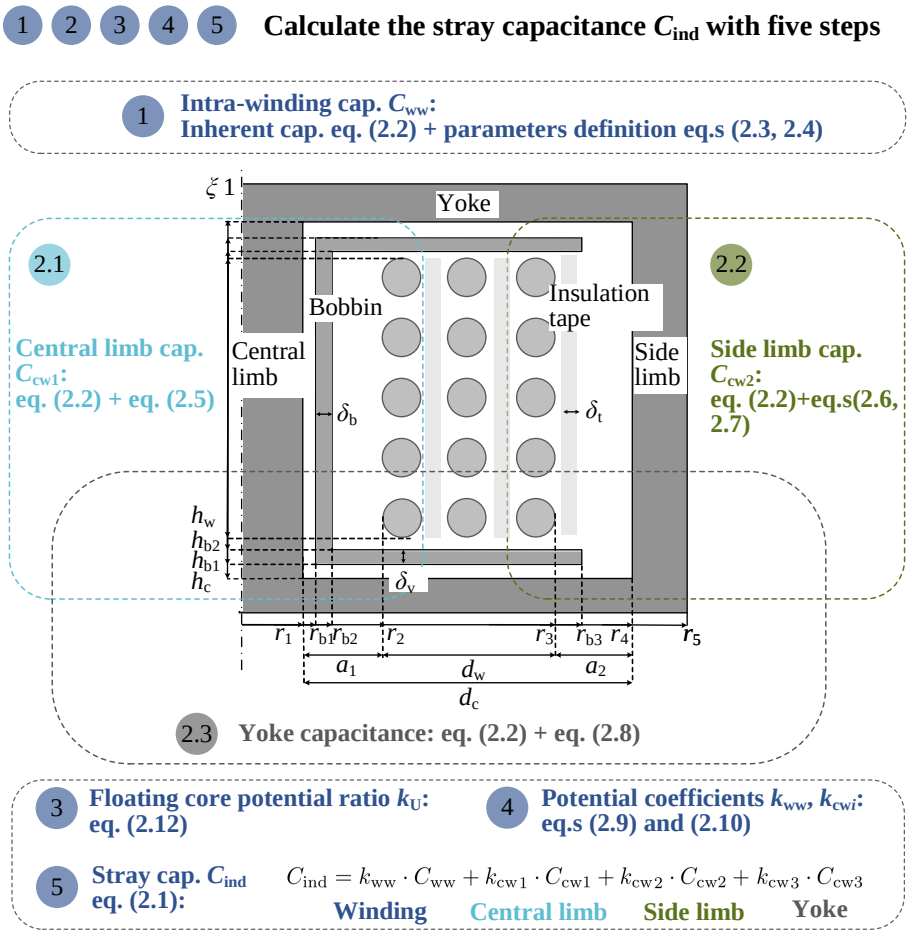

- t : the number of turns per layer
- r_1, r_2 : the window and winding inner radius
- r_3, r_4 : the winding and window outer radius
- l_{MLT} : the mean length per turn
- p : the number of layers
- d_e : the diameter of wire with insulation
- d_i : the diameter of wire without insulation
- ε_a : the permittivity of air
- ε_t, δ_t : the permittivity and thickness of the insulation tape
- ε_{wire}, δ_{wire} : the permittivity and thickness of wire coating
- ε_b : the permittivity of the bobbin
- h_c, h_w : the height of the window and winding
- δ_b , δ_v : the thickness of the bobbin in horizontal and vertical direction
- a_{iso}, h_{iso} : the distance between two bare wires in the window width and window height direction, respectively

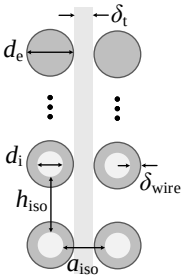

Fig. 2.3: Five steps to determine the stray capacitance C_{ind} of an inductor. [J1], [78]

- Inherent Capacitance

  The inherent capacitance is the capacitance between conductors without considering the potential applied. The parallel plate and coaxial cylindrical capacitance model are two well-known models [86]

$$C_x = \begin{cases} \alpha_x \cdot \varepsilon_0 \varepsilon_x \frac{A_x}{d_x} = \alpha_x \cdot \varepsilon_0 \varepsilon_x \frac{2\pi h_x r_x}{d_x} \\ \alpha_x \cdot \varepsilon_0 \varepsilon_x \frac{2\pi h_x}{\ln(1+\frac{d_x}{r_x})} \end{cases} \qquad x = \text{ww, cw1, cw2 and cw3} \tag{2.2}$$

  where α_{cw} is the weighting factor, A_x is the facing area, d_x is the effective distance between conductors, ε_x and ε_0 are the relative and vacuum permittivity, h_x is the height of plate/cylinder, and r_x is the width of plate or radius of cylinder, respectively. Applying parameters with different definitions obtains C_{ww}, C_{cw1}, C_{cw2}, and C_{cw3}, as introduced in the following.

  - Intra-winding Capacitance C_{ww}

    C_{ww} models the capacitance between layers, it uses (2.2) and the parameters are defined as [56, 63, 87]

$$\begin{aligned} &\alpha_{\text{ww}} = 1, \quad h_{\text{ww}} = t \cdot d_{\text{e}}, \quad d_{\text{ww}} = d_{\text{eff}}, \\ &r_{\text{ww}} = l_{\text{MLT}}/(2\pi), \quad \varepsilon_{\text{ww}} = \frac{\varepsilon_{\text{wire}} \varepsilon_{\text{t}} a_{\text{iso}}}{\varepsilon_{\text{wire}} \delta_{\text{t}} + 2\varepsilon_{\text{t}} \delta_{\text{wire}}} \end{aligned} \tag{2.3}$$

    where d_{eff} is the effective layer distance, for normal winding

$$d_{\text{eff}} = a_{\text{iso}} - 0.15 d_{\text{i}} + 0.26(h_{\text{iso}} + d_{\text{i}}) \tag{2.4}$$

  - Central Limb Capacitance C_{cw1}

    For MnZn ferrite with high permittivity above 10^4 [88, 89], it is equivalent to the perfect conductor with high conductivity in the electrostatic analysis [82]. The central limb capacitance C_{cw1} models the capacitance between the core central limb and the winding, including the bobbin in between. The parameters in (2.2) are defined by [64, 88]

$$\begin{aligned} &\alpha_{\text{cw1}} = 1, \quad h_{\text{cw1}} = h_c, \quad d_{\text{cw1}} = r_2 - r_1 + d_{\text{e}}/2, \\ &r_{\text{cw1}} = r_1 + d_{\text{cw1}}/2, \quad \varepsilon_{\text{cw1}} = \frac{\varepsilon_{\text{a}} \varepsilon_{\text{b}} d_{\text{cw1}}}{\varepsilon_{\text{a}} \delta_{\text{b}} + \varepsilon_{\text{b}} (r_2 - r_1 - \delta_{\text{b}})} \end{aligned} \tag{2.5}$$

    where ε_{cw1} is the equivalent permittivity of bobbin material and air in that area, d_{cw1} is the length from the core to the inner side of the winding, r_{cw1} is the length from the the middle point of the capacitance structure to the symmetrical axis, respectively.

  - Side Limb Capacitance C_{cw2}

    As the winding factor increases, the core side limb is close to the winding. C_{cw2} is to model their capacitance, and the parameters of (2.2) are

$$
\begin{aligned}
&h_{\mathrm{cw2}} = h_c, \quad d_{\mathrm{cw2}} = r_4 - r_3 + d_{\mathrm{e}}/2, \\
&r_{\mathrm{cw2}} = r_3 + d_{\mathrm{cw2}}/2, \quad \varepsilon_{\mathrm{cw2}} = \frac{\varepsilon_{\mathrm{a}}\varepsilon_{\mathrm{t}} d_{\mathrm{cw2}}}{\varepsilon_{\mathrm{a}}\delta_{\mathrm{t}} + \varepsilon_{\mathrm{t}}(d_{\mathrm{cw2}} - \delta_{\mathrm{t}})}
\end{aligned} \tag{2.6}
$$

where $\varepsilon_{\mathrm{cw2}}$ is the equivalent permittivity of tape material and air in that area, d_{cw2} is the length from core side limb to the outer side of the winding, r_{cw2} is the length from the middle point of the capacitance structure to the symmetrical axis, respectively. For ETD core, the side limb surrounds only a portion of the winding, as is shown in Fig. 2.1(c). The weighting factor α_{cw2} is used to model this proportion

$$
\alpha_{\mathrm{cw2}} \approx 4r_1/(2\pi r_3) \approx 4r_1/(\pi r_1 + \pi r_4) \tag{2.7}
$$

The concept of α_{cw2} is similar to the proportion in the ERXP model in [90], and it changes with core structures.

– Yoke Capacitance C_{cw3}

When the winding height increases, the capacitance between core top/bottom yoke and the winding C_{cw3} increases. Eq. (2.2) is defined by

$$
\begin{aligned}
&\alpha_{\mathrm{cw3}} = 1, \quad A_{\mathrm{cw3}} \approx 4r_1(r_3 - r_2), \\
&d_{\mathrm{cw3}} = (h_{\mathrm{c}} - h_{\mathrm{w}})/2 + d_{\mathrm{e}}/2, \quad \varepsilon_{\mathrm{cw3}} = \frac{\varepsilon_{\mathrm{a}}\varepsilon_{\mathrm{b}} d_{\mathrm{cw3}}}{\varepsilon_{\mathrm{a}}\delta_{\mathrm{v}} + \varepsilon_{\mathrm{b}}(\frac{h_{\mathrm{c}}}{2} - \frac{h_{\mathrm{w}}}{2} - \delta_{\mathrm{v}})}
\end{aligned} \tag{2.8}
$$

where $\varepsilon_{\mathrm{cw3}}$ is the equivalent permittivity of bobbin material and air in that area, d_{cw3} is the length from the core yoke to the winding, A_{cw3} is defined in Fig. 2.1(c) and it is twice of the area of A3. A3 approximately equals to the area of the dot frame rectangle, which is $2r_1 \times (r_3 - r_2)$.

- Potential Coefficients

The inherent capacitance model (2.2) assumes that the voltage potential is the same in each electrode, i.e., the winding and core. However, it is not the case in the inductor, as shown in Fig. 2.4. To consider the potential difference, the potential coefficients k_x are needed to modify the inherent capacitance and finally get the stray capacitance C_{ind} seen from winding terminals.

– Intra-winding Coefficient k_{ww}

k_{ww} for modifying C_{ww} of the winding is [56, 91]

$$
k_{\mathrm{ww}} = \beta(p-1)(\frac{2}{p})^2 \tag{2.9}
$$

where, β is wiring coefficient of the winding, which is $1/4$ for flyback windings and $1/3$ for regular windings, respectively.

– Core-related Coefficient $k_{\mathrm{cw}i}$

$k_{\mathrm{cw}i}$ for modifying $C_{\mathrm{cw}i}$ of the winding and core is

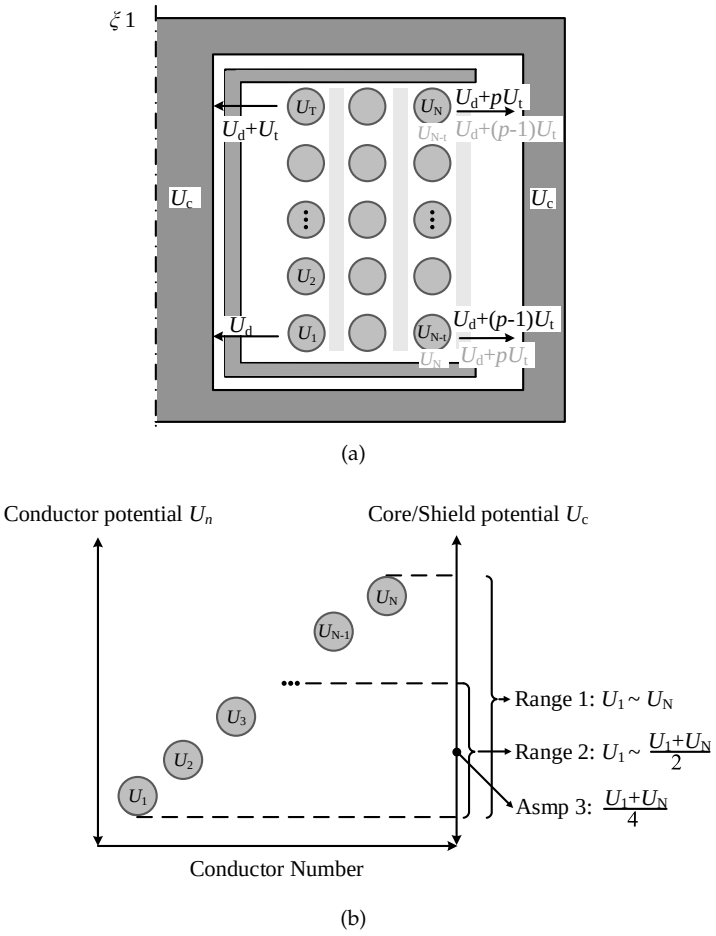

Fig. 2.4: The potential of the winding and the core/shield. (a) Cross-section of the inductor. The potential of the winding is illustrated from U_1 to U_N for each turn, and the potential of the core is illustrated as U_c. The arrow indicates the voltage between the core and winding. (b) Potential comparison of each turn and the core. Normally the potential of the core U_c locates between the U_1 and U_N, as Range 1. Usually, the core is with smaller distance to core central limb than to core side limb, and U_c is more close to U_1, as Range 2. A simple assumption of U_c is with Assumption 3 (Asmp 3). [J1], [78]

$$
\begin{aligned}
k_{cw1} &= \frac{3k_U^2 + 3k_U + 1}{3p^2}, \\
k_{cw2} &= \frac{3k_U^2 + (6p-3)k_U + (3p^2 - 3p + 1)}{3p^2}, \\
k_{cw3} &= \frac{6k_U^2 + 6pk_U + (2p^2 - p + 2)}{3p^2} \quad \text{or} \quad \frac{6k_U^2 + 6pk_U + (2p^2 - p + 1)}{3p^2}
\end{aligned}
\tag{2.10}
$$

Table 2.1: Prototypes I1 to I8 used for Case Study 1

	Value	Units
Core size	ETD 59/31/22	
Core material	N97 (MnZn ferrite)	
Bobbin size	B66398	
Layers p	1, 2, 3, 4, 5, 8	
Turns per layer t	34	
Round wire Dia. d_i	1	mm

where $k_\mathrm{U} = U_\mathrm{d}/U_\mathrm{t}$, $U_\mathrm{d} = U_1 - U_\mathrm{C}$ as shown in Fig. 2.4(a). $k_{\mathrm{cw}3}$ are with two values for the winding terminals in different directions. Their voltage potentials are in black and gray letters in Fig. 2.4(a), respectively. The first one is used due to their negligible difference. Appendix A.1 gives the derivation process of (2.10).

- Floating Core/Shield Potential U_C

  The core-related coefficients need the input of k_U, which is the relation between the potential of the core and winding. Therefore, U_C should be obtained. The range and assumption of U_C are in Fig. 2.4(b) and explained in its caption.

  To accurately get U_C requires the circuit model in Fig. 2.5(a). Using Kirchhoff's Current Law, U_C is obtained with the expression of the voltage of the winding, as more derived in Appendix A.2

$$U_\mathrm{c} = U_1 + \frac{C_{\mathrm{cw}1} + (2p-1)C_{\mathrm{cw}2} + 2pC_{\mathrm{cw}3}}{2C_{\mathrm{cw}1} + 2C_{\mathrm{cw}2} + 4C_{\mathrm{cw}3}} U_\mathrm{t} \tag{2.11}$$

$$k_\mathrm{U} = -\frac{C_{\mathrm{cw}1} + (2p-1)C_{\mathrm{cw}2} + 2pC_{\mathrm{cw}3}}{2C_{\mathrm{cw}1} + 2C_{\mathrm{cw}2} + 4C_{\mathrm{cw}3}} \tag{2.12}$$

  These equations are derived when the core is assembled without air gap, so the core is with the uniform potential. For a core with air gaps in between, they are required to be derived again following a similar process.

  Inductor prototypes named I1, I2, I3, I4, I5, and I8 are built to verify the analytical formula of U_c, as shown in Table 2.1. They are designed with the same core and winding configuration, while with different layers p. Comparison is made with finite element method (FEM) simulation results, as shown in Fig. 2.5(b). The simulation is using the axisymmetric dimension, electrostatics field, and in the software FEMM [92]. The cross-section in Fig. 2.3 is used for simulation. Some simulation results are also given in Fig. 2.6 in next section. In Fig. 2.5(b), the analytical calculations are close to simulation results. As p increases, U_c starts from the middle voltage of the winding 0.5V and decreases to approximately 0.25V, which also verifies the Assumption 3 in Fig. 2.4(b).

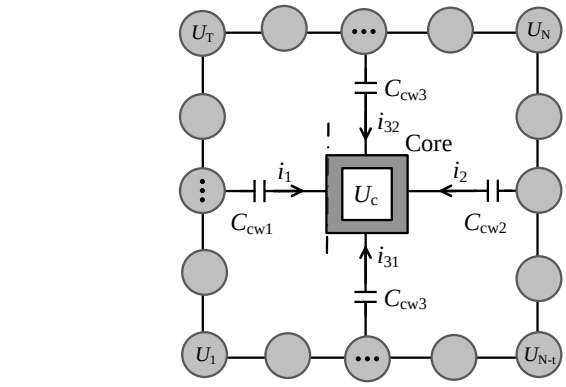

(a)

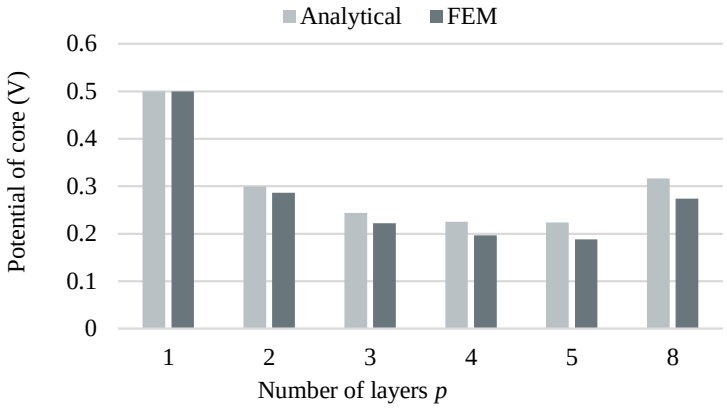

(b)

Fig. 2.5: Circuit and verification of the potential of core/shield U_c. (a) The equivalent circuit. It transfers the electric field problem to the electric circuit problem, and then solve U_c by Kirchhoff's Current Law (KCL). (b) The simulation verification of the analytical model from I1 to I8 (c.f. Table 2.1). In the simulation, U_1= 0V, U_N= 1V, the voltage of the turns in between increases linearly. [J1], [78]

2.3 Case Study 1: Inductors with Cores

The six inductors simulated in the last section are built, simulated, and tested in this case study, and some of them are shown in Fig. 2.6. Their results are compared in Fig. 2.7.

In the simulation, the stray capacitance C_{ind} is calculated with the energy method

$$C_{ind} = 2W_{sim}/(U_N - U_1)^2 \tag{2.13}$$

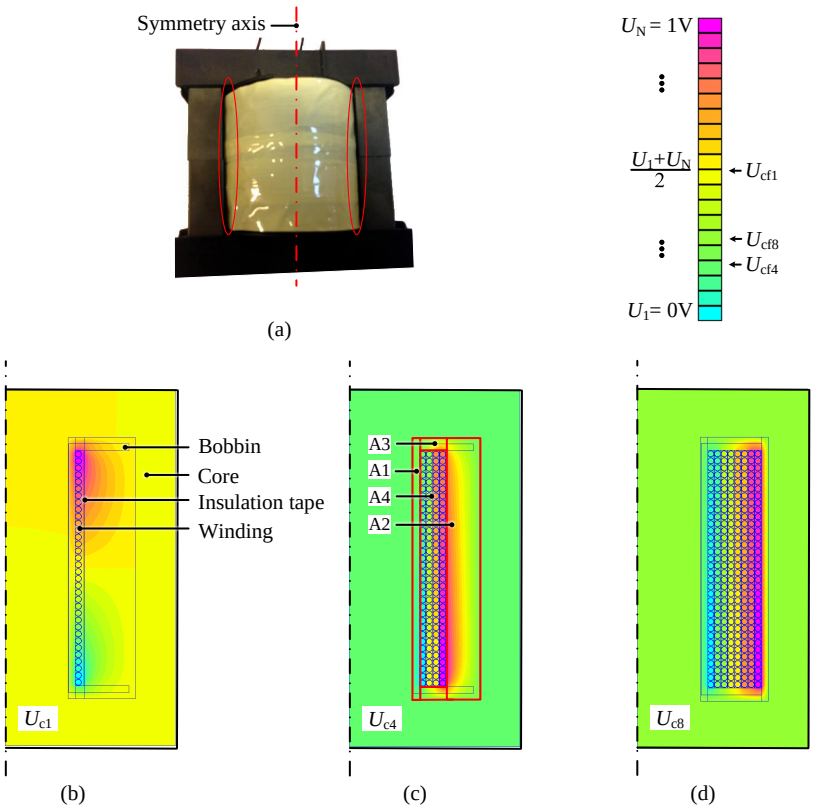

Fig. 2.6: The built prototype I8 (a) and the simulation results of I1 (b), I4 (c) and I8 (d). The potential of the core, $U_{c1} \approx 0.5\ V$, $U_{c4} \approx 0.2\ V$, and $U_{c8} \approx 0.3\ V$, are indicated by the color in each simulation case. They agree well with the analytical calculation in Fig. 2.5(b). A1, A2, A3, and A4 are the relevant area for C_{cwi} in Fig. 2.1(c). [J1], [78]

where W_{sim} is the stored energy of the inductor, voltages from U_1 to U_N are applied to each turn of the winding.

Moreover, similar to (2.7), the core also surrounds the winding the full circle in the simulation, which is different from reality. A coefficient is used to compensate for this effect by modifying the permittivity in this area, referring to the method in [93]. In region A2 the coefficient is

$$k_{sim2} = 4r_1/(2\pi r_3) \tag{2.14}$$

In region A3 it is

$$k_{sim3} = 4r_1/(\pi r_2 + \pi r_3) \tag{2.15}$$

For the experiment, Keysight impedance analyzer E4990A is used for the measurement. The frequency at zero phase angle is obtained, and the stray capacitance is calculated with the resonant method [88, 94]. The whole stray capacitance C_{ind}

is measured by the inductor with the core, and the intra-winding capacitance C_{wwT} is measured after disassembling the core. Subtracting them obtains the core-related capacitance C_{cwT}.

From the comparison in Fig. 2.7, the results of the analytical, FEM, and experiments fit well. The errors between them come from three perspectives, i.e., the frequency-dependent character of the core, which should be modeled by a combination of inductance, capacitance, and resistance [82, 95]; the mismatch between the designed normal winding and built orthocyclic winding in reality; and the errors in the dimension measurement. One special case is I2 with $p = 2$, where C_{wwT} without core is larger than C_{ind} with the core, so the measured value is set as zero. This is due to the nonlinearity of the core material, which is pointed out as the first error source. Nevertheless, this effect is limited and only exists in one prototype in this case study. A more detailed error analysis refers to the discussions in [J1], [78].

The percentage of $C_{\mathrm{cw}i}$ varies in each cases. C_{cw1} is the largest when $p = 1$. C_{cw2} increases with p due to the decrease of the distance between the winding and side limb. It dominates C_{cwT} for large-winding-factor scenarios. C_{cw3} increases stably and also becomes significant when p increases. Therefore for large-winding-factor inductors, only considering the central-limb capacitance C_{cw1} underestimates the total core-related capacitance significantly.

The percentage of C_{cwT} in the whole stray capacitance C_{ind} is significant when $p = 1$, then it drops to become negligible when $p = 2$, after that it increases with p. So C_{cwT} is essential for two extreme scenarios: the inductor with one layer and with all layers. To determine whether C_{cwT} should be considered, quantitative criteria should be used, and they are given in the next section.

Finally, only inductors with the floating core are discussed in this report. In fact, the proposed equation is also capable of handling the inductor with a grounded core or grounded shield. In that case, the potential of the core U_{c} is set to the grounding voltage, and the k_{U} in (2.10) and the all $k_{\mathrm{cw}i}$ is re-calculated accordingly. The verification of this situation is introduced in [J1], [78].

2.4 Criteria to Consider Core/Shield-related Capacitance

The core/shield-related capacitance ratio $C_{\mathrm{cw}}/C_{\mathrm{ind}}$ of inductors with core ETD 59/31/22 and P30/19 is shown in Fig. 2.8. Fig. 2.8(b) is the inductor with a flux band. The flux band is a shield, which is conductive and surrounds the magnetics to suppress the interaction from the magnetics to other electrical devices. It also contributes to the core/shield-related capacitance. In all three cases, windings are assumed to occupy the window height fully. The x-axis of each figure is the ratio of the width of the winding to the core. This ratio is also proportional to the winding factor and the layers p.

In three cases in Fig. 2.8, $C_{\mathrm{cw}}/C_{\mathrm{ind}}$ is significant when $p = 1$, then it drops close to zero, and then increases to between 20% and 100% at last. This changing trend is also applicable to other cores. For the pot core inductor, its side limb surrounds the winding and is with higher core-related capacitance ratio than ETD cores. Also, the

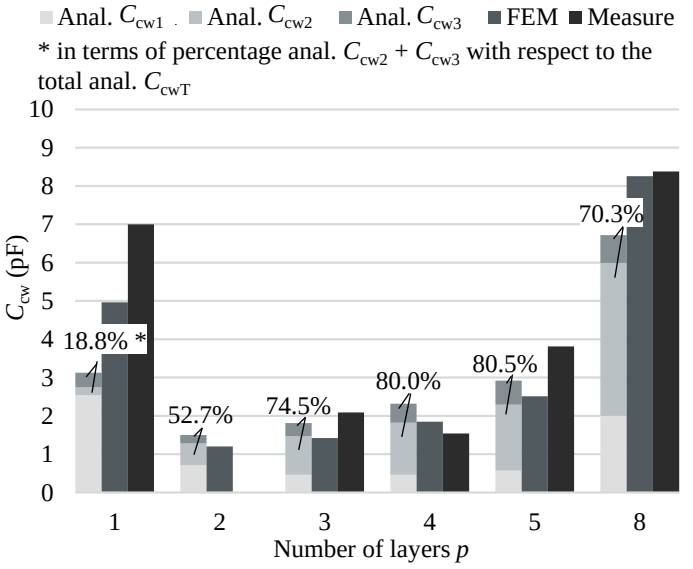

(a)

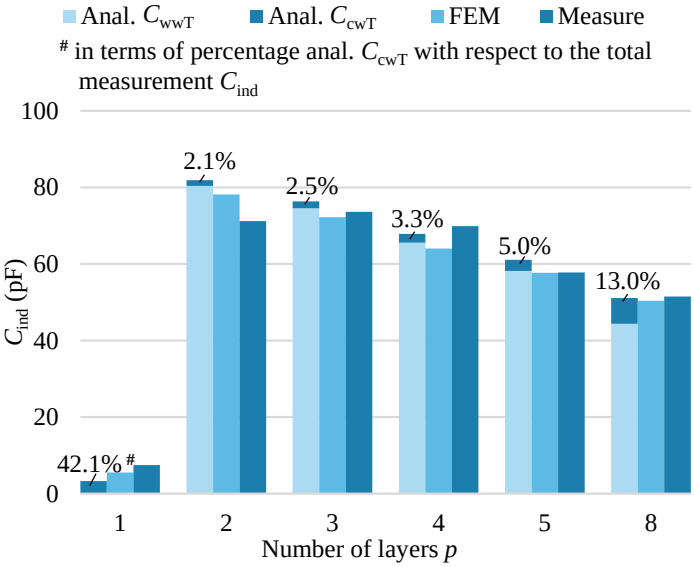

(b)

Fig. 2.7: Comparison of the stray capacitance of inductors I1 to I8 with floating core (c.f. Table 2.1). The analytical, FEM, and experimental results are indicated by Anal., FEM, and Measure, respectively. (a) Core-related capacitance. (b) Total capacitance. [J1], [78]

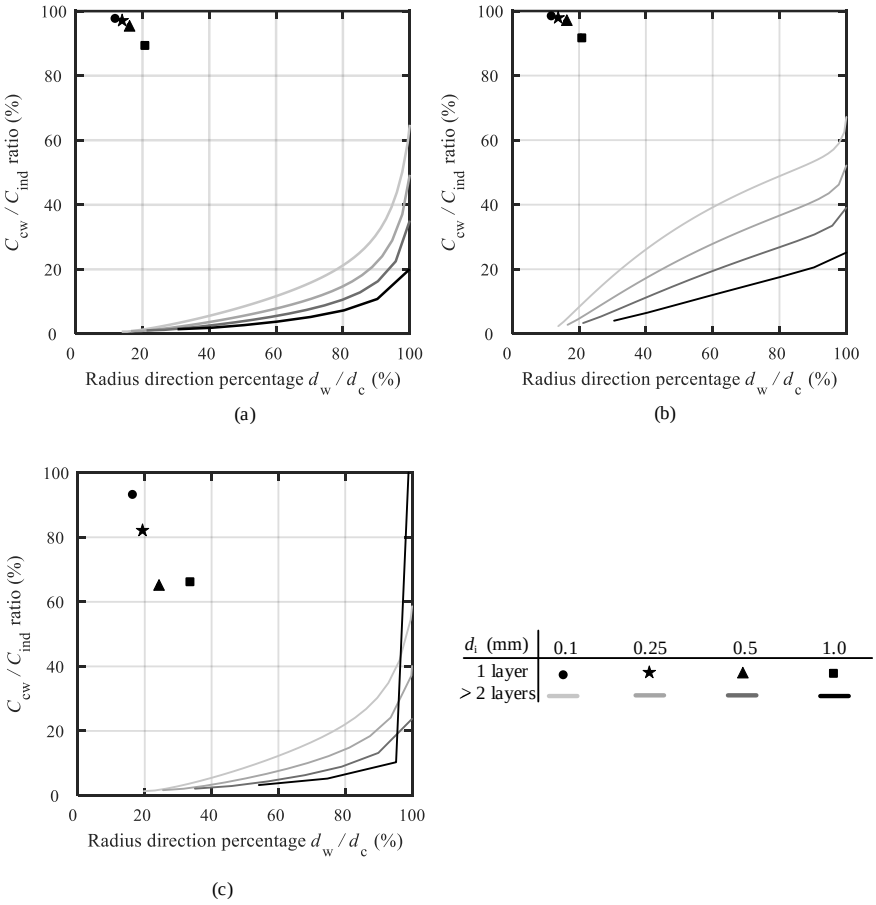

Fig. 2.8: The core/shield-related capacitance ratio C_{cw}/C_{ind}. The x-axis of each figure is the ratio of the width of the winding to the core. (a) is with ETD59/31/22 core, (b) is with the same core as (a) plus a flux band, (c) is with the pot-type core P30/19. Different wire diameters d_i from 0.1 mm to 1.0 mm are listed in each case. There is a significant step increase of the winding capacitance from one turn to multi-turns. Therefore the core/shield-related capacitance ratio decreases dramatically without a smooth transition. So the one turn scenarios are listed separately. [J1], [78]

thinner wire leads to a higher core/shield-related capacitance ratio.

In general, the criteria to determine C_{cw} is set as $C_{cw}/C_{ind} \geq 10\%$. As a rule of thumb, the circumstances are inductors:

1. With only one layer winding;
2. With a flux band or shield;
3. With E and P type cores, and with a winding width percentage d_w/d_c larger than 50%.

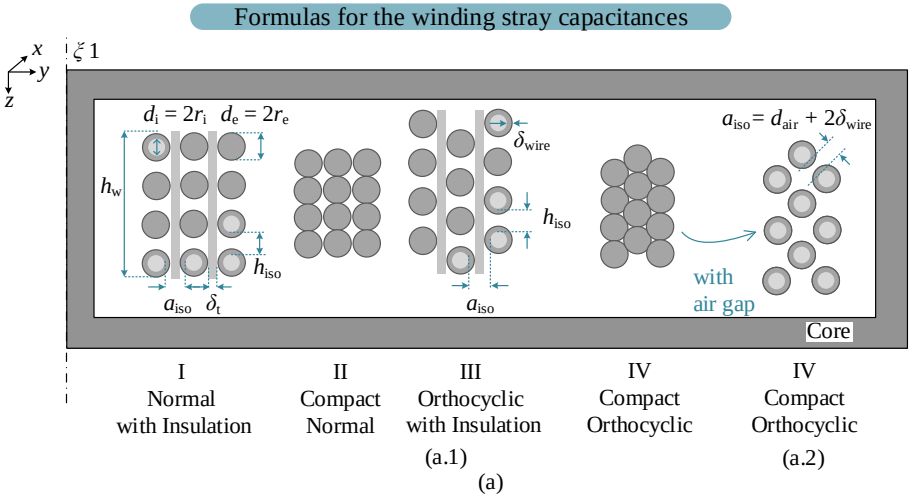

1 Layer capacitance C_l

- $C_{ww,n}$ for winding type I, II, and III, eq. (2.2, 2.3, 2.4):

$$C_{ww,n} = \varepsilon_0 \varepsilon_{wire} \frac{2\pi h_w (l_{MLT}/(2\pi))}{d_{ww}} \qquad d_{ww} = a_{iso} - 0.15 d_i + 0.26(h_{iso} + d_i)$$

- $C_{ww,d}$ for winding type IV, eq. (2.16):

$$C_{ww,o} = t\varepsilon_0 \frac{4\varepsilon_{wire} \arctan\left[\frac{(\sqrt{3}-1)(2\varepsilon_{wire}+k_{ln})}{(\sqrt{3}+1)\sqrt{k_{ln}(2\varepsilon_{wire}+k_{ln})}}\right]}{\sqrt{2\varepsilon_{wire} k_{ln} + k_{ln}^2}} \qquad k_{ln} = \ln k_{rad} \qquad k_{rad} = d_e/d_i$$

ε_{wire} , d_e is substituted by $\varepsilon_{wire,eq}$, $d_{e,eq}$, eq. (2.17, 2.18):

$$\varepsilon_{wire,eq} = \frac{\varepsilon_{wire}\varepsilon_0 (d_{air} + 2\delta_{wire})}{\varepsilon_{wire} d_{air} + 2\varepsilon_0 \delta_{wire}} \qquad d_{e,eq} = d_i + a_{iso}$$

2 Winding capacitance C_w, eq. (2.1, 2.9):

$$C_w = \beta \cdot C_{ww} (p-1) \left(\frac{2}{p}\right)^2$$

- h_w : the height of the winding
- r_e : the wire radius with coating
- d_e : the wire diameter with coating
- r_i : the wire radius without coating
- d_i : the wire diameter without coating
- d_{air} : the air gap length
- p : the number of layers
- t : the number of turns per layer
- a_{iso} : the inter-layer insulation distance
- ε_0 , ε_{wire} : the vacuum and relative permittivity of wire insulation
- l_{MLT} : the mean length per turn
- d_{ww} : the effective distance between layers
- h_{iso} : the inter-turn insulation distance in height direction
- k_{rad} : the radius ratio
- β : the winding wiring coefficient, equals to 1/3 for normal winding and 1/4 for flyback winding

(b)

Fig. 2.9: Normal and orthocyclic winding capacitance formulas. (a.1) Four types of winding configurations and the dimension definition. (a.2) Proposed definition of the inter-layer insulation distance a_{iso} for the winding IV. (b) Capacitance formula. [J2], [79]

2.5 Analytical Modeling: Stray Capacitance of Orthocyclic Windings

The above discussion assumes the wire of the winding is distributed orderly, as the normal winding type I and II in Fig. 2.9. However, due to the round edge of the wire, the normal winding configuration is in an unstable position, and the wires displace as orthocyclic winding III and IV in reality.

To calculate the stray capacitance of the compact orthocyclic windings, The electric field of the compact orthocyclic winding is modeled in [64, 87] and the obtained winding capacitance is

$$C_{\mathrm{ww,o}} = t\varepsilon_0 \frac{4\varepsilon_{\mathrm{wire}} \arctan\left[\frac{(\sqrt{3}-1)(2\varepsilon_{\mathrm{wire}}+k_{\mathrm{ln}})}{(\sqrt{3}+1)\sqrt{k_{\mathrm{ln}}(2\varepsilon_{\mathrm{wire}}+k_{\mathrm{ln}})}}\right]}{\sqrt{2\varepsilon_{\mathrm{wire}}k_{\mathrm{ln}}+k_{\mathrm{ln}}^2}} \tag{2.16}$$

where $k_{\mathrm{ln}} = \ln k_{\mathrm{rad}}$, $k_{\mathrm{rad}} = d_{\mathrm{e}}/d_{\mathrm{i}}$ is the radius ratio. (2.16) does not consider the air gap distance d_{air} between layers. It overestimates the stray capacitance in reality because wiring the compact orthocyclic winding is difficult due to the hardness of the copper wire. Between turns in the neighborhood layers, there are air gap d_{air}, the insulation of two wires. To compensate the air gap d_{air}, the modifications of permittivity of insulation $\varepsilon_{\mathrm{wire}}$ and diameter of coating wire d_{e} to the equivalent permittivity $\varepsilon_{\mathrm{wire,eq}}$ and equivalent diameter $d_{\mathrm{e,eq}}$ are necessary

$$\varepsilon_{\mathrm{wire,eq}} = \frac{\varepsilon_{\mathrm{wire}}\varepsilon_0(d_{\mathrm{air}}+2\delta_{\mathrm{wire}})}{\varepsilon_{\mathrm{wire}}d_{\mathrm{air}}+2\varepsilon_0\delta_{\mathrm{wire}}} \tag{2.17}$$

$$d_{\mathrm{e,eq}} = d_{\mathrm{i}} + a_{\mathrm{iso}} \tag{2.18}$$

In general, the formulas for stray capacitance of winding type I, II, III, and IV are summarized in Fig. 2.9.

2.6 Case Study 2: Inductors with Normal and Orthocyclic Windings

To verify the proposed model with the modified permittivity and wire diameter, a series of inductors with compact normal winding type, i.e., L2, L3, L4, L5, and L8, and with compact orthocyclic winding, i.e., L2o, L3o, L4o, L5o, and L8o, are designed. Their winding configurations are in Table 2.2. Their photo and simulations of L8/L8o are shown in Fig. 2.10. Their finite element method simulation (FEM), analytical calculation (Anal.), and measurement (Meas.) results are compared in Fig. 2.11.

From the comparison, the analytical results of (2.16) without air-gap compensation are with the most significant error, which indicates that the air-gap is nonnegligible. The Anal. Norm. is the parallel-plate model (2.2), (2.3) and (2.4). It is for the compact normal winding and is with negligible error compared with the simulation results

Table 2.2: Inductors with normal and orthocyclic windings for Case Study 2 [J2], [79]

Parameters	Normal L2, L3, L4, L5, L8	Orthocyclic L2o, L3o, L4o, L5o, L8o	Units
Core size	ETD 59/31/22		
Layers p	2, 3, 4, 5, 8		
Turns per layer t	34		
Round wire Dia. d_{i}	1		mm
Wire Iso. δ_{wire}	0.05		mm
Inter-layer a_{iso}	0.13		mm

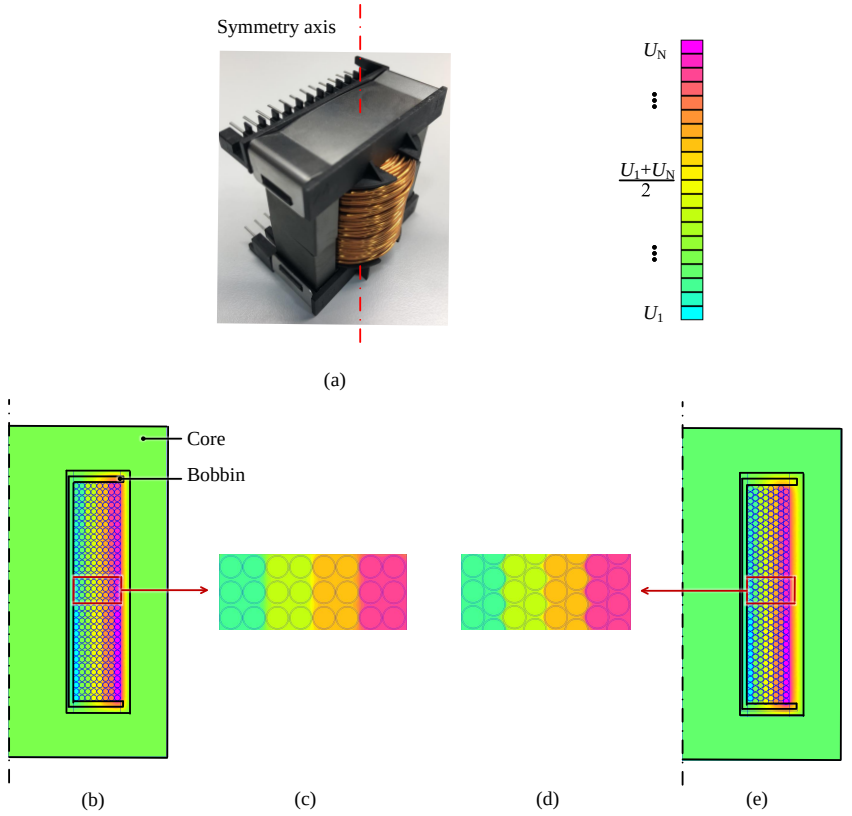

Fig. 2.10: Photo of L8o and electrical field simulation results of L8/L8o (c.f. Table 2.2). (a) is the photo of L8o. (b, e) are the simulation of L8 and L8o, and (c, d) are their winding zoom-in results, respectively. The color in the simulation results indicates their voltage distribution in the electric static simulation. [J2], [79]

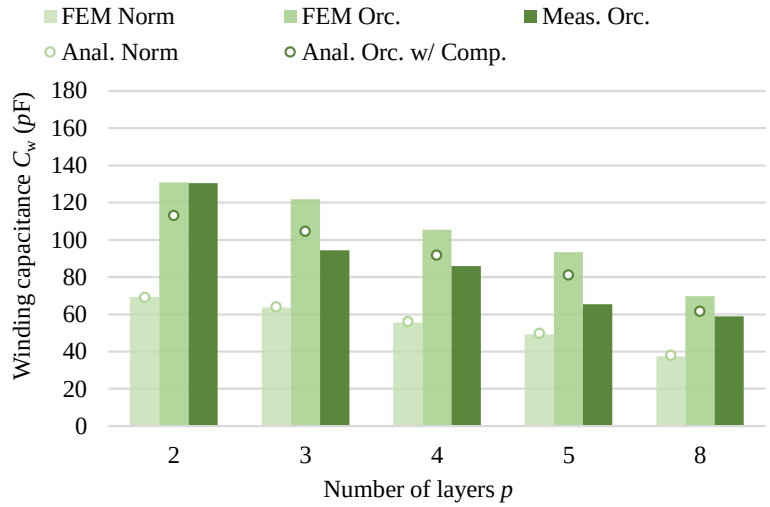

(a)

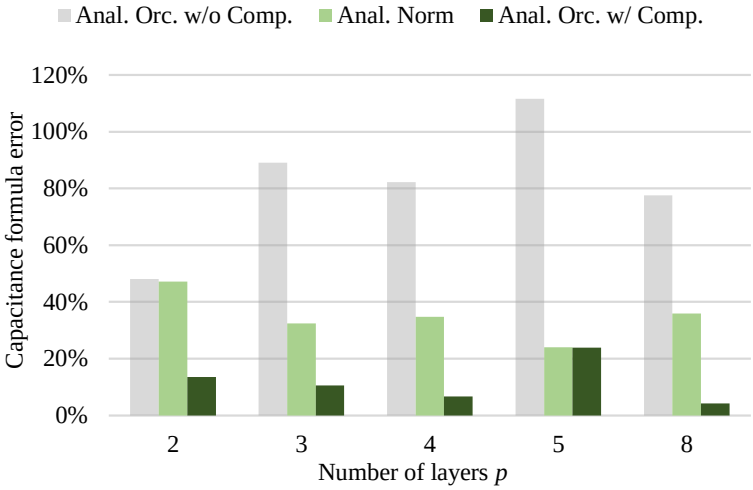

(b)

Fig. 2.11: Winding capacitance of inductors with normal (Norm.) and orthocyclic (Orc.) windings (c.f. Table 2.2). The analytical, finite element method simulation, and measurement results are marked as Anal., FEM, and Meas., respectively. Anal. Orc. w/ and w/o Comp. are the results of (2.16) with and without compensation equations (2.17) and (2.18), respectively. (a) The stray capacitance of inductors with 2, 3, 4, 5, and 8 layers of normal winding (L2 to L8) and compact orthocyclic winding (L2o to L8o). Only inductors with orthocyclic winding are built and measured because the normal winding is difficult to build in reality. (b) An error comparison with the measurement results of L2o to L8o. [J2], [79]

(FEM Norm). However, when compared with the compact orthocyclic winding measurement results, the Anal. Norm. is with a significant error, even the parameters of both winding configurations are the same. The maximum error is up to 47.1%. Finally, with the proposed modified equations (2.16), (2.17), and (2.18), the calculated results are with the lowest errors in three models, and the maximum error in the five inductors is 23.9%.

In reality, an ideal winding type IV is also challenging to be built. Due to the round curve of the wire, the wire is located between the position of winding type II and IV. So the measured capacitance is also located between the simulation results of those two types of windings. However, the real winding position is more close to the winding type IV than type II, as indicated by the measurement results.

2.7 Orthocyclic Capacitance Ratio

To generically compare the impact of changing from the compact normal winding type II to the compact orthocyclic winding type IV, the orthocyclic capacitance ratio k_c is defined

$$k_c = \frac{C_{ww,o}}{C_{ww,n}} \cdot 100\% \tag{2.19}$$

When changing ε_{wire} from 1 to 5 and changing k_{rad} from 1.05 to 2, the corresponding k_c is illustrated in Fig. 2.12. Several generic conclusions are obtained

- Usually the winding is designed as the normal winding and built more close to the orthocyclic winding configuration;
- For the same winding dimension, same insulation, and no air gap, the stray capacitance of the compact orthocyclic winding is different from the compact normal winding, and it results in a maximum of 118% increase or 20% decrease in the different scenarios;
- Their difference in the winding capacitance decreases with the number of layers p;
- One method to decrease the difference is to design the wires in the *safe area* in Fig. 2.12 with larger permittivity and thicker wire coating;
- Another method to decrease their difference is to add insulation tape between layers.

2.8 Conclusions

This chapter studies the electric field modeling, and proposes an improved stray capacitance model for inductors and a modified capacitance model for orthocyclic windings. The effect of the core central limb, side limb, and yoke are all considered in the capacitance model for inductors. The model is applicable for both the floating and grounded core/shield scenarios. The proposed model is verified in the case study by

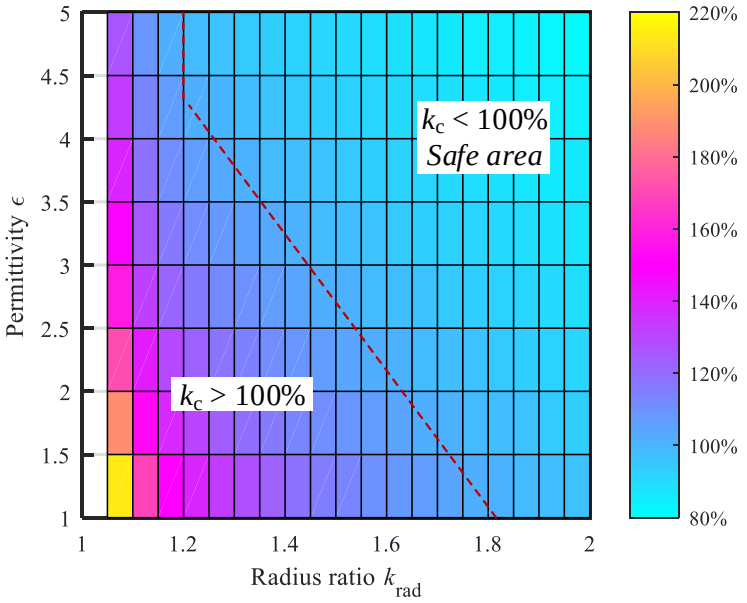

Fig. 2.12: The orthocyclic capacitance ratio k_c changes with the permittivity of insulation coating ε_{wire} and radius ratio k_{rad}. The air gap length $d_{air} = 0$. The *safe area* is distinguished by the red dashed line. It is $k_c \leq 100\%$ area, and means that the winding capacitance does not increase when changes form the compact normal winding type II to the compact orthocyclic winding type IV. [J2], [79]

six inductors with FEM simulation and experimental results. The criteria to consider the core/shield-related capacitance is presented with a maximum 10% core/shield-related capacitance ratio. Moreover, a capacitance model for the orthocyclic winding is also studied considering the air-gap effect with compensating equations. Compared with the compact normal winding, the capacitance of the compact orthocyclic winding can increase up to 118% or decrease up to 20% dependents on the radius ratio and permittivity.

In general, this chapter is with four major contributions:

- Propose an improved stray capacitance model for inductors;
- Give the criteria to consider the core/shield-related capacitance;
- Propose compensating equations for the stray capacitance of compact orthocyclic windings;
- Give a generic comparison of the compact normal and compact orthocyclic winding in terms of the stray capacitance, which should be considered during the design of inductors and transformers.

Chapter 3

Magnetic Field Modeling: Winding Loss and Leakage Inductance

3.1 Background

This chapter studies the magnetic field modeling of magnetic components. Dowell's equation is firstly reviewed [77]. Then the power loss of the partial layer winding and the orthocyclic windings are investigated. Finally, a leakage inductance model for the orthocyclic winding is also studied.

The high-frequency winding power loss is induced by skin and proximity effects. Dowell proposed a closed-form equation in the Cartesian coordinate system, and it is widely used for the ac resistance calculation and optimization [98–100]. The winding loss in the cylindrical coordinate system is derived in [101, 102]. These methods are compared in [103]. There are also analytical models for Litz wire [104–106]. With the advances in computational resources, recent research uses the magnetic field simulation to acquire more accurate results than the analytical calculations. Further, using those simulation results to fit the corresponding coefficients, the computational-aid and semi-empirical models are proposed [107–111]. They achieve good accuracy without too much computational burden .

Power electronics go higher and higher frequency and density with limited design margin. Special windings, e.g., the partial layer winding and orthocyclic winding, should be modeled precisely for the model-based design. They are shown in Fig. 3.1. The conventional Dowell's equation and leakage inductance formula are not applicable anymore.

The partial layer winding is a concept that is distinguished from the full layer winding. A full layer wraps the wires to occupy all of the core window height, with the number of turns per layer t. When it comes to the last layer, a partial layer appears if the remaining turns $t_0 < t$. Normally the partial layer is applied in the design to

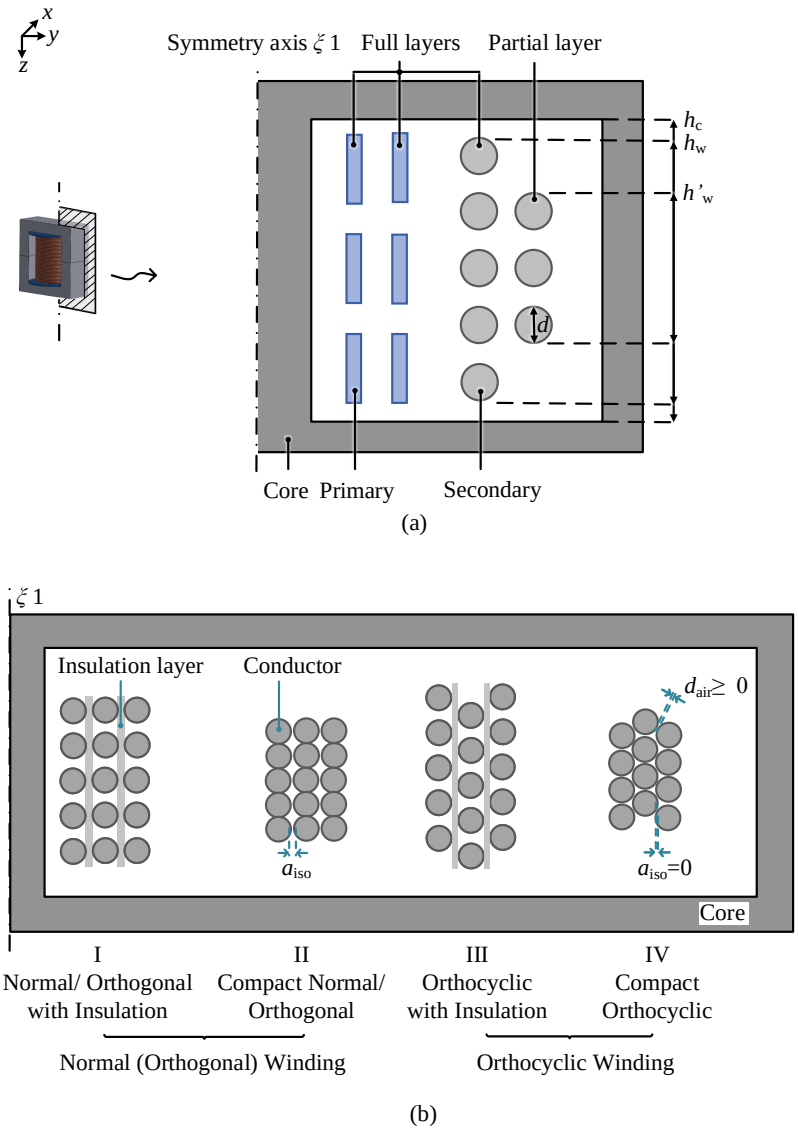

Fig. 3.1: Transformer winding configurations studied in this chapter: full and partial layer windings (a), normal and orthocyclic windings (b). [C1, J2, J3], [79, 96, 97]

control the wire turns accurately.

The impact of the orthocyclic windings on the resistance and leakage inductance is also not clear. As discussed in the previous chapter, the winding is usually designed and modeled as the normal winding configuration, i.e., type I & II in Fig. 3.1(b), but built as the orthocyclic winding, i.e., type III and IV. Dowell's model for winding

resistance is wire-position-independent. It assumes that the flux is parallel to winding height, which is in z direction in Fig. 3.1. When the porosity factor decreases, i.e., the ratio of the winding height to the window height, the flux is not straight anymore. It becomes two-dimensional, and the assumption becomes weak. Dowell's equation is not accurate anymore [112–116]. The orthocyclic winding also induces the two-dimensional effect. However, its impact on the ac resistance is not clear.

The leakage inductance is induced by the magnetic field the same with the ac resistance. There are mature models in low-frequency [117] and high-frequency range [1, 77, 118, 119]. Those formulas are also based on Dowell's one-dimensional flux assumption. For the orthocyclic winding with a two-dimensional field, its impact should be investigated.

To address those issues, this chapter studies the winding power loss and leakage inductance, which consists following major contributions:

- Propose an ac resistance model for the partial layer. Both the original and approximation equation are studied, the differences between them and Dowell's equation are analyzed in detail;
- Propose an orthocyclic coefficient for the ac resistance of orthocyclic windings, and compare the ac resistance of compact normal and orthocyclic windings;
- Propose the orthocyclic coefficient and new definition of inter-layer insulation for the leakage inductance of orthocyclic windings, and compare the leakage inductance of compact normal and orthocyclic windings.

3.2 Analytical Modeling: Power Loss of Partial Layer Windings

3.2.1 Dowell's Equation

The normal winding is defined occupying the full core window, and with orthogonal configuration, as the primary winding in Fig. 3.1(a) and the type I and II winding in Fig. 3.1(b). The classic ac resistance model for the normal winding is proposed by Dowell in 1966 and also named after him [77]

$$R_{\text{Dowell}} = R_{\text{dc}} F_{\text{Dowell}} \tag{3.1}$$

with

$$F_{\text{Dowell}} = \triangle[\varsigma + \frac{2}{3}(p^2 - 1)\xi] \tag{3.2}$$

$$\Delta = \frac{d_{\text{w}}}{\delta}\sqrt{\eta} \tag{3.3}$$

$$\varsigma = \frac{\sinh(2\triangle) + \sin(2\triangle)}{\cosh(2\triangle) - \cos(2\triangle)} \quad \xi = \frac{\sinh\triangle - \sin\triangle}{\cosh\triangle + \cos\triangle} \tag{3.4}$$

where R_{Dowell} and R_{dc} are the ac and dc winding resistance, respectively, F_{Dowell} is the ac resistance factor, Δ is the penetration ratio, η is the porosity factor and equals to

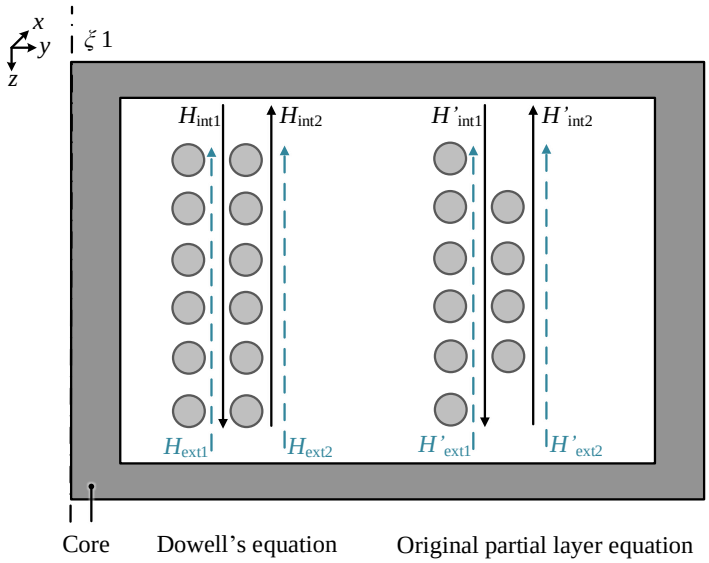

Fig. 3.2: The magnetic field intensity of different models. For Dowell's equation, H_{int1} and H_{int2} are the skin field intensities at the left and right side of the layer, while H_{ext1} and H_{ext2} are the proximity field intensities, respectively. The field intensities for the original partial layer equation are defined in a similar way. [J3], [97]

1 in the original Dowell's equation, d_{w} is the thickness of the foil, p is the number of layers, δ is the skin depth, ς and ξ are the skin and proximity coefficients, respectively.

Dowell's equation is initially for the foil winding. It is derived in a Cartesian coordinate system, and based on several assumptions:

- the foil occupies the full core window height in z direction;
- the magnetic field inducing the eddy current in the foil is one-dimensional and parallel to the foil, as shown in Fig. 3.2;
- in the core, the permeability is infinite, so the magnetic field intensity $H_{\text{core}} \approx 0$. Therefore, only the magnetic field in the window is considered.

Dowell's equation is extended to the rectangle wire and square wire with the porosity factor η, as illustrated in Fig. 3.3

$$\eta = \frac{t d_{\text{w}}}{h_{\text{c}}} = \frac{h_{\text{w}}}{h_{\text{c}}} \tag{3.5}$$

With the principle of the equivalent area transformation, it is also applicable for the round wire. The diameter of the wire d_{i} is transferred to the equivalent thickness d_{w}

$$d_{\text{w}} = \sqrt{\frac{\pi}{4}} d_{\text{i}} \tag{3.6}$$

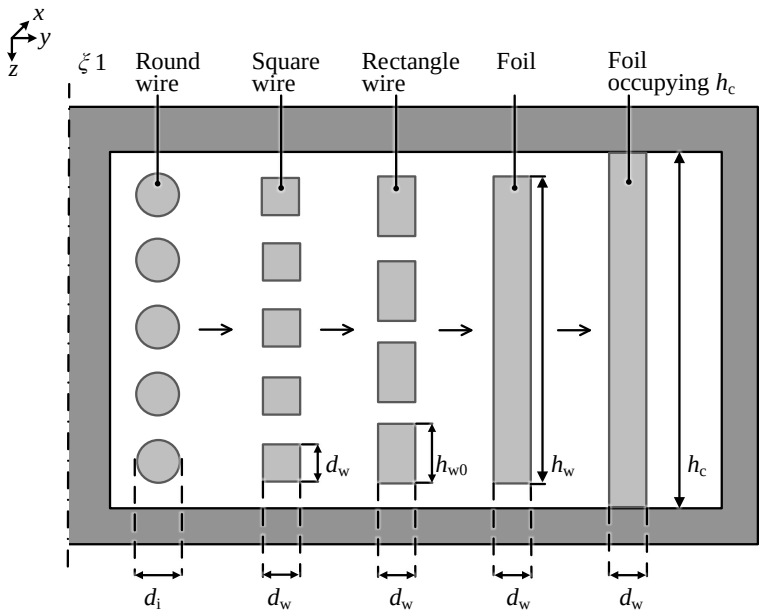

Fig. 3.3: The equivalent thickness transformation. The round wire with diameter d_i is transferred to the square shape wire, rectangle shape wire, foil, and foil occupying the whole window with the equivalent thickness d_w.

3.2.2 Original Partial Layer Equation

A partial winding consists of p full layers and one partial layer. h_{w0} is defined as the height of a single turn and equals to equivalent d_w for the round and rectangle wire. The height of full layer h_w and partial layer h'_w are

$$h_w = t h_{w0} \tag{3.7}$$

$$h'_w = t_0 h_{w0} \tag{3.8}$$

where t and t_0 are turns of full and partial layer, respectively. The partial coefficient k is defined by

$$k = \frac{t_0}{t} = \frac{h'_w}{h_w} \tag{3.9}$$

The magnetic field intensity of the Dowell's full layer equation and the original partial layer equation is illustrated in Fig. 3.2. The Magnetomotive Force (MMF) in the full layer F_m and in the partial layer F'_m are

$$F_m = t \cdot \hat{I_0} \tag{3.10}$$

$$F'_m = t_0 \cdot \hat{I_0} = \frac{t_0}{t} \cdot F_m = k F_m \tag{3.11}$$

where $\hat{I_0}$ is the peak current of each turn. Therefore for the partial layer, the internal skin effect field intensity is

$$H'_{\text{int1}} = -H'_{\text{int2}} = \frac{F'_{\text{m}}}{2h_{\text{c}}} = \frac{kF_{\text{m}}}{2h_{\text{c}}} \tag{3.12}$$

and the averaged external proximity field intensity is

$$H'_{\text{ext1}} = H'_{\text{ext2}} = \frac{\frac{pF_{\text{m}}}{h_{\text{c}}} + \frac{pF_{\text{m}}+kF_{\text{m}}}{h_{\text{c}}}}{2} = \frac{2pF_{\text{m}} + kF_{\text{m}}}{2h_{\text{c}}} \tag{3.13}$$

The MMF of the partial layer is k times than that of the full layer, while the field length is the same as h_{c}. So both internal skin effect and external proximity effect field intensity decrease.

With the magnetic field intensity as boundary conditions, the original partial layer equation with p full layers and one partial layer is derived in Appendix A.3

$$R_{\text{ori}} = R_{\text{dc}} F_{\text{ori}} \tag{3.14}$$

with

$$F_{\text{ori}} = \Delta\varsigma + \frac{4p^3 - 4p - 3k + 3k(2p+k)^2}{6(p+k)}\Delta\xi \tag{3.15}$$

When $k = 0$ or $k = 1$, this equation becomes Dowell's equation for p or $p+1$ full layers.

Finally, the partial layer causes a decrease of the field intensity H, which is different from the field intensity decrease due to the porosity factor η. k is defined as the partial layer height to the winding height, while η is the winding height to the core height. So k is to modify the relation between the partial layer height and the winding height, while η is to correct the field distortion resulted from the mismatch between the winding height and the window height, respectively. Therefore, there is no conflict between k and η.

3.2.3 Approximation of Partial Layer Equation

Combining Dowell's equation and the concept of partial coefficient, an approximation of the original partial layer equation is proposed in [97]

$$R_{\text{approx}} = R_{\text{dc}} F_{\text{approx}} \tag{3.16}$$

with

$$F_{\text{approx}} = \triangle[\varsigma + \frac{2}{3}(p_p^2 - 1)\xi] \tag{3.17}$$

$$p_p = p + k \tag{3.18}$$

where p_p is a fraction which represents the layers of the partial winding. The equation is simpler compared with the original equation. However, it has no theoretical support. Its accuracy is compared with the original equation in following sections.

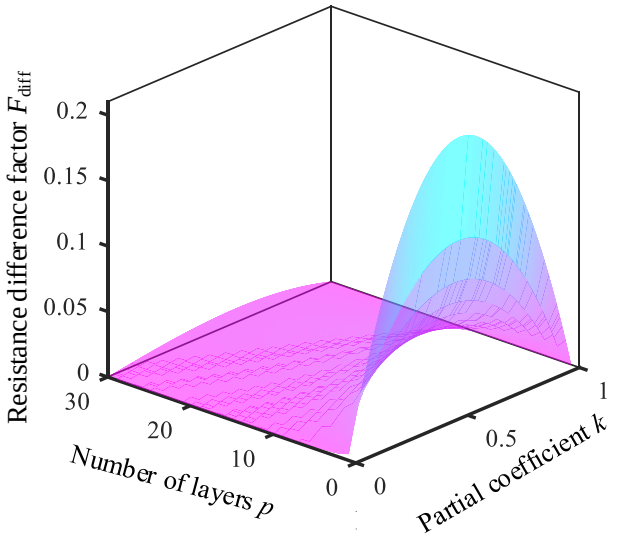

Fig. 3.4: Resistance factor F_{diff} changes with partial coefficient k and the number of layers p. F_{diff} is the maximum when ($k = 0.5$, $p = 1$). [J3], [97]

3.2.4 Difference Between Two Partial Layer Equations

The resistance difference R_{diff} between the original and approximation equation for the partial layer winding is defined as

$$\begin{aligned} R_{\text{diff}} = R_{\text{ori}} - R_{\text{approx}} &= R_{\text{dc}}(F_{\text{ori}} - F_{\text{approx}}) \\ &= R_{\text{dc}} F_{\text{diff}} = R_{\text{dc}} \frac{\Delta\xi(k - k^3)}{6(p + k)} \end{aligned} \tag{3.19}$$

where F_{diff} is defined as the resistance difference factor. Changing k from 0 to 1, and p from 0 to 30, the corresponding F_{diff} is illustrated in Fig. 3.4.

Assuming the number of layers p as a constant, F_{diff} first increases with k and then decreases. The maximum F_{diff} is obtained when the differential of F_{diff} with respect to k is zero ($\frac{\partial F_{\text{diff}}}{\partial k} = \frac{p(1-3k^2)-2k^3}{(p+k)^2} = 0$). The calculated k is

$$k_{max}(p) = \frac{1}{2}\left(\frac{p^2}{q} + q - p\right) \tag{3.20}$$

with

$$q = \sqrt[3]{-p^3 + 2\sqrt{p^2 - p^4}} \tag{3.21}$$

Change the value of p from 1 to 5000, $0.50 \leq k_{max}(p) \leq 0.58$. So the maximum F_{diff} is obtained when $0.50 \leq k_{max}(p) \leq 0.58$, which is approximately the half layer scenario. F_{diff} is the largest as 0.21 when $p = 1$, and then decreases with p. Therefore, the highest error using the approximate equation is $21\% R_{\text{dc}}$ when $p = 1$ and $k = 0.5$, then it decreases significantly with p.

Table 3.1: Winding specification of prototypes P1, P2, P3, and P4 used for Case Study 3

	Primary	Secondary				Unites
		P1	P2	P3	P4	
No. of partial layers	0	0	1	1	0	
Turns in partial layer t_0	0	0	10	20	0	
No. of full layers p	2	2	2	2	3	
Turns in full layer t	16	16	16	38	38	
Round wire Dia. d_i	1.56	1.56	1.56	0.62	0.62	mm

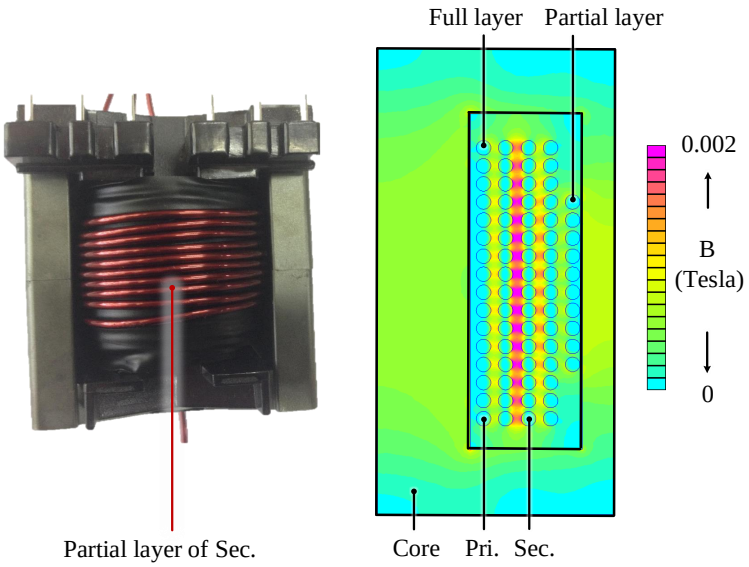

Fig. 3.5: Photo of Prototype P2 (c.f. Table 3.1) and its simulation result at 200 kHz. [C1, J3], [96, 97]

3.3 Case Study 3: Transformers with Partial Layer

Two subcases are performed in this section to verify the original and approximate equations for the partial layer winding. The first subcase is with two transformers named P1 and P2. They are with the same size core PQ50/50, same primary winding, but with and without partial layer as the secondary winding, as described in Table 3.1. The photo of P2 and the finite element simulation results at 200 kHz are shown in Fig. 3.5. The simulation is done in the software FEMM [92]. A comparison between P1 and P2 using the results from analytical calculation, simulation, and experiments is shown in Fig. 3.6. Aglient E5061B network analyzer is used to measure the primary side ac resistance of the transformer, while the transformer is short-circuited at the secondary side.

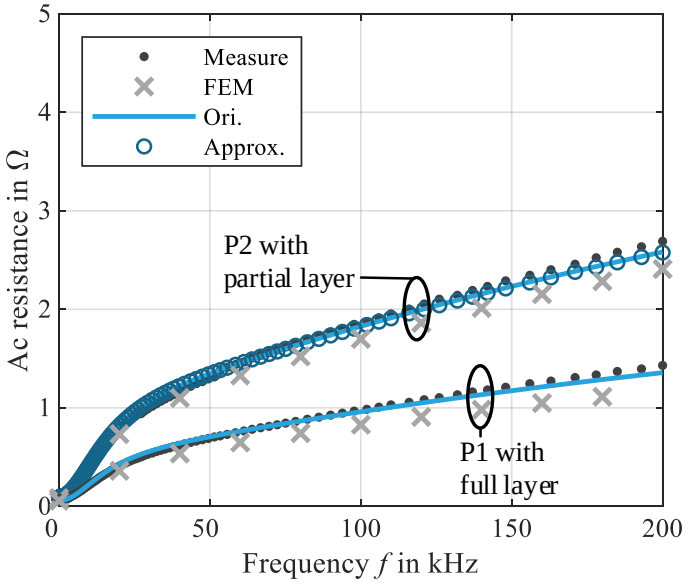

Fig. 3.6: Comparison of P1 and P2 ac resistance (c.f. Table 3.1) with the analytical (Ori. for original partial layer equation and Approx. for approximation of partial layer equation), simulation (FEM), and experiment (Measure) results. [C1, J3], [96, 97]

From the comparison, both original and approximate models fit the simulation and measurement results. The limited errors are from the one-dimensional analytical field assumption, the neglect of the three-dimensional effect in the two-dimensional simulation, and also measurement errors.

The ac resistance of P2 is significantly higher compared with P1, especially with the increase of frequency. Therefore, only using Dowell's equation for the transformer and neglecting the partial layer causes considerable errors with the increase of layer and frequency.

The transformer P3 with the same core as P1 is built for the second subcase study. Its winding configuration is given in Table 3.1. The analytical, simulation, and experiment results are shown in Fig. 3.7. They agree with each other in the whole frequency range. P4 with the same winding and core parameters as P3 except that there are three full layers in the secondary winding, are also shown in Fig. 3.7 for comparison. Its winding configuration is also in Table 3.1. The wire diameter in the secondary is 0.62 mm, so the eddy current effect is negligible below 100 kHz. The differences between P3 and P4 below 100 kHz are negligible. This difference increases along with the frequency, which indicates the importance of the partial layer equation in the high-frequency range.

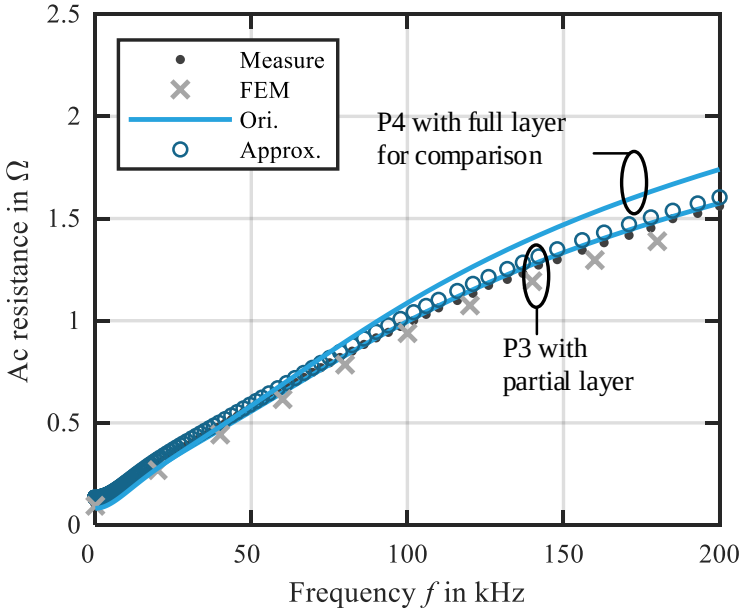

Fig. 3.7: Comparison of P3 and P4 ac resistance (c.f. Table 3.1) with the analytical (Ori. for original partial layer equation and Approx. for approximation of partial layer equation), simulation (FEM), and experiment (Measure) results. [J3], [97]

3.4 Analytical Modeling: Power Loss of Orthocyclic Windings

During the winding wiring process, it is difficult to fix the position of round wires due to their curved edges. With the increase of turns and layers, the wire can displace from normal position (Fig. 3.1(b) I and II) to orthocyclic (Fig. 3.1(b) III and IV). The winding volume decreases approximately 13.4 %. It also causes the distortion of magnetic fields, as shown in Fig. 3.8(b).

The field intensity H of the orthocyclic winding is modified by the field ratio $k_c(\Delta, \eta)$

$$H = \frac{F_m}{h_c \cdot k_c(\Delta, \eta)} \tag{3.22}$$

where F_m is the magnetomotive force, Δ and h_c are the penetration ratio and core window height defined in Dowell's equation (3.1, 3.2, 3.3, 3.4), respectively. $k_c(\Delta, \eta)$ is a function of the frequency f, which is positive proportional to the penetration ratio Δ. $k_c(\Delta, \eta)$ is also a function of η, because the decrease of η causes the severe field distortion, as illustrated in Fig. 3.8(b). $k_c(\Delta, \eta)$ at different frequency range and porosity factor is summarized in Table 3.2 and explained below.

Dowell's equation (3.1) is originally for the normal winding type I and II. It as-

Table 3.2: Field ratio k_c at different penetration ratio Δ and porosity factor η [J2], [79]

Winding type	I & II & III	IV
$k_c(\mathrm{LF}, \eta)$	1	1
$k_c(\mathrm{HF}, 0.5)$	≈ 1	$\pi/2$
$k_c(\mathrm{HF}, 1)$	≈ 1	$\pi/3$
$k_c(\mathrm{HF}, \eta)$	≈ 1	$2\eta \arcsin \frac{1}{2\eta}$

LF : low freq., $\Delta \ll 1$.
HF : high freq., $\Delta \gg 1$.
Winding types I, II, III, and IV refers to Fig. 3.1(b).

sumes the magnetic field line is one-dimensional and in window height direction. In the low-frequency (LF) range, the eddy current effect is not severe, and the magnetic field passes through the wire directly. So this assumption works well for all winding types. Therefore, $k_c(\mathrm{LF}, \eta) = 1$ for all winding types I to IV in Table 3.2.

As the increase of frequency, the eddy current is non-negligible. It generates the magnetic field against the external field. Generally, the external field looks like being pushed out of the wire area and distorts, as shown in Fig. 3.8(b). For winding type I, II, and III, $k_c \approx 1$. For winding type IV, when it comes to the high-frequency (HF) range and $\Delta \gg 1$, k_c(HF,η) at $\eta = 0.5$ and $\eta = 1$ is calculated according to the field distribution in Fig. 3.8(b), which is $\frac{\pi}{2}$ and $\frac{\pi}{3}$, respectively. When $0.5 \leq \eta \leq 1$, k_c(HF,η) is located between $\frac{\pi}{2}$ and $\frac{\pi}{3}$, and it is calculated as $2\eta \arcsin \frac{1}{2\eta}$ according to structural relationship.

In conclusion, for winding type IV, in low frequency range ($\Delta \ll 1$), $k_c = 1$; in high frequency range ($\Delta \gg 1$), $k_c = 2\eta \arcsin \frac{1}{2\eta}$. The field distortion also affects the ac resistance. Two transformers are designed for comparison and named O1 and O1o, respectively. Their winding configurations are in Table 3.3, and the winding porosity factor η is 0.6. They are with the same wire, core, and winding configuration except that O1 is with normal winding, and O1o is with orthocyclic winding. Define the ac resistance factor of orthocyclic winding $F_{r,o}$, the ac resistance factor of normal winding as $F_{r,n}$. Their ratio $F_{r,o}/F_{r,n}$ from the simulation results is illustrated in Fig. 3.9 as the circles. Increasing or decreasing their number of turns per layer t, $\eta = 0.8$ and 0.5 scenarios are also simulated and illustrated.

To compensate the field distortion analytically, the field ratio $k_c(\Delta, \eta)$ can be used to further adjust the equivalent window height $h_{c,eq}$. A orthocyclic coefficient $k_h(\Delta, \eta)$ is defined, combining the field coefficient $k_c(\Delta, \eta)$, and also curve fitting the simulation results in Fig. 3.9 with a hyperbolic function

$$\begin{aligned} & k_h(\Delta, \eta) \\ &= \frac{1/k_c(\mathrm{HF}, \eta)^2 - 1}{2} \tanh\left(\frac{\Delta - 4}{1.5}\right) + \frac{1/k_c(\mathrm{HF}, \eta)^2 + 1}{2} \\ &= \frac{\frac{1}{(2\eta \arcsin \frac{1}{2\eta})^2} - 1}{2} \tanh\left(\frac{\Delta - 4}{1.5}\right) + \frac{\frac{1}{(2\eta \arcsin \frac{1}{2\eta})^2} + 1}{2} \end{aligned} \tag{3.23}$$

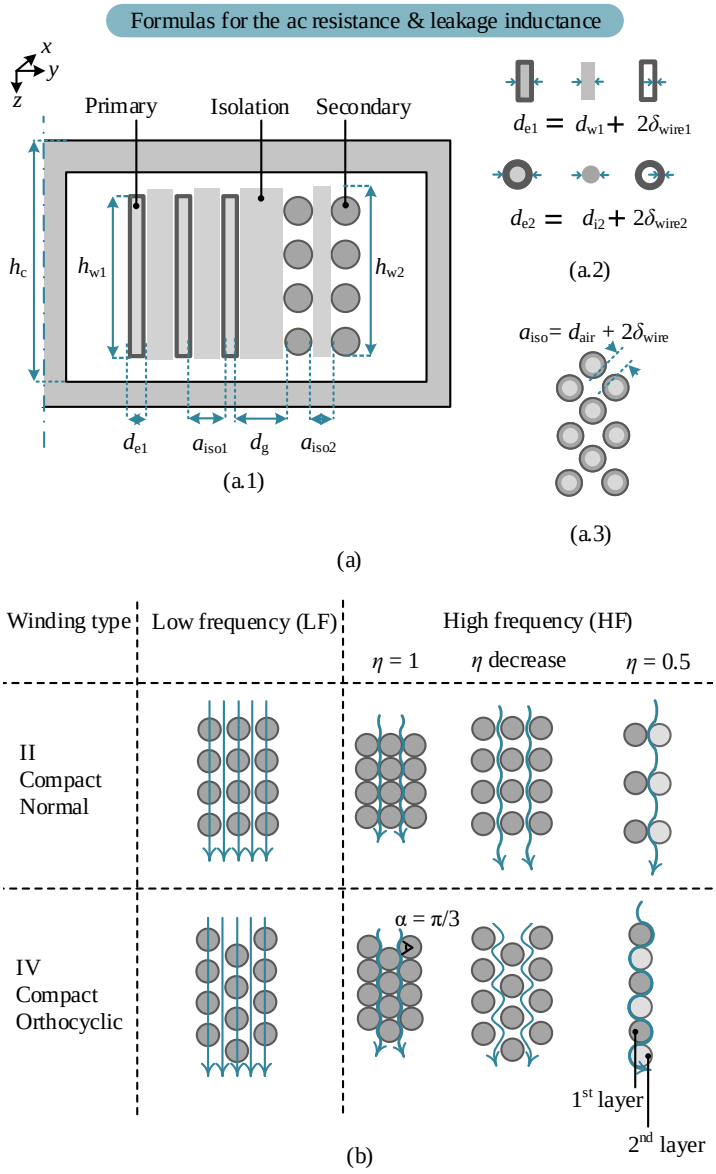

Fig. 3.8: Ac resistance and leakage inductance for different winding types. (a.1) Cross-section of a transformer and the dimension definition. (a.2) Dimension definition of primary (subscripts of 1) and secondary (subscripts of 2) winding. (a.3) Proposed new definition of the inter-layer insulation a_{iso} for orthocyclic winding type IV. (b) Magnetic field of different winding types at low and high frequency. (c) Ac resistance and leakage inductance formulas of different winding types. [J2], [79] [sub-figures #1/2]

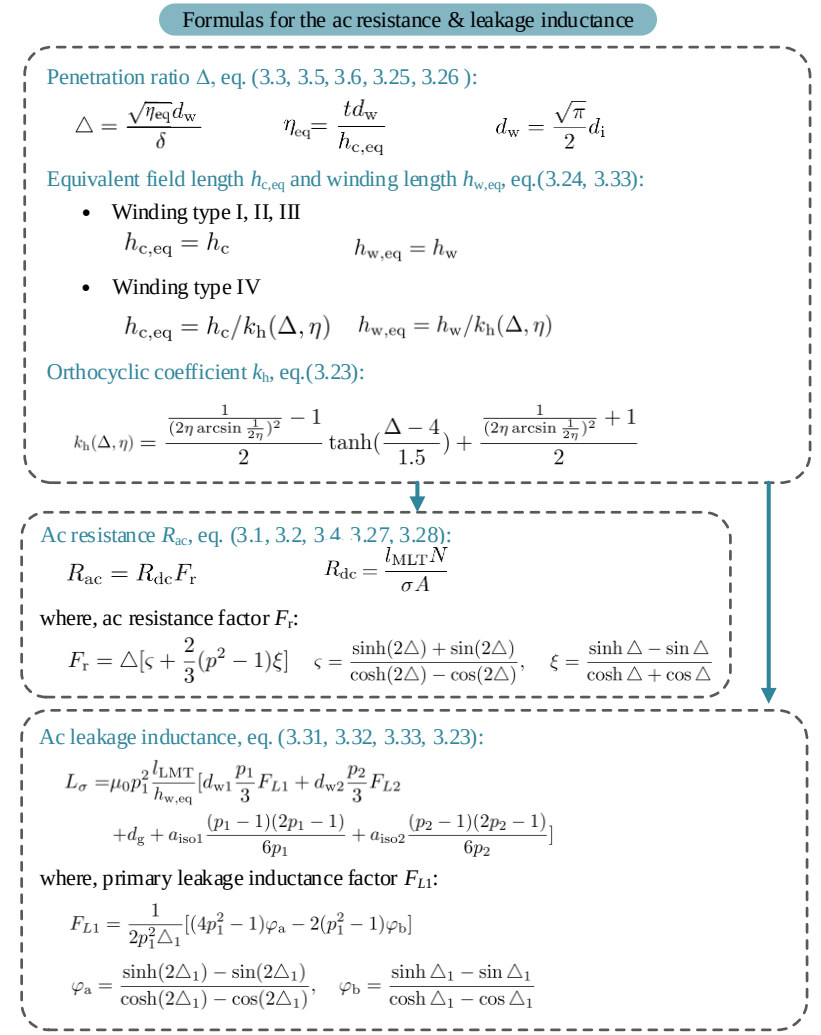

- l_{MLT} : the mean length per turn
- N : the number of turns
- σ : the conductivity of the wire
- A : the cross section area of each turn
- Δ : the penetration ratio of the wire
- η : the porosity factor
- p : the number of layers
- d_i : the bare diameter of the round wire without coating
- d_w : the width of the foil without coating
- δ : the skin depth
- μ_0 : the permeability of air
- t : the number of turns per layer
- h_c : the height of the core window
- h_w : the height of the winding
- d_g : the thickness of the inter-winding insulation
- a_{iso} : the inter-layer insulation distance in width direction, including wire coating, air gap, and layer insulation
- F_{L2} : the secondary leakage inductance factor, similar to F_{L1} except p_1 and Δ_1 are replaced by p_2 and Δ_2

(c)

Fig. 3.8: [cont. sub-figures #2/2]

Table 3.3: Transformers with normal and orthocyclic windings for Case Study 4 & 5 [J2], [79]

Parameters	O1/ O1o	O2/ O2o	O3/ O3o	Units
ETD core size	59/31/22	59/31/22	29/16/10	
Pri./Sec. p	3	3	3	
Turns per layer t	34	30	20	
Round wire Dia. d_{i}	1.0	0.9	0.75	mm
Inter-winding Insu. d_{g}	0.8	0.4	0.2	mm
Inter-layer Insu. a_{iso}	0.2	0.1	0.1	mm

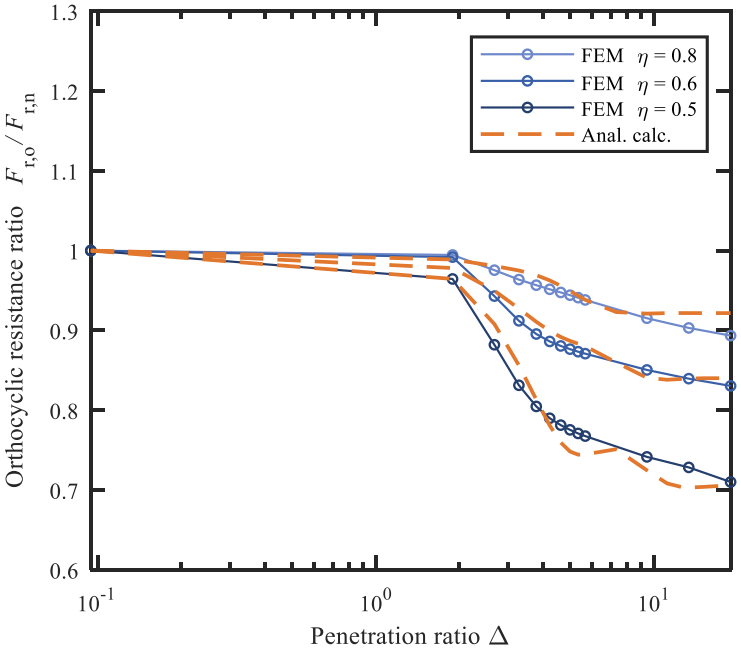

Fig. 3.9: The resistance factor ratio of orthocyclic and normal windings $F_{\mathrm{r,o}}/F_{\mathrm{r,n}}$. The simulation results are given as blue circles. The dashed line represents the results of the proposed equation. [J2], [79]

(3.23) can also be other forms as long as they fit the simulation curve in Fig. 3.9.

So the field length is equivalent to the effective height of core $h_{\mathrm{c,eq}}$

$$h_{\mathrm{c,eq}} = h_{\mathrm{c}}/k_{\mathrm{h}}(\Delta, \eta) \tag{3.24}$$

With the modified effective window height, the equivalent porosity factor is

$$\eta_{\mathrm{eq}} = \frac{td_{\mathrm{w}}}{h_{\mathrm{c,eq}}} \tag{3.25}$$

Taking the equivalent porosity factor η_{eq} in the penetration ratio (3.3)

$$\Delta = \frac{d_{\text{w}}}{\delta}\sqrt{\eta_{\text{eq}}} \tag{3.26}$$

and the skin and proximity coefficient (3.4) as

$$\varsigma = \frac{\sinh(2\triangle) + \sin(2\triangle)}{\cosh(2\triangle) - \cos(2\triangle)} \quad \xi = \frac{\sinh\triangle - \sin\triangle}{\cosh\triangle + \cos\triangle} \tag{3.27}$$

the modified ac resistance factor $F_{\text{r,o}}$ is obtained with (3.2)

$$F_{\text{r,o}} = \triangle[\varsigma + \frac{2}{3}(m^2 - 1)\xi] \tag{3.28}$$

The orthocyclic coefficient and corresponding equations are summarized in Fig. 3.8.

3.5 Case Study 4: Ac Resistance of Normal and Orthocyclic Winding Transformers

Three subcase study is performed, with transformers of different core sizes and porosity factors η, to verify the proposed resistance model.

- Case 4.1: ETD 59/31/22 core, $\eta = 0.6$

  O1 and O1o discussed previously are used as the first subcase study. In reality, building a normal winding transformer is difficult, so only O1o is built and tested, as shown in Fig. 3.10(a). The simulation results of O1 and O1o are also compared in Fig. 3.10(b, c, d, e). Their magnetic flux distribution matches well with the theoretical analysis in Fig. 3.8(b). Their comparison with the analytical, simulation, and experimental results are shown in Fig. 3.11 (a, b). Building the ideal compact orthocyclic winding is difficult in reality. Therefore, O1o is in the winding position between winding type II and IV. The measured ac resistance of O1o also locates between the simulated results of the O1 and O1o.

- Case 4.2: ETD 59/31/22 core, $\eta = 0.5$

  Case 4.2 designs O2 and O2o, as illustrated in Table 3.3. They use the same core as O1/O1o in Case 4.1, however, with smaller number of turns per layer and wire diameter. The porosity factor $\eta_0 = 0.5$. Their comparison are illustrated in Fig. 3.11 (c, d). Compared with Case 4.1, Case 4.2 is with a lower porosity factor, while the proposed equations show smaller error than the original Dowell's equation.

- Case 4.3: ETD 29/16/10 core, $\eta = 0.6$

  Case 4.3 designs two transformers with normal and orthocyclic windings but with a smaller ETD 29/16/10 core, and their winding configurations are given in Table 3.3. A comparison of the ac resistance is given in Fig. 3.11 (e, f). Again the measured results are located between the simulation of normal and orthocyclic winding configurations, and the proposed equation achieves better accuracy.

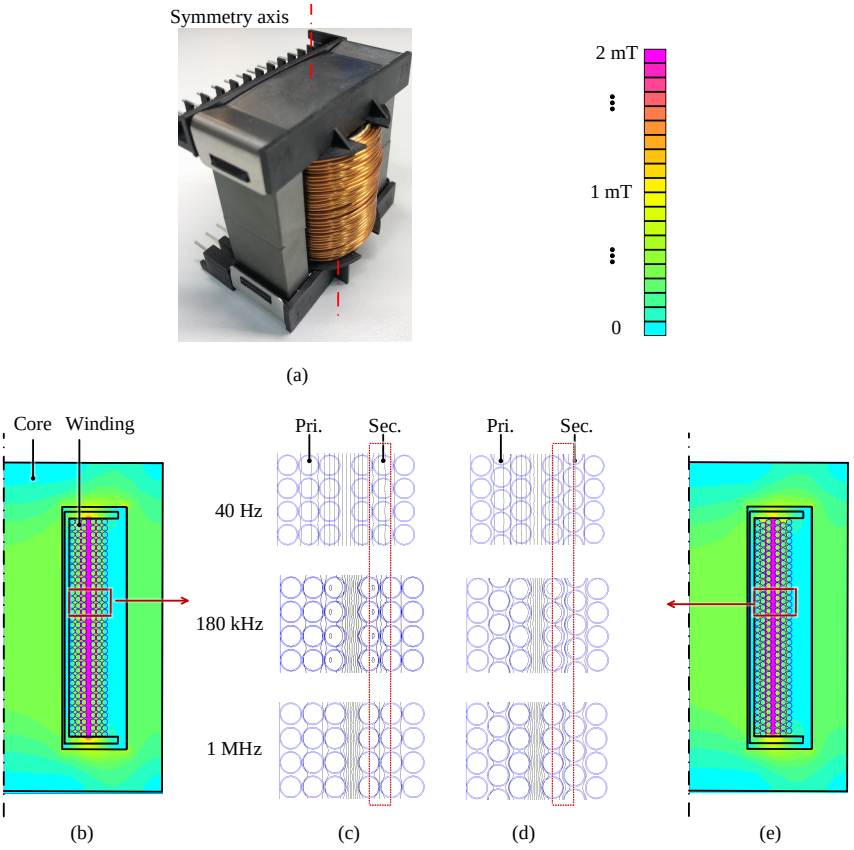

Fig. 3.10: Photo and simulation of the prototype O1 and O1o with normal and orthocyclic windings (c.f. Table 3.3). (a) is photo of O1o. (b, e) are the magnetic field simulations of O1 and O1o at 180 kHz, (c, d) are their zoom-in view at different frequencies. The magnetic field in the red dotted frame in (c, d) verifies the field analysis in Fig. 3.8(b). [J2], [79]

In conclusion, the proposed equation is with smaller error for the compact orthocyclic winding type IV, especially with the increase of the frequency and decrease of the porosity factor. Compared with the experiment results in three sub-cases, the maximum error of Dowell's equation is 24.4%, while it is 8.6% for the proposed equation.

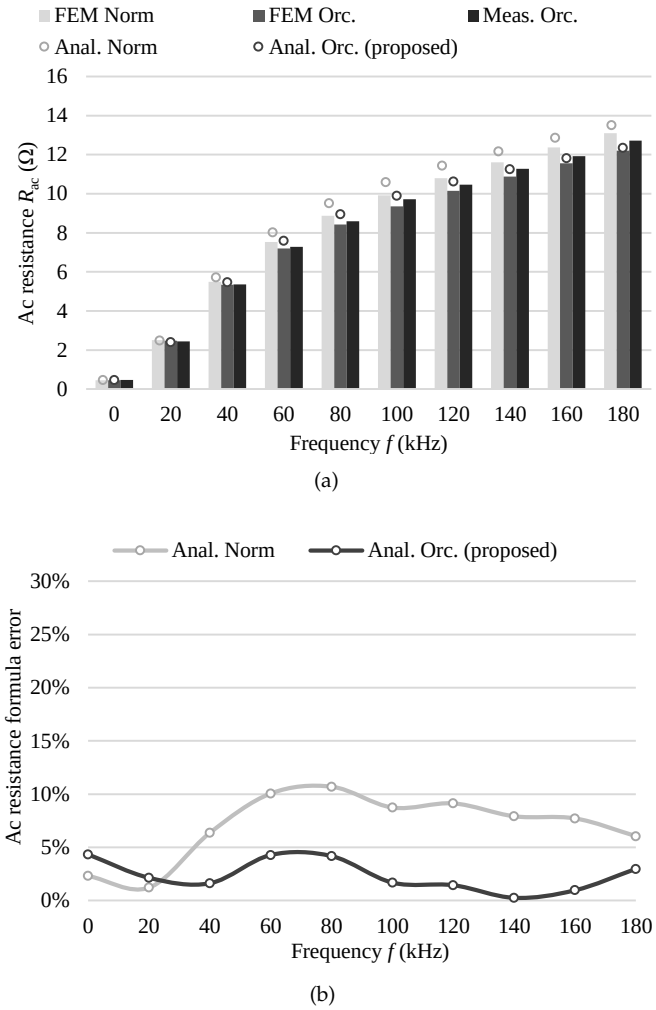

Fig. 3.11: Ac resistance and error comparison of prototype O1/O1o, O2/O2o, and O3/O3o with normal and orthocyclic windings (c.f. Table 3.3). (a) The FEM, analytical, and experimental results of O1 with normal winding (Norm.) and O1o with orthocyclic winding (Orc.). O1 and O1o are with the same core, winding dimension, and insulation, except for the winding type. Their difference in the mean length per turn (MLT) due to different winding types is 0.54% which is negligible. Therefore their different results are mainly due to the winding type. (b) Error analysis of different formulas compared with the experimental measurement. (c, d) Ac resistance and error analysis of O2 and O2o. (e, f) Ac resistance and error analysis of O3 and O3o. [J2], [79] [sub-figures #1/3]

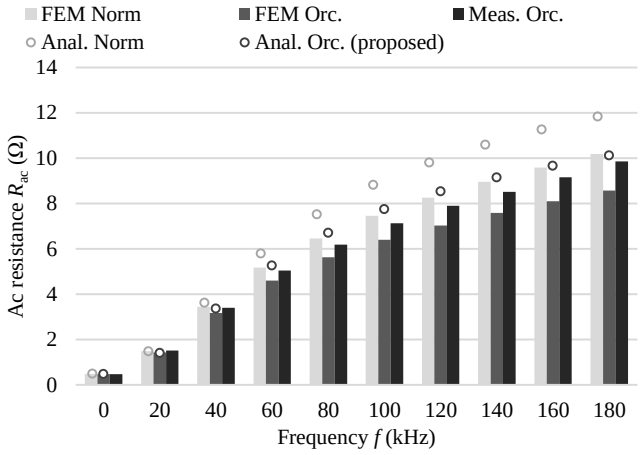

(c)

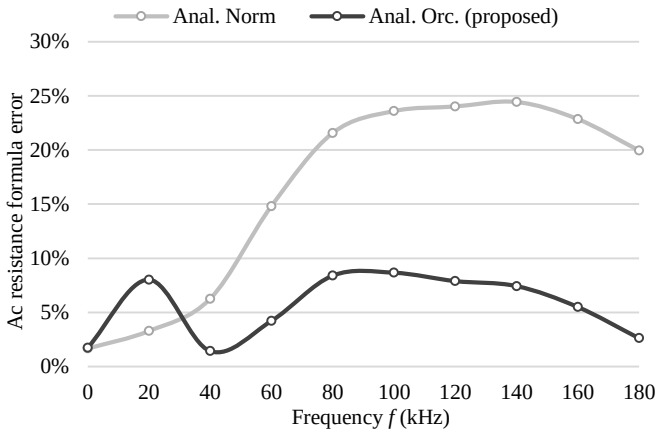

(d)

Fig. 3.11: [cont. sub-figures #2/3]

3.6 Orthocyclic Resistance Ratio

To compare the impact of the orthocyclic winding to the ac resistance, the orthocyclic resistance ratio k_r is defined as

$$k_\mathrm{r} = \frac{F_\mathrm{r,o}}{F_\mathrm{r,n}} \cdot 100\% \tag{3.29}$$

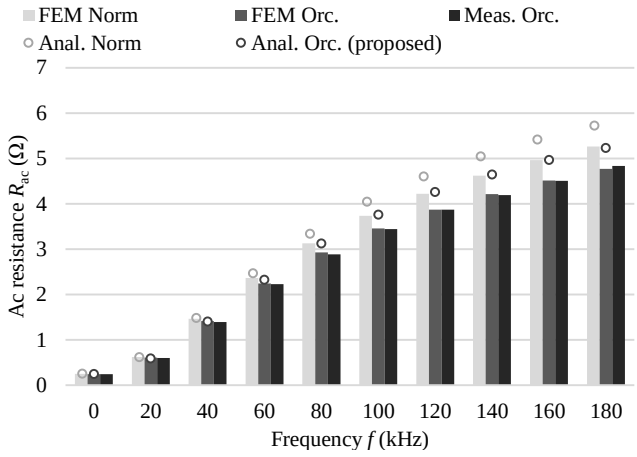

(e)

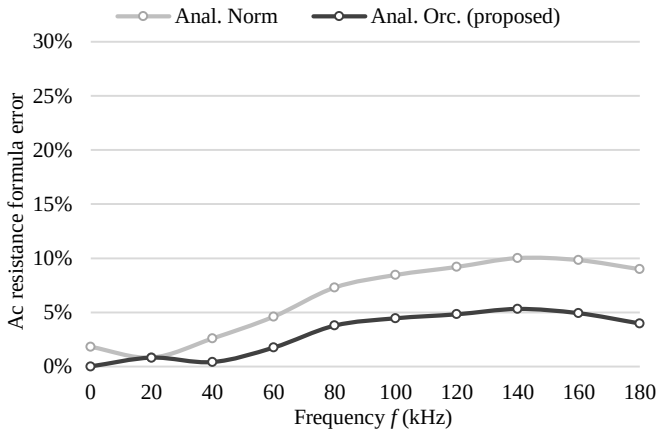

(f)

Fig. 3.11: [cont. sub-figures #3/3]

where $F_{r,o}$ and $F_{r,n}$ are the ac resistance ratio of the compact orthocyclic and normal winding with the same winding and wire dimensions, respectively.

By changing the penetration ratio $\triangle$ and porosity factor η, k_r is calculated in Fig. 3.12. Several conclusions are obtained:

- Due to the field distortion, the compact orthocyclic winding is with smaller ac resistance against compact normal winding considering the same wire diameter and wire coating;
- The difference of ac resistance between compact orthocyclic and normal wind-

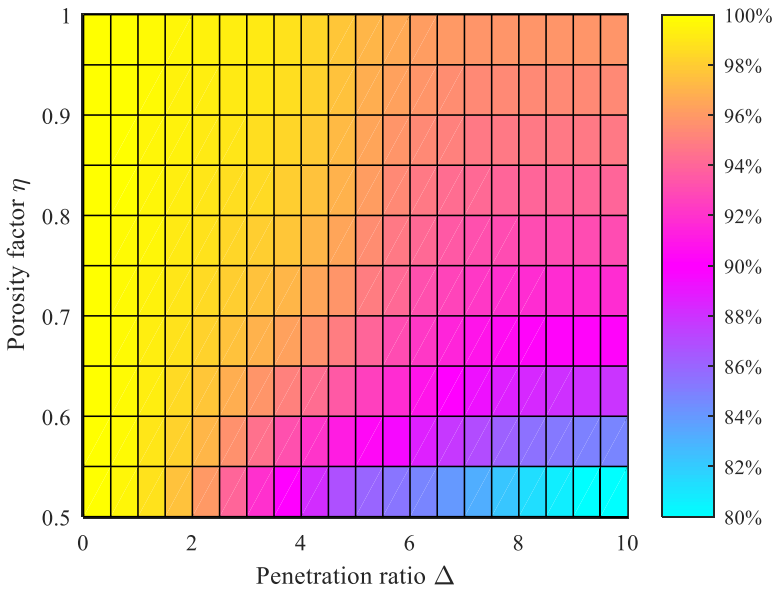

Fig. 3.12: The orthocyclic resistance ratio k_r changes with the penetration ratio Δ and porosity factor η. For the simplification of comparison, the air-gap distance d_{air} is set as 0 for both windings. The number of layers $p = 5$ in the presented case. When changing p from 1 to 20, the related k_r is similar and this mapping does not change significantly. [J2], [79]

ing is non-negligible with the decrease of the porosity factor and increase of the penetration ratio (also the frequency), and it is not relevant to the number of layers p.

- k_r reaches minimum 80% when the penetration ratio $\triangle = 10$ and the porosity factor $\eta = 0.5$.

3.7 Analytical Modeling: Leakage Inductance of Orthocyclic Windings

3.7.1 Leakage Inductance of Normal Winding

The analytical modeling of the leakage inductance is based on the integration of magnetic field energy storing in the window and winding area. The classic low-frequency leakage inductance formula dose not consider the eddy current effect and is frequency-independent [2]

$$L_\sigma = \mu_0 p_1^2 \frac{l_{LMT}}{h_w}(d_g + \frac{d_c - d_g}{3}) \tag{3.30}$$

where μ_0 is the air permeability, l_{LMT} is the mean length per turn, p_1 is the layers of primary winding, h_w is the winding height, d_g is insulation distance between primary

and secondary, d_c is the window width, respectively.

Taking the eddy current into consideration, the high-frequency leakage inductance formula is with both the frequency-dependent and frequency-independent parts [77, 120, 121]

$$\begin{aligned} L_\sigma =& \mu_0 p_1^2 \frac{l_{\mathrm{LMT}}}{h_{\mathrm{w,eq}}} [\underbrace{d_{\mathrm{w1}} \frac{p_1}{3} F_{L1} + d_{\mathrm{w2}} \frac{p_2}{3} F_{L2}}_{\text{freuqncy dependent}} \\ & \underbrace{+ d_{\mathrm{g}} + a_{\mathrm{iso1}} \frac{(p_1-1)(2p_1-1)}{6p_1} + a_{\mathrm{iso2}} \frac{(p_2-1)(2p_2-1)}{6p_2}}_{\text{freuqncy independent}}] \end{aligned} \tag{3.31}$$

where

$$\begin{aligned} & F_{L1} = \frac{1}{2p_1^2 \triangle_1} [(4p_1^2 - 1)\varphi_{\mathrm{a}} - 2(p_1^2 - 1)\varphi_{\mathrm{b}}], \\ & \varphi_{\mathrm{a}} = \frac{\sinh(2\triangle_1) - \sin(2\triangle_1)}{\cosh(2\triangle_1) - \cos(2\triangle_1)}, \quad \varphi_{\mathrm{b}} = \frac{\sinh \triangle_1 - \sin \triangle_1}{\cosh \triangle_1 - \cos \triangle_1} \end{aligned} \tag{3.32}$$

F_{L1} is the leakage inductance factor, and the subscript 1 indicates the primary winding. Other parameter definitions are summarized in Fig. 3.8. The high-frequency leakage formula considers the eddy current, and it is in the focus of this study.

3.7.2 Leakage Inductance of Orthocyclic Winding

The leakage inductance is generated by the same magnetic field as the ac resistance. The flux in the wire contributes to the frequency-dependent part in (3.31), while the flux in the insulation contributes to the frequency-independent part. So the field analysis for the orthocyclic winding in Fig. 3.8(b) is also applied here. In (3.31), the length of the field is represented by the winding height h_{w}. It is modified by the orthocyclic coefficient and becomes the equivalent winding height

$$h_{\mathrm{w,eq}} = h_{\mathrm{w}} / k_{\mathrm{h}}(\Delta, \eta) \tag{3.33}$$

For the flux in the insulation, the orthocyclic winding not only impacts the flux in height direction (z axis) but also in the width direction (y axis). In Fig. 3.1, the interlayer insulation distance a_{iso} of the winding type IV is zero according to its definition. However, it does not in line with reality. The flux can still zigzag from one turn to the next, as shown in Fig. 3.8(b). Therefore, the flux width cannot be defined as a_{iso} with the original definition. Instead, the new definition of a_{iso} is given in Fig. 3.8(a.3). It is the direct distance between the two turns in adjacent layers, not purely in the width direction.

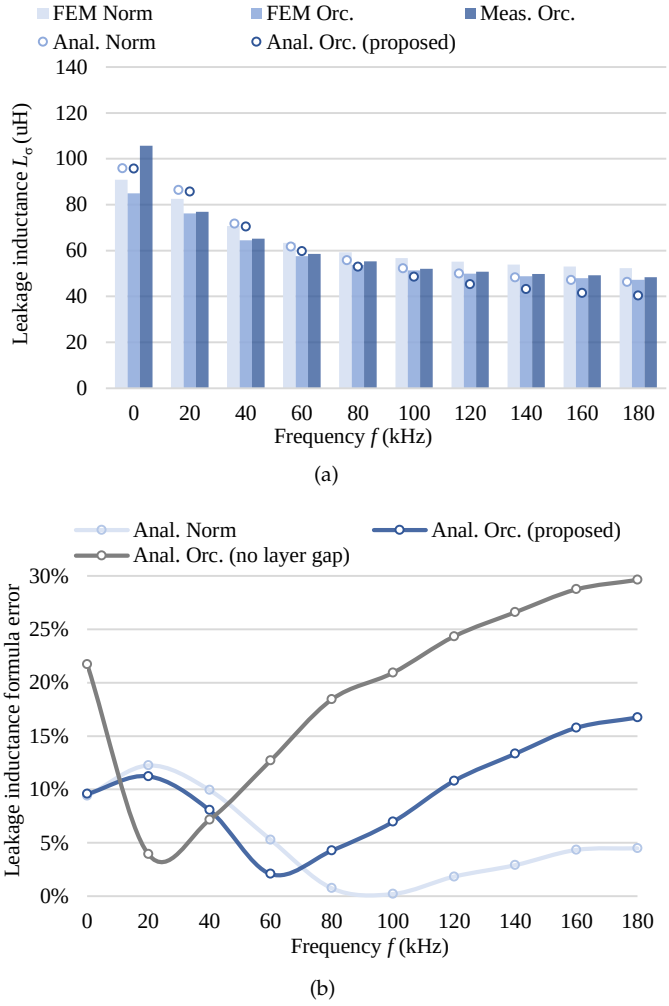

Fig. 3.13: Leakage inductance and error comparison of prototype O1/O1o, O2/O2o, and O3/O3o with normal and orthocyclic windings (c.f. Table 3.3). (a) The FEM, analytical, and experimental results of O1 with normal winding (Norm.) and O1o with orthocyclic winding (Orc.). (b) Error analysis of the different formulas compared with experimental results. (c, d) Leakage inductance and error analysis of O2 and O2o. (e, f) Leakage inductance and error analysis of O3 and O3o. [J2], [79] [sub-figures #1/3]

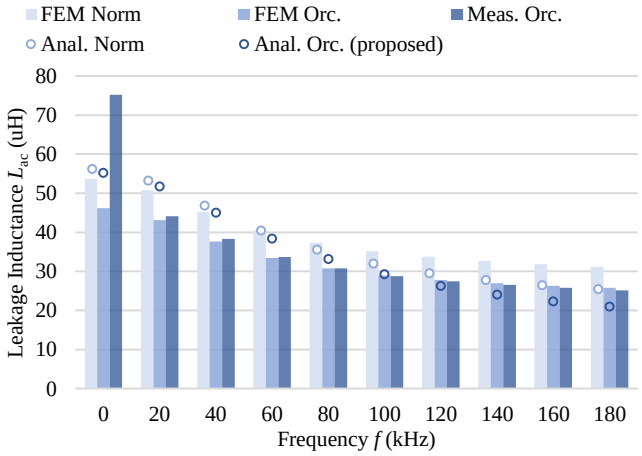

(c)

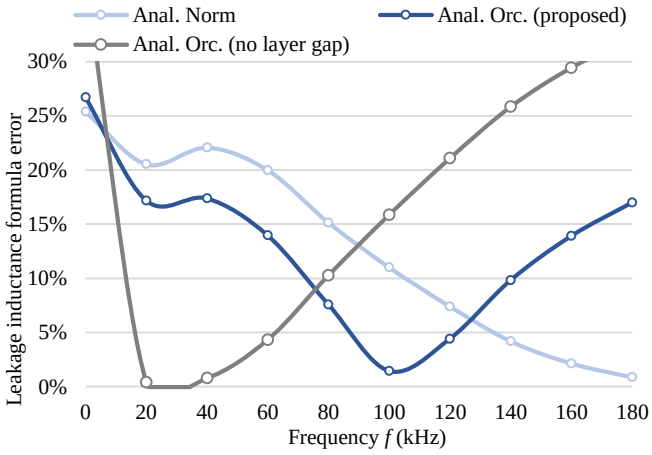

(d)

Fig. 3.13: [cont. sub-figures #2/3]

3.8 Case Study 5: Leakage Inductance of Normal and Orthocyclic Winding Transformers

Transformers in Table 3.3 are also used as the Case Study 5 to verify the proposed modified leakage inductance formulas. The calculated, simulated, and tested leakage inductance of O1/ O1o, O2/ O2o, and O3/ O3o are shown in Fig. 3.13.

O*i* and O*i*o are designed and built with the same core, wire diameter, and in-

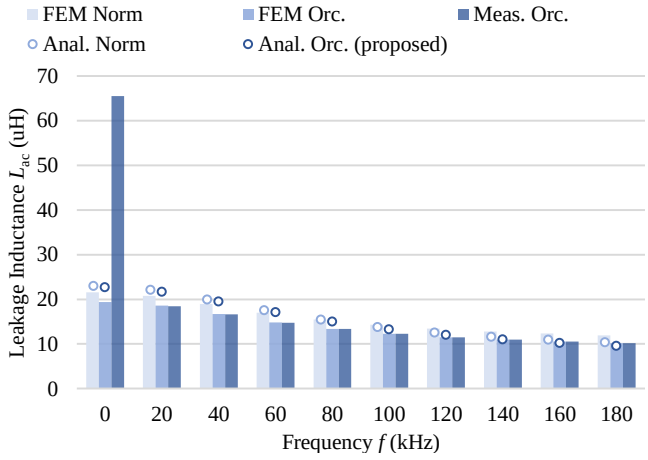

(e)

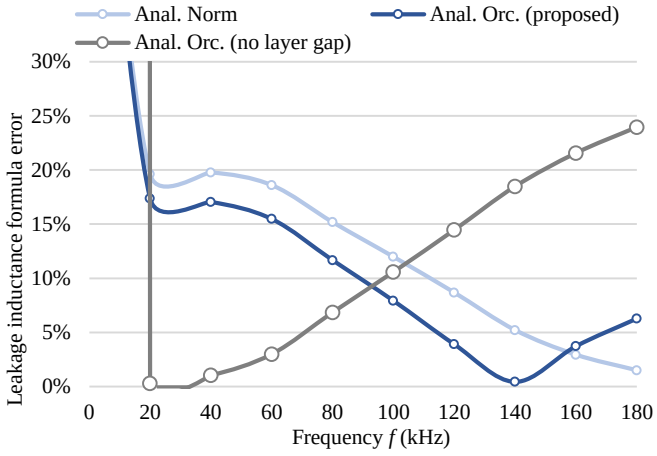

(f)

Fig. 3.13: [cont. sub-figures #3/3]

sulation distance (including inter-winding distance d_g and inter-layer distance a_{iso}). They are only with different winding types: compact normal and compact orthocyclic windings, respectively. The normal winding results (Norm.) are calculated for Oi with (3.31); while the orthocyclic winding results (Orc.) are calculated for Oio with (3.31), (3.33), and the new definition of a_{iso}.

Without the new definition of a_{iso}, the value of original a_{iso} equals to 0 in this case. The orthocyclic winding calculated with (3.31), (3.33), and the original definition of a_{iso} is also presented, as Anal. Orc. (no layer gap) in the error analysis.

Again, the wire position of built prototype Oio is located between the type II

and IV, so its measurement results are also located between the simulation results of those two types windings, but more close to winding type IV. In DC and low-frequency range, the measurement is not accurate. This is because the impedance of the main inductance in this frequency range decreases, and it impacts the short-circuit inductance. So the short-circuit inductance is not the leakage inductance anymore.

From comparison and error analysis in Fig. 3.13, both the normal winding equation for normal winding and proposed orthocyclic winding modification for orthocyclic winding achieves good accuracy. However, if using the normal winding equation for the orthocyclic winding without modifying the definition of inter-layer insulation a_{iso}, there are significant errors.

3.9 Orthocyclic Leakage Inductance Ratio

Similar to the orthocyclic capacitance and ac resistance ratio, the orthocyclic leakage inductance ratio k_l is also defined to compare the difference between the compact orthocyclic winding and normal winding

$$k_\text{l} = \frac{\mu_0 p_1^2 \frac{l_\text{w}}{h_{\text{w,o}}} [d_{w1} \frac{p_1}{3} F_{L1,o} + d_{i1} \frac{(p_1-1)(2p_1-1)}{6p_1}]}{\mu_0 p_1^2 \frac{l_\text{w}}{h_{\text{w,n}}} [d_{w1} \frac{p_1}{3} F_{L1,n} + d_{i1} \frac{(p_1-1)(2p_1-1)}{6p_1}]} \cdot 100\% \tag{3.34}$$

only the leakage flux in the primary winding area is considered and compared for the sake of generalization. The parameters with the subscripts o and n stand for the compact orthocyclic and normal winding, respectively. The ratio with the change of the penetration ratio Δ and porosity factor η is shown in F.g. 3.14, from where several conclusions are obtained:

- Generally, if every parameter is the same except for the winding type, the leakage inductance of the compact orthocyclic winding is smaller than compact normal winding.
- With the increase of the penetration ratio (also the frequency) and decrease of the porosity factor, the difference between the compact orthocyclic and normal winding is non-negligible. Besides, the number of layers p and radius ratio k_rad (defined in Section 2.5 as $k_\text{rad} = d_\text{e}/d_\text{i}$) are with negligible impact on the difference.
- The orthocyclic leakage inductance ratio k_l drops to minimum 65 % when ($\triangle = 10, \eta = 0.5, k_\text{rad} = 2, p = 20$).

3.10 Conclusions

This chapter studies the magnetic field modeling of magnetic components, and focuses on the winding resistance and leakage inductance models. An ac resistance model for a partial layer winding is studied. Its approximation model is also proposed, achieving the maximum error of $21\% R_\text{dc}$ in the analytical analysis. Moreover, the distortion of the magnetic field in the orthocyclic winding is investigated. An

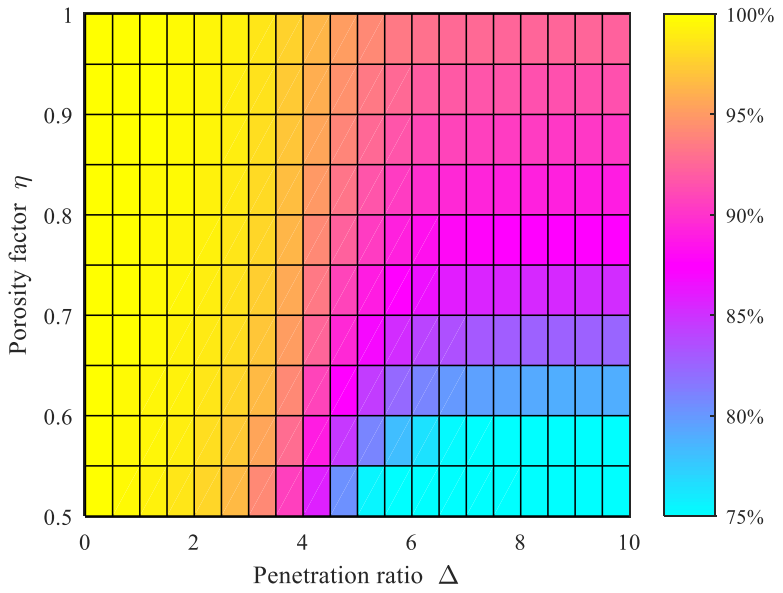

Fig. 3.14: The orthocyclic leakage inductance ratio k_{l} changes with the penetration ratio Δ and porosity factor η. For the simplification of comparison, the air-gap distance $d_{\mathrm{air}} = 0$ for both windings. The number of layers $p = 5$ in the presented case. When changing p from 1 to 20, the related k_{l} is similar, but this mapping does not change significantly. The radius ratio $k_{\mathrm{rad}} = 1.1$ in the presented case, and the $k_{\mathrm{l}} < 0.8$ area is $(\triangle > 5.5, \eta < 0.55)$. When k_{rad} changes to 2.0, the $k_{\mathrm{l}} < 0.8$ area changes to $(\triangle > 4.5, \eta < 0.65)$. Therefore this mapping also does not change significantly with k_{rad}. [J2], [79]

orthocyclic coefficient is used in both ac resistance and leakage inductance formula to modify the field distortion. In the leakage inductance formula, the inter-layer distance is also re-defined to represent the field energy in reality. A comparison of the compact normal and compact orthocyclic winding is also performed. The ac resistance of the compact orthocyclic winding decreases 20% at most, while the leakage inductance decreases 35% at most. All of the magnetic field models are verified through simulation and experimental results in three cases studies.

In conclusion, this chapter is with six major contributions:

- Propose an original equation for the ac resistance of the partial layer winding;
- Propose an approximation equation for ac resistance of the partial layer winding;
- Analyze the difference between the original and approximation equation analytically;
- Propose an orthocyclic coefficient for the ac resistance of the compact orthocyclic winding;
- Propose an orthocyclic coefficient and new definition of the inter-layer insulation distance for the leakage inductance of the compact orthocyclic winding;

- Give a generic comparison of the compact normal and compact orthocyclic winding in terms of the ac resistance and leakage inductance, which can be used to guide the winding design with precise parameters control requirements.

Chapter 4

Thermal Modeling: Thermal Coupling and Network

4.1 Background

With the electromagnetic model, the loss of magnetics is calculated. It is used as the heat source in the thermal model. In this chapter, the thermal modeling method of magnetics is investigated, while the planar transformer is chosen as the focus of the study due to its compact structure, vulnerable print circuit board (PCB) with weak cooling capacity, and high power densities. A thermal network modeling is proposed based on the assumption of thermal decoupling. The thermal impedance matrix is obtained, which is suitable to be implemented in the design flow. Based on the modeling method, the temperature distribution, as well as the hot-spot of the magnetics, are calculated, which can be further used for the thermal degradation analysis in the next chapter.

The basic structure of a planar transformer is in Fig. 4.1. A planar transformer is with benefits of high power density, low profile, and simple manufacturing process [123]. However, it also has the vulnerable print circuit boards (PCBs) surrounded by the core with poor heating dissipation capability. So the demand of thermal modeling for planar transformers is urgent, especially for calculating the hot-spot temperature, selecting the insulation grade, and achieving a high-reliable design.

There are several thermal modeling methods, i.e., the analytical method, the Computational Fluid Dynamics (CFD) simulation, the experimental measurements, and also applying hybrid methods.

The analytical model can be implemented in the design procedure [124, 125]. However, there is no general analytical model for planar transformers yet. Moreover, the knowledge of thermal engineering is required, while a case by case study is needed for each structure, core material, winding configuration, etc.

Recent advances in the computational hardware and thermal measurement devices enable faster and more accurate CFD simulations and experiments.

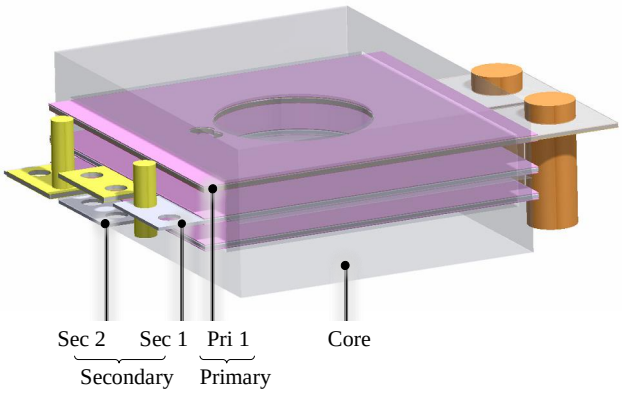

Fig. 4.1: A planar transformer structure. Pri 1 are the primary winding; Sec 1&2 are the two secondary windings. [C2], [122]

The CFD simulation can obtain a detailed temperature distribution of each structure [126–129]. The uneven thermal distribution inside the transformer is verified in [126] and [127]. For the transformer with compact internal structure or with insulation glue immersed, the whole transformer is regarded as a block, and its system-level thermal impedance is obtained through simulations [130].

The experimental methods determine the impacts of thermal conduction, convection, and radiation without theoretical simplifications [131, 132]. The impact of connectors, along with its interaction with other electrically-connected devices, is also considered. However, the experimental process is cost-, time- and material-consuming. Therefore, it is usually performed as the verification of the analytical and simulation model or in a final design. Exceptions in [133] and [134] use experimental results to fit the analytical model to adjust the coefficients. In this way, the accuracy of the experiment-modified analytical model is significantly improved.

This chapter introduces a thermal modeling method based on the publications in [C2], [122]. It is with the following features:

- Considering the thermal coupling between the ambient, windings, and core
  In high-density applications, the physical distance between windings and the core decreases, and the interaction between them should be considered. Moreover, when the transformer is exposed to the air, the thermal convection and radiation on the core surface are temperature-dependent and non-linear.
- A detailed thermal distribution as the output of the analysis
  It is used not only for the hot-spot identification and thermal design but also for the thermal reliability modeling, which is discussed in the next chapter.
- Time and computational resources-efficient
  The model should be able to be implemented in the optimization programs.

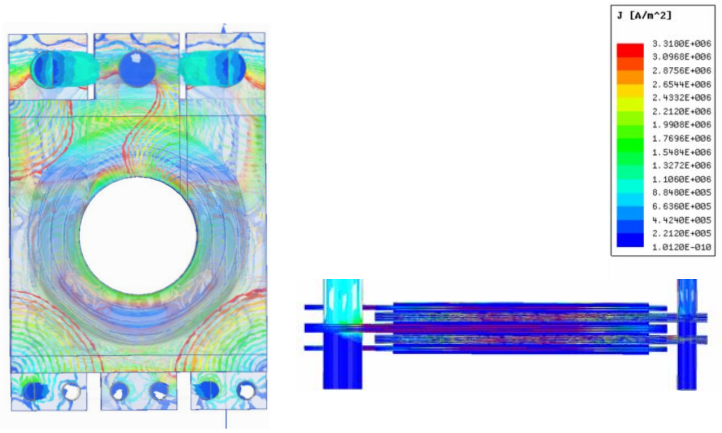

(a)

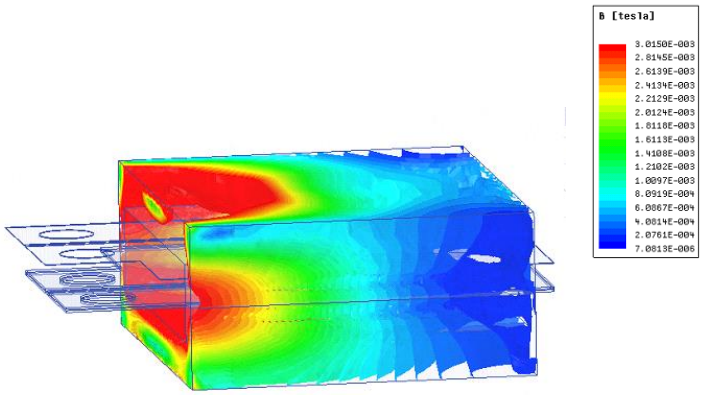

(b)

Fig. 4.2: Uneven current density (a) and flux density (b) distributions in simulation of the studied planar transformer. The planar transformer specification is introduced in Section 4.3. [C2], [122]

4.2 Thermal Modeling

4.2.1 Power Loss Modeling

Generally, there are two major power losses in magnetics, i.e., the winding and core losses. The analytical model of the winding loss is detailed discussed in the previous chapter. To obtain the detailed temperature distribution of each winding layer, the loss in each layer is calculated using Dowell's equation multiple times. For a planar transformer with complex winding configurations and layout, the finite element method simulation is an alternative method. The current density of the studied

planar transformer in the magnetic field simulation is illustrated in Fig. 4.2(a). Its specification is introduced in Section 4.3.

For the core loss, the classic model is proposed by Charles P. Steinmetz and named after him [67]. He observed the simple relationship between the flux density and the loss density through plenty of experimental results. Taking the frequency f into consideration, this Original Steinmetz Equation (OSE) is

$$P_s = K f^a {B_m}^b \tag{4.1}$$

where, K, a, b are material coefficients provided by core manufacturers through test results and curve fitting, and B_m is the peak magnetic flux density.

Although the OSE is simple and does not need too much expertise, it is limited to sinusoidal waveforms. For arbitrary waveforms, unlike winding losses, there is no orthogonality of core losses between each order harmonics, which is due to its nonlinearity [135]. Performing Fourier transformation of arbitrary waveforms to a series of sine waves, calculating the core loss in the different frequency domain, and finally making superposition of the core losses, are not proper methods for the arbitrary waveform core loss. To address this nonlinearity and extend the application of OSE, various methods are proposed, as summarized in [120]. Those equations include: the Generalized Steinmetz Equation (GSE) [69], Modified Steinmetz Equation (MSE) [68], the Improved Generalized Steinmetz Equation (iGSE) [70], the Equivalent Elliptical Loop (EEL) [72], the Natural Steinmetz Extension (NSE) [71], the Waveform-coefficient Steinmetz Equation (WcSE) [73], and Expanded GSE (EGSE) [74].

Among those, iGSE is widely accepted, because it is with a smaller estimation error and the same with OSE in sinusoidal-wave scenario [70]. It is written as

$$P_s = \frac{1}{T}\int_0^T k_i \left|\frac{\mathrm{d}B(t)}{\mathrm{d}t}\right|^{\alpha} (\Delta B)^{b-a} \mathrm{d}t \tag{4.2}$$

$$k_i = \frac{K}{(2\pi)^{a-1}\int_0^{2\pi} |\cos(\theta)|^a \cdot 2^{b-a} \mathrm{d}\theta} \tag{4.3}$$

where, θ is the phase angle, T is the period of flux waveform, and ΔB is the peak-to-perak flux amplitude.

Simulation results of the core flux density in Fig. 4.2(b) shows the uneven flux distribution inside the core. This distribution is structure-dependent, and it is only possible to be obtained through simulation.

In the following thermal modeling, the uneven current distribution in the same winding layer and uneven flux distribution in the core is neglected, and only the power loss differences among different layers are considered.

4.2.2 Thermal Network Modeling

In planar transformers and magnetics with pot cores, normally the core surrounds the winding, and blocks the thermal interaction between the windings and the ambient, as illustrated in Fig. 4.3. With this simplification, the thermal transferring initiated from the winding consists of two steps, i.e., from the winding to the core, and from the core to ambient. The thermal network modeling also follows this way, i.e., the network inside and outside the core, which is shown in Fig. 4.4. P_{core}, P_{w1},...

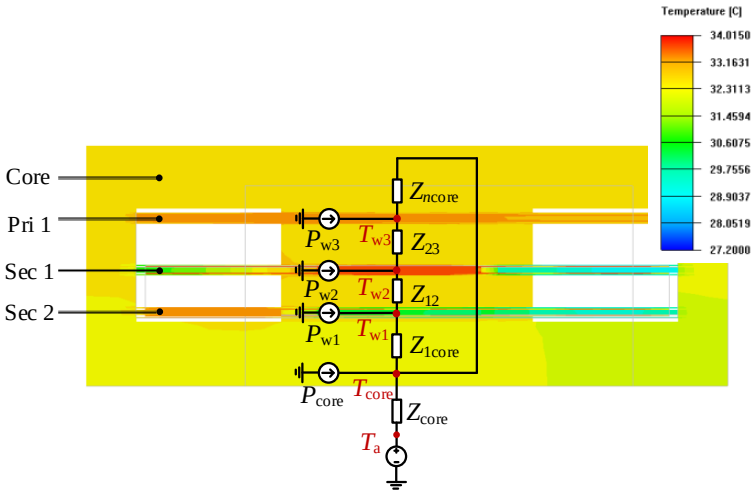

Fig. 4.3: A simplified illustration of the thermal impedance network of a planar transformer. The core is exposed to the air. The other mutual thermal impedances are not presented and the full model is in Fig. 4.4(a). [C2], [122]

are the losses generated by the core and windings, Z_{12}, Z_{13}, Z_{14},... are the mutual thermal impedance, T_{core}, T_{a}, T_{w1},... are the temperature of the core, ambient, and windings. The subscripts 1, 2, ... , n indicate the windings marked by those numbers. Fig. 4.4(a) neglects the core temperature difference, while Fig. 4.4(b) considers the temperature difference between the two pieces of cores. In the following, the first model is discussed, and the second can be applied in a similar way.

Fig. 4.4(a) is represented by the formula of the thermal matrix

$$\begin{bmatrix} T_{w1}(t) \\ T_{w2}(t) \\ \vdots \\ T_{wn}(t) \end{bmatrix} = T_{\text{a}} + \frac{d}{dt}\boldsymbol{Z_{\text{core}}(t)} * [P_{\text{core}} + \sum_{i=1}^{n} P_{wi}(t)] + \frac{d}{dt}\begin{bmatrix} Z_{11}(t) & Z_{12}(t) & \dots & Z_{1n}(t) & Z_{1core}(t) \\ Z_{21}(t) & Z_{22}(t) & & Z_{2n}(t) & Z_{2core}(t) \\ \vdots & \vdots & \ddots & \vdots & \\ Z_{n1}(t) & Z_{n2}(t) & \dots & Z_{nn}(t) & Z_{ncore}(t) \end{bmatrix} * \begin{bmatrix} P_{w1}(t) \\ P_{w2}(t) \\ \vdots \\ P_{wn}(t) \\ P_{core}(t) \end{bmatrix} \tag{4.4}$$

The impedance network is obtained with either multiple times of simulations or the analytical calculation, as introduced below. When replacing the thermal impedances Z_{12}, Z_{13}, Z_{14},... with thermal resistances R_{12}, R_{13}, R_{14},..., it becomes a resistance network, which means that only the steady state temperature is considered.

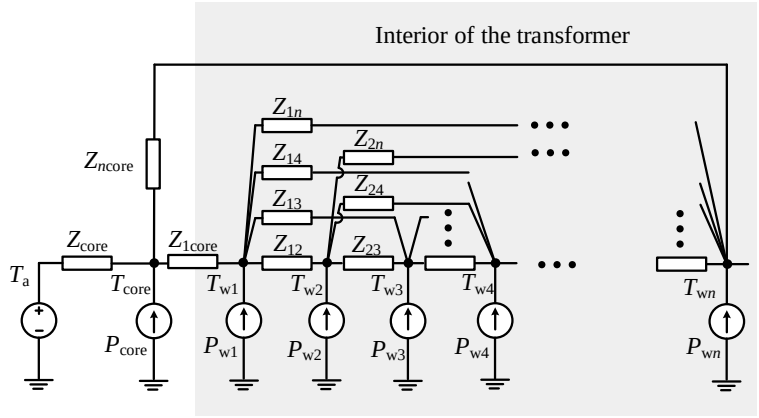

(a)

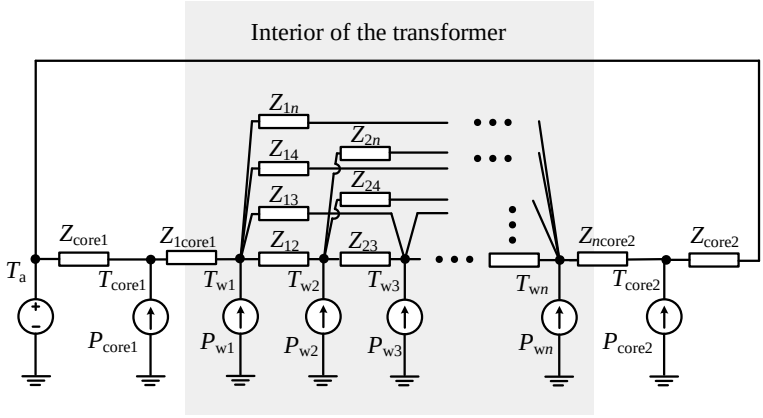

(b)

Fig. 4.4: The thermal network of the planar transformer. (a) The network considering single core temperature. (b) The network considering two core temperatures, each one for a half core piece. [C2], [122]

4.2.2.1 External Thermal Impedance

The external thermal impedances are those between the core and ambient air, which are located outside the gray area of Fig. 4.4. They can be obtained through the CFD simulation or analytical methods.

- CFD method

  There are thermal convection and radiation from the core to ambient. In the

CFD simulation, the thermal impedance $Z_{\text{core}}(t)$ is extracted by

$$Z_{\text{core}}(t) = \frac{T_{\text{core}}(t) - T_{\text{a}}}{P_{\text{core}}} \tag{4.5}$$

where P_{core} is the loss in the core, $T_{\text{core}}(t)$ is the core temperature. Applying different core losses P_{core} to the core, $Z_{\text{core}}(t)$ along with the time and power loss P_{core} are obtained in the simulation.

The thermal convection and radiation is temperature-dependent, so Z_{core}(t) is non-linear. It is also described by the first order Foster model [136]

$$Z_{\text{core}}(t) = R_{\text{core}}[1 - e^{-t/(R_{\text{core}}C_{\text{core}})}] \tag{4.6}$$

where, C_{core} and R_{core} are thermal capacitance and resistance, respectively. R_{core} is further modeled by [137]

$$R_{\text{core}} = a \times P^{b}{}_{\text{core}} \tag{4.7}$$

where a and b are thermal resistance coefficients based on curve fitting.

Using the Foster model (4.6) and (4.7) to fit the simulated $Z_{\text{core}}(t)$ obtains related parameters a, b, and C_{core}.

If only the steady-state temperature is needed, the impedance network is simplified to the resistance network. The thermal impedance is simplified to the thermal resistance

$$R_{\text{core}} = \frac{T_{\text{core}}(t \to \infty) - T_{\text{a}}}{P_{\text{core}}}. \tag{4.8}$$

where $t \to \infty$ indicates the time when the core temperature is stable. The related results of R_{core} is in Fig. 4.5 labeled as CFD.

Using (4.7) to fit the simulated R_{core} obtains a and b.

- Analytical method

  The analytical modeling in this study only considers the thermal resistance for simplification. If the core is exposed to air, the thermal convection and radiation take a major place. R_{core} is solved by [3]

$$R_{\text{core}} = \frac{R_{\text{conv}} R_{\text{rad}}}{R_{\text{conv}} + R_{\text{rad}}} \tag{4.9}$$

  where R_{conv} and R_{rad} are the convection and radiation resistance from the core to ambient, respectively.

  For the thermal convection resistance R_{conv}

$$R_{\text{conv}} = \frac{1}{h_{\text{conv}} A_{\text{conv}}} = \frac{1}{Nu \frac{\lambda}{L} \cdot A_{\text{conv}}} \tag{4.10}$$

  where, A_{conv} is the convection area, Nu is the Nusselt number, h_{conv} is the convection coefficient, L is the surface characteristic length of different surfaces, λ is the thermal conductivity, respectively.

  For the thermal radiation resistance R_{rad}

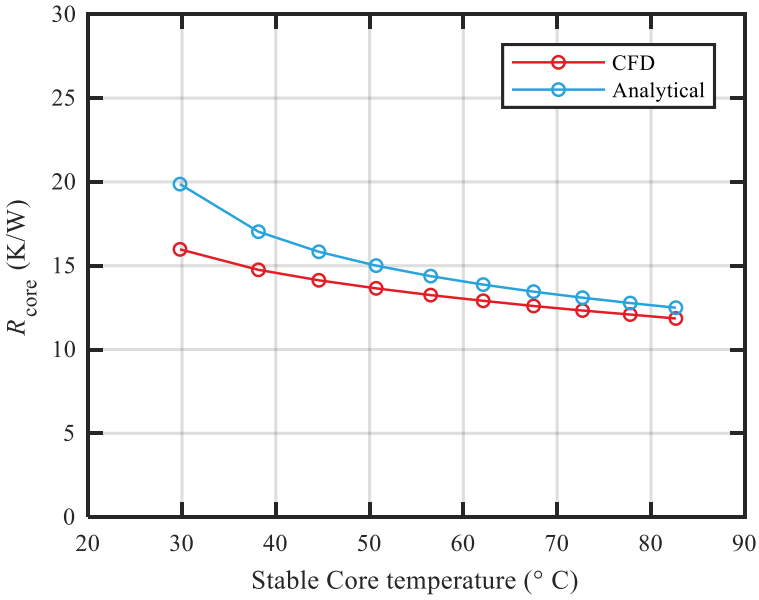

Fig. 4.5: The analytical and computational fluid dynamics (CFD) simulation results of the external thermal resistance R_{core}. The CFD results of the thermal resistance is obtained with (4.8) when the time $t = 6000$s. The analytical results are with (4.9). [C2], [122]

$$R_{\text{rad}} = \frac{1}{h_{\text{rad}} A_{\text{rad}}} = \frac{1}{\epsilon\sigma \frac{T_{\text{s}}^4 - T_{\text{a}}^4}{T_{\text{s}} - T_{\text{a}}} \cdot A_{\text{cov}}} \tag{4.11}$$

where, ϵ is the surface emissivity, A_{rad} is the radiation area, σ is the Stefan-Boltzmann constant, and h_{rad} is the radiation coefficient. The analytically calculated R_{core} is shown in Fig. 4.5 along with the CFD results.

4.2.2.2 Internal Thermal Impedance

The internal thermal impedance is the impedance between the core and windings, and between each winding, as shown within the gray area in Fig. 4.4. In planar transformers, the core surrounds the windings. The heat from the winding is firstly delivered to the core, and then dissipated to the ambient. The air is assumed as still and static inside the core. Therefore only thermal conduction is considered, and there is no thermal convection and radiation inside the core. With this assumption, the whole internal thermal impedance network is considered as a linear and time-invariant (LTI) system. Therefore, the law of superposition is applicable [138, 139].

This assumption also applies to the pot core magnetics. For other types of transformers and inductors, the accuracy may decrease with the increase of the contact area between the winding and air.

- CFD method

In the j-th simulation, applying the power P_j to the j-th node, and the mutual impedance $Z_{ij}(t)$ between node j and another node i can be extracted as

$$Z_{ij}(t) = \frac{T_i(t) - T_{core}(t)}{P_j} \tag{4.12}$$

where j = 1,2,... n, and the *core*, i = 1,2,... n. Performing n+1 times simulations obtains all the mutual impedances in (4.4).

Z_{ij}(t) is then fitted with the first order Foster model

$$Z_{ij}(t) = R_{ij}[1 - e^{-t/(R_{ij}C_{ij})}] \tag{4.13}$$

where, C_{ij} and R_{ij} are the fitted thermal capacitance and resistance obtained from the fitting, respectively.

Similarly, applying $t \to \infty$ obtains the internal thermal resistance with CFD simulations

$$R_{ij} = \frac{T_i(t \to \infty) - T_{core}(t \to \infty)}{P_j} \tag{4.14}$$

- Analytical method

  The thermal resistance R_{ij} can also be obtained with the analytical thermal conduction equations [3]

$$R_{ij} = \frac{1}{h_{cond} A_{cond}} = \frac{1}{\frac{\lambda}{l} \cdot A_{cond}} \tag{4.15}$$

where A_{cond} is the conduction area, h_{cond} is the conduction coefficient, l is the heat flux length.

4.2.3 Modeling Procedure

As a summary, the procedure for the thermal network modeling is

1. Extract the external thermal impedance Z_{core} or thermal resistance R_{core} with CFD simulations from (a) to (d) given below, or the external thermal resistance R_{core} with the analytical equation (4.9).
   (a) Import the geometry and material information of the magnetics to a CFD simulation tool;
   (b) Apply different P_{core} to the core, apply different T_a to the ambient, get enough simulations in the scale of study;
   (c) Extract Z_{core} of different (P_{core}, T_a) with (4.5), or extract R_{core} of different (P_{core}, T_a) with (4.8);
   (d) Curve fit Z_{core} in the (P_{core}, T_a) frame with (4.6), or curve fit R_{core} in the (P_{core}, T_a) frame with (4.7);
2. In CFD simulations, apply P_j to different winding layers, calculate the internal mutual impedance Z_{ij} with (4.12) and curve fit Z_{ij} with (4.13); or calculate the internal mutual resistance R_{ij} with (4.14). In the analytical calculation, the internal thermal resistance is given as (4.15).

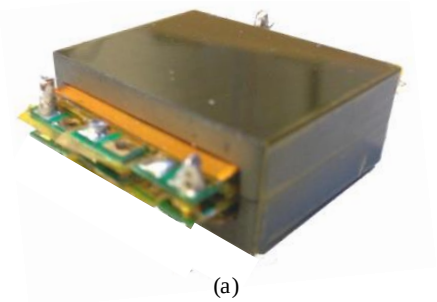

(a)

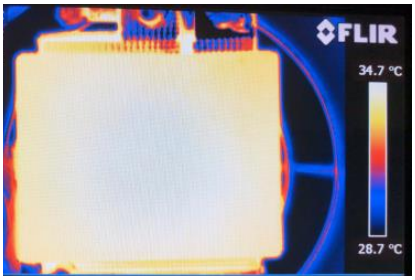

(b)

Fig. 4.6: The built transformer and its thermal image during operation. [C2], [122]

Table 4.1: Specifications of the planar transformer for Case Study 6 [C2], [122]

Parameters	Value	Units
Core material	Hitachi ML91S	
Core size	ER32	
Primary (Pri 1)	1	turn
Secondary(Sec 1+ Sec 2)	5 + 5	turn
PCB copper thickness	0.1	mm
FR4 thickness	70	um

With above procedures, the thermal impedances or resistance in the matrix are obtained. To use it, input the ambient temperature T_{a}, core loss P_{core}, and winding loss P_{wi} of interest, and use (4.4) to calculate the dynamic temperature response (thermal impedance network) or the steady-state temperature (thermal resistance network).

4.3 Case Study 6: A Planar Transformer

A planar transformer for a photovoltaic micro-inverter studied in [6] is used as a case study to verify the thermal model. The basic specifications of the transformer are listed in Table 4.1, and the transformer structure is illustrated in Fig. 4.1. Its

Table 4.2: Temperature of transformer components (°C) [C2], [122]

Methods	Ambient	Core	Pri 1	Sec 1	Sec 2
Proposed	26.4	33.1	33.8	34.2	33.6
CFD	26.4	31.9	32.8	33.0	32.6
Thermal camera	28.7	34.7			
Thermal couple	26.4	32.7		34.1	

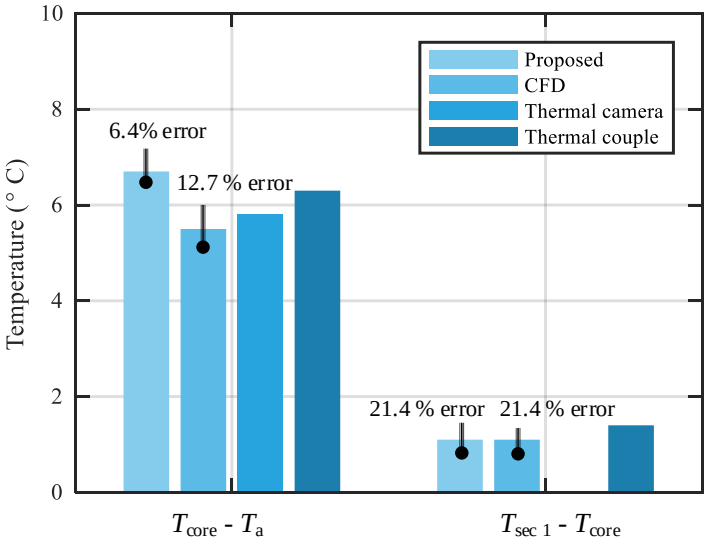

Fig. 4.7: The steady-state temperature comparison. T_{core}- T_a is the core and ambient temperature difference, and T_{Sec1}- T_{core} is the secondary and core temperature difference. The listed errors are those compared with the results from the Type K thermal couple. [C2], [122]

simulation results are in Fig. 4.2 and Fig. 4.3. In the test condition, a 0.75 MHz square waveform is applied to the primary side, and the planar transformer is with a resistance load. The total loss is 1.36 W. The ambient temperature is 28.7 °C. The measurement is with the thermal camera FLIR X8400sc and thermal couples RS Pro Type K, and the thermal image from the thermal camera is in Fig. 4.6.

With the proposed thermal model, the calculated steady-state temperature is shown in Fig. 4.7 and Table 4.2. Only the thermal resistance matrix is considered at the first step for the simplification.

Both the CFD simulations and the measurements obtain an uneven temperature distribution in the core and winding. The highest temperature is used and listed for comparison. It usually locates at the central point of the core. The thermal couple is also placed in the central part of the winding and the core. The errors of the proposed

method and the CFD are due to the assumptions that it is an LTI system, and also the cure fitting errors.

4.4 Conclusions

This chapter studies a thermal network modeling method of magnetics. It is applicable for planar transformers and pot core magnetics, where the core surrounds most of the winding surface. Its thermal impedance or the thermal resistance is obtained through the computational fluid dynamics (CFD) simulation or analytical equations. Finally, it is verified on a MHz planar transformer by two kinds of experimental measurement results.

The advances in this work include:

- A generic thermal modeling method is provided compared with the conventional analytical detailed and case-by-case modeling method;
- Through CFD simulations, it provides a matrix model and does not need to implement the simulation itself in the design procedure;
- The network nodes can be the winding layer, the whole winding, each piece of the core, and the entire core, etc. The number of network nodes is flexible, and it depends on the required level of accuracy.

The limitations of this method include:

- The thermal decoupling assumption becomes weak when the winding surface surrounded by the core decreases, and the accuracy decreases;
- The superposition law may become inapplicable when the inner air space increases, or with forced air cooling scenarios.

Chapter 5

Degradation Modeling: Testing, Analysis, and Lifetime Modeling

5.1 Background

This chapter uses one type of planar transformer for Accelerated Life Testing (ALT), and analyzes their degradation mechanism and lifetime model. The first observations in the ALT under the thermal stress is presented while the test setups, procedure, and results are introduced. Based on that, the most likely failure mechanisms of the planar transformer are investigated, and the thermal degradation and lifetime models are obtained with certain end-of-life criteria and assumptions.

A planar transformer structure is shown in Fig. 5.1(a). It consists of the magnetic core, the insulation layer/ insulator, and the printed circuit board (PCB) winding, respectively. The typical reliability stresses are shown in Fig. 5.1(b, c, d, e). The temperature is considered as the major reliability stress for magnetics, as proved in the research on the line-frequency power transformer and electrical machine. For planar magnetics, there is severe unevenly distributed current and magnetic flux, which affect the reliability of the PCB and core, respectively. Moreover, there are voltage shock and high-frequency components in power electronic circuits. Other stresses, i.e., humidity, solar radiation, electromagnetic radiation, and vibration, maybe also important depends on application scenarios.

From experiences in the power transformer and electric machine research, the insulation is the major concern of the reliability of magnetics. Generally, there are two kinds of structures which provide the insulation function in the transformer, i.e., the PCB board and the insulation tape/ insulator. The PCB board provides the board insulation for the copper traces. The solder mask covering the copper traces is made from the epoxy liquid, or dry-film photoimageable, or liquid photoimageable inks, etc. The board base material is normally with the grade of the Flame Retardant 4 (FR4)

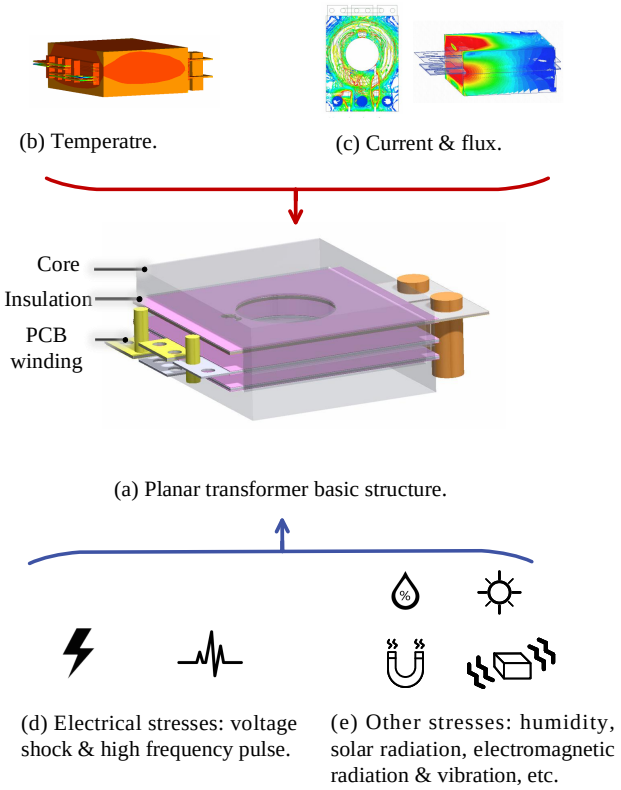

Fig. 5.1: Planar transformer basic structure (a) and typical reliability stresses (b, c d, e). [C3], [51]

for up to 140 °C applications. Compared with the wire winding, the PCB winding is with more complex structures. It is regarded as relatively vulnerable under thermal and vibration stresses. Its reliability under the thermal shock, vibration, and humidity stresses is reported in [35, 36]. The thermal shock causes thermo-mechanical failure due to the mismatch of the board material properties, including the copper layer, solder mask, FR4, etc. The failure caused by the flux residue in PCB is investigated in [37]. In [38], a lifetime model of PCB is presented based on the failure mechanism of the crack in the solder ball.

The second kind of insulation is the insulation tape/ insulator. It is between the boards to provide the inter-board insulation function. It is usually made with mica, Polyvinyl chloride (PVC), Vinyl, Polyimide, etc. The reliability of those materials has been investigated in other areas where those insulation materials are also used [32, 33]. Usually, the thermal and electrical stress are regarded as their principal failure stresses, and the Arrhenius model and inverse power law are applied for their lifetime modeling, respectively [34].

Compared with other parts in the planar transformer, the magnetic core is re-

garded as relatively reliable. Its reliability stresses include the overheating, internal and external force, and magnetic flux distortion [21]. It results in the variation of the core loss density and permeability, which affects the energy storage capability. There is the degradation study on the iron-powder core [23–25], iron-based amorphous core [22], ferrite [26–30], and core glue [31], respectively. The iron powder core is regarded with a severe thermal degradation feature. There are organic binders in the core, which lead to low resistivity and high eddy current above 125°C to 150°C. The increased eddy current induces core losses and further increases the core temperature, which finally leads to thermal run-away [24]. Their degradation curve follows a similar trend. In the beginning, the core loss is not significant; however, after a certain time, the slope of the loss curve increases with the time, which indicates the accelerated aging till failure [25]. The degradation of the iron-based amorphous results from its oxidation at the high-temperature [22]. There is a significant difference between the degradation curve below 150°C and at 200°C. In the former case, the core loss increases gradually. However, in the latter case, the loss firstly increases gradually and then more rapidly after 16 months. Therefore, temperature is the key factor that affects the formation of the oxide layer. The ferrite material is with low eddy current loss in tens to thousands of kHz range and therefore is widely used for planar magnetics. It is regarded as relatively stable compared with other types of cores, and there are few degradation results on its magnetic performance. Its thermal degradation mechanism is studied as early as 1967 for MgMnFeO ferrites in 1967 [26]. In telecommunication applications, the decrease of the permeability is also reported and characterized as the disaccommodation factor D_f [27]. Recent advances present the thermal aging results of the Cobalt-doped Mn–Zn ferrite [28], where the loss at 100kHz increases, however, above 500kHz decreases. There is a reversible increase of the core loss under the specific magnetic field applied at the test, however no significant changes are seen under different humidity environments. Its thermally-induced mechanical stress reliability is studied in [29, 30]. The core glue is applied to stick the cores, and its mechanical stress reliability is investigated in [31].

The Accelerated Life Testing (ALT) of planar magnetics is firstly reported in [51] to the best knowledge, and its degradation is analyzed in [76]. They are the major work of this chapter. In this study, a series of tests are performed for one type of planar transformers, various parameters are recorded as the degradation curve, and the failure mechanism and lifetime assessment procedure are also investigated.

5.2 ALT Setup

The planar magnetics under test are shown in Fig. 5.2, and they are the same type. They are soldered on the test fixture as the device under test (DUT) in Fig. 5.3(a). A total of 24 samples numbered 1 to 24 are used in the test. No. 1 to No. 12 are put in the 200 °C oven, while No. 13 to No. 24 are in the 180 °C oven, respectively.

5.2.1 Insulation Test

The insulation is the major focus of the reliability research in power transformers and electrical machines, where the partial discharge (PD) experiments are widely

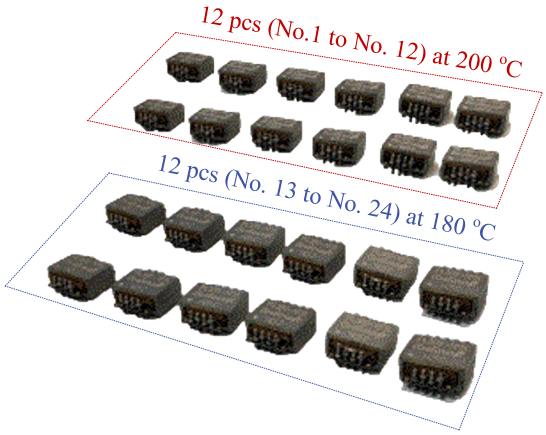

Fig. 5.2: Twenty-four planar transformers under test at two different thermal stresses. The transformers are with the dimension of 27×30×10 mm, 300 W rated power, ferrite core, and PCB windings, respectively. [C3, C4], [51, 76]

applied to characterize the insulation capability and degradation. This experience is also used in this study for planar magnetics. PD is the electrical discharge when the voltage is applied to the insulator, and it bridges the insulator between conductors partially [140].

The PD test in our study follows the IEC standard 60270 [141]. The test instruments and device under test (DUT) in a high voltage lab is shown in Fig. 5.3(a). A typical excitation voltage and PD charge pattern during the test are in Fig. 5.3(b). In the test, the excitation voltage is applied from zero and increases step by step. The partial discharge (PD) appears in the insulation, and the related PD level is measured by the PD measurement unit. During the test, the threshold of the PD event is set as 10 pC. Once the PD level exceeds the threshold, it is regarded as a PD inception event, and the corresponding excitation voltage is recorded as the inception voltage. The planar transformers under test are designed for several hundred kHz. However, the frequency of the excitation voltage in the test is 50 kHz due to the limitation of the hardware. The result of the inception voltage can still characterize the capability of the insulation, as the 50 Hz PD experiments for the medium-frequency transformer in the study [53].

5.2.2 Impedance Test Setup

The impedance of planar transformers at different degradation stages is tested with the impedance analyzer Keysight E4990A. Different measurement configurations are shown in Fig. 5.4. The impedance analyzer is set as a constant excitation voltage of 0.5 V.

The test fixture in Fig. 5.3(a) is also used here. To remove the impact of the board, its impedance Z_{board} and phase θ_{board} are also measured and excluded from

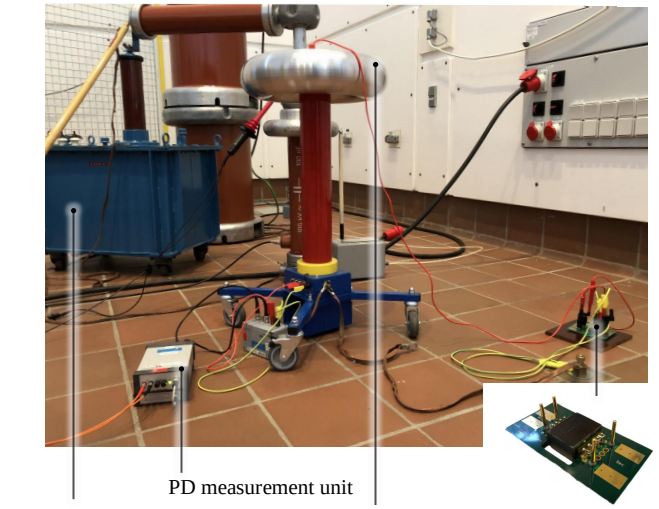

(a)

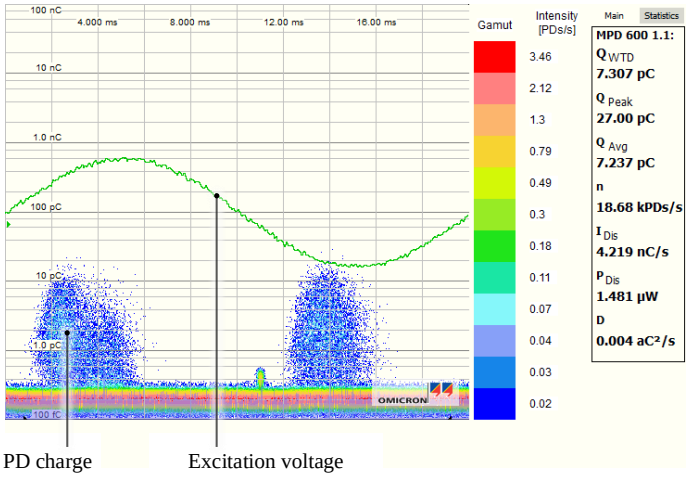

(b)

Fig. 5.3: Insulation test for planar transformers. (a) The PD test setup in a high voltage lab. (b) A typical PD test record pattern. [C3, C4], [51, 76]

the transformer impedance

$$\begin{aligned} Z_{ix} &= Z_{it}\cos(\theta_{it}) - Z_{\text{board}}\cos(\theta_{\text{board}}) \\ Z_{iy} &= Z_{it}\sin(\theta_{it}) - Z_{\text{board}}\sin(\theta_{\text{board}}) \end{aligned} \tag{5.1}$$

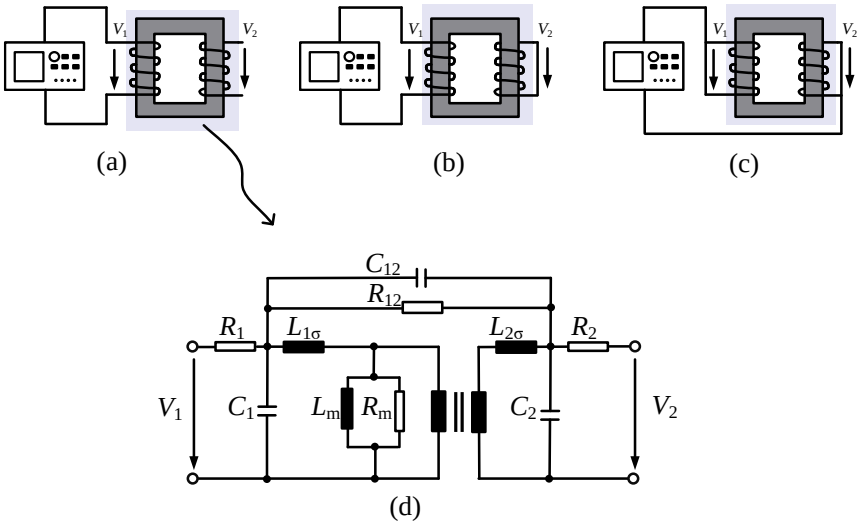

Fig. 5.4: Three measurement configurations of the planar transformer. Configuration (a) is for the primary inductance L_{m} + $L_{1\sigma}$ and primary resistance R_{m}+ R_1, configuration (b) is for leakage inductance $L_{1\sigma}$ + $L_{2\sigma}$ and short-circuit resistance R_1+ R_2, and configuration (c) is for the insulation capacitance C_{12} and insulation resistance R_{12}, respectively. [C3], [51]

$$Z_i = \sqrt{Z_{ix}^2 + Z_{iy}^2}, \quad \theta_i = \arctan \frac{Z_{ix}}{Z_{iy}} \tag{5.2}$$

where $Z_{i\mathrm{t}}$ and $\theta_{i\mathrm{t}}$ are the impedance and phase of the ith planar transformer with the test board, and Z_i and θ_i are the impedance and phase of the ith planar transformer without the test board, respectively.

With above test setups, the planar transformers are characterized by the parameters of the inception voltage, primary inductance, primary resistance, leakage inductance, and short-circuit resistance. They are used for the degradation analysis, as introduced below.

5.3 Degradation Analysis

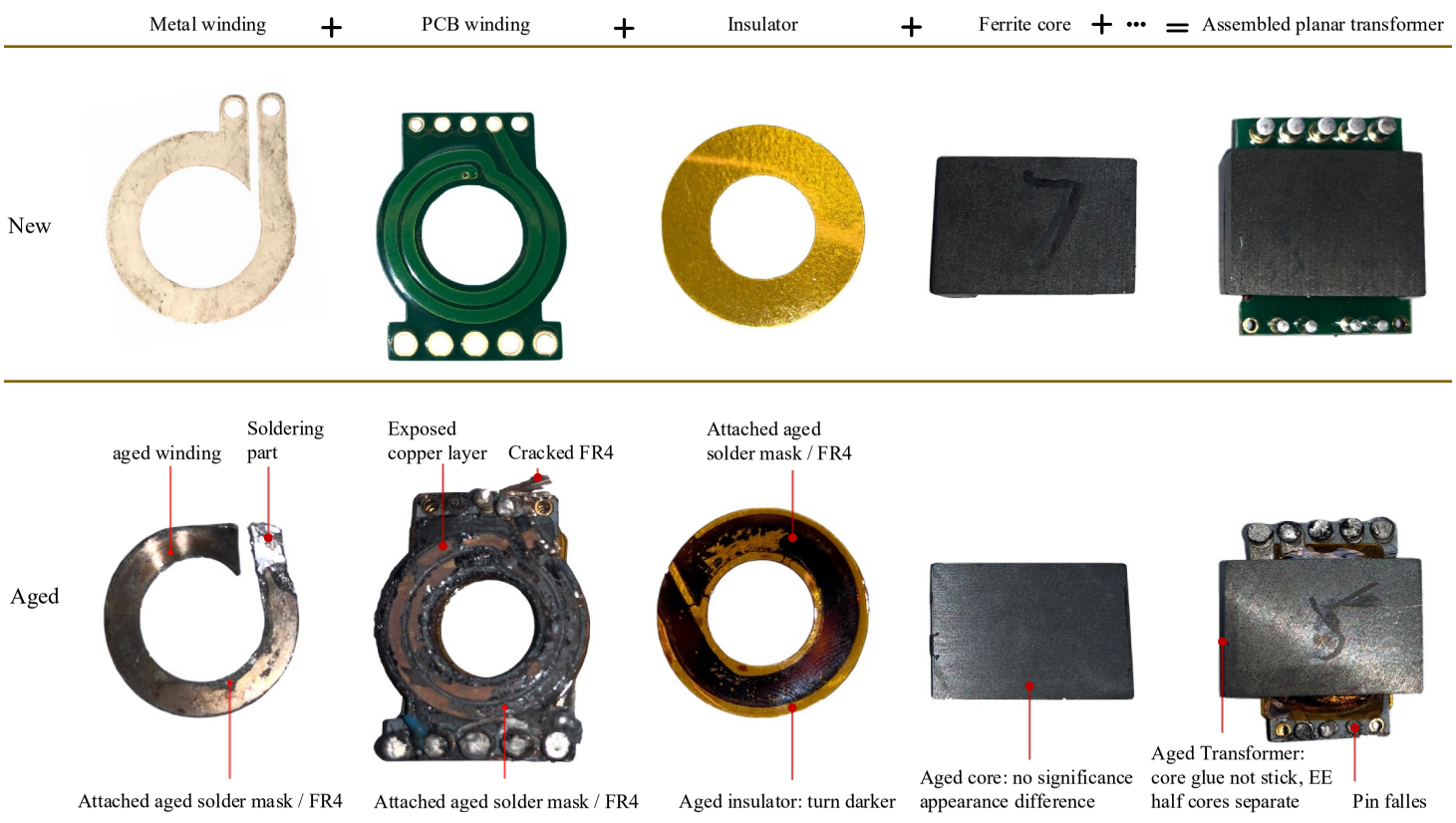

Fig. 5.5: Photo of the new and aged transformers and its sub-components. [C3], [51]

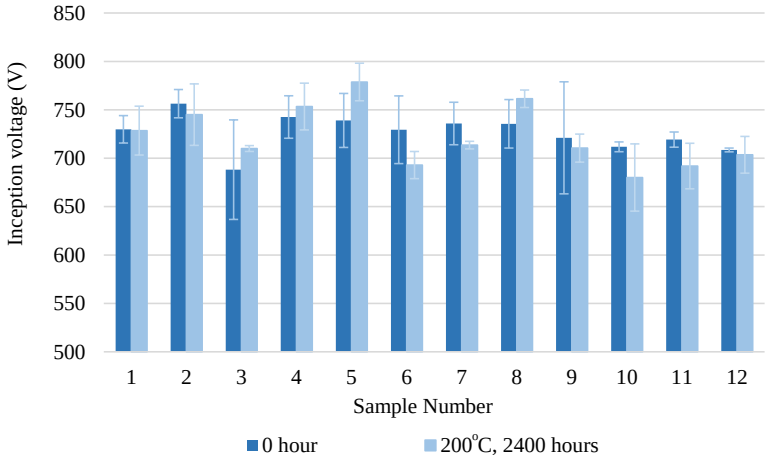

Fig. 5.6: The partial discharge test results of the planar transformer. For each bar, three times of tests are performed, and the mean inception voltage along with the standard deviation are given. [C4], [76]

The 24 transformers are firstly characterized by the testing setups before the degradation test. Then they are put into the high-temperature ovens for certain hours; after that, they are taken out of the oven and cooled down to the ambient temperature, and characterized in the testing again. This procedure is performed periodically. The related parameters are recorded along with their appearances, which are analyzed below.

5.3.1 Insulator Degradation

In the optical observation, the new and degraded transformer and their sub-components are shown in Fig. 5.5. The aged transformer is disassembled after 5688 hours of 200 °C thermal stress. There is a significantly difference between sub-components except for the cores. The insulator is with the Polyimide for above 130 °C applications. It turns darker during degradation, and its degradation mechanism is the thermo-oxidation [32].

The PD test results at the beginning and after 2400 hours 200 °C thermal stress are shown in Fig. 5.6. For the mean inception voltage, 8 out of 12 samples decreases while 4 samples increases. Their variations are also in the range of the standard deviation, which can attribute to the measurement errors. Therefore the conclusion that the inception voltage decreases with the degradation of the insulator can not be made at this stage.

In conclusion, at this stage, even there is a visible change of the PCB and the insulator, the insulation capability of planar transformers does not change significantly. The insulator can still provide the insulation function similar to the initial state.

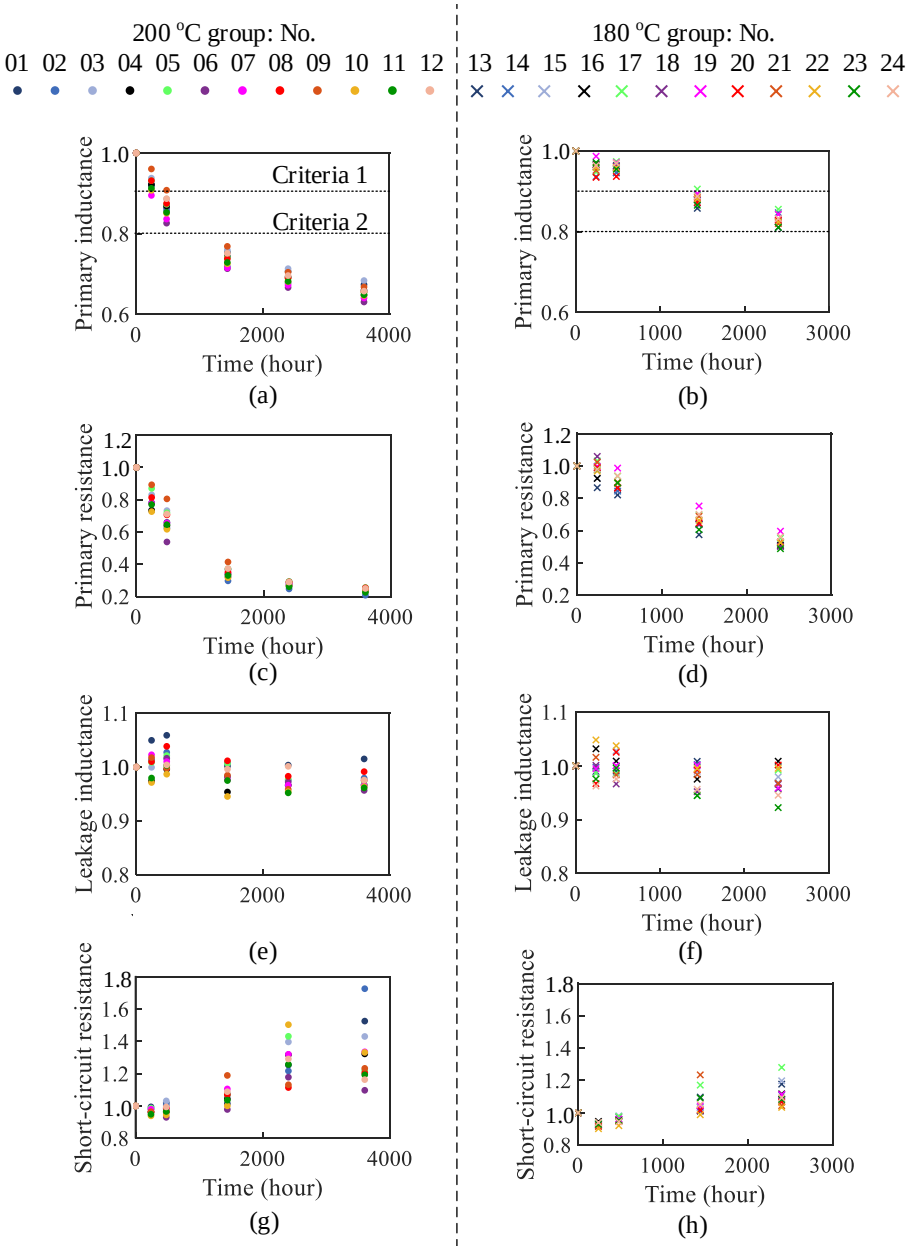

Fig. 5.7: Normalized parameters of planar transformers during ALT. All parameters are tested at 100 kHz. (a, c, e, g) are the primary inductance, primary resistance, leakage inductance, and short-circuit resistance of transformers with 200 °C thermal stress, and (b, d, f, h) are with 180 °C stress, respectively. The end-of-life criteria 1 is 10% inductance drop, while end-of-life criteria 2 is 20% inductance drop, respectively. [C4], [76]

5.3.2 Core Degradation

There is no significant change in the appearance of the new and aged cores in Fig. 5.5. So the core degradation is indicated by the primary impedance in Fig. 5.7(a, b, c, d). At both temperatures, the primary inductance $L_{\mathrm{m}} + L_{1\sigma}$ and resistance $R_{\mathrm{m}} + R_1$ decreases continuously and the slope of change also decreases. The primary inductance decreases approximately 30% and 15% after 2500 hours of thermal stress at 200°C and 180°C; and the primary resistance decreases about 70% and 40%, respectively.

The decrease of the primary inductance indicates a decrease of the equivalent permeability of the core. The mean normalized primary inductance at 200°C L_{m200} and at 180°C L_{m180} and their fitted curve along with the degradation time t is shown in Fig. 5.8

$$L_{\mathrm{m200}} = 0.6471 + 0.3547 \times \exp\left(-0.0009429t\right) \tag{5.3}$$

$$L_{\mathrm{m180}} = 0.6737 + 0.3211 \times \exp\left(-0.0003021t\right) \tag{5.4}$$

There are two possible explanations for the decrease of the equivalent permeability. The first is due to the degradation and volume explanation of the core glue. The core glue is a special chemical composition to stick the two pieces of cores together, as in Fig. 5.9. Usually, it is with the permeability close to the air. Therefore, the glue area is equivalent to a tiny air-gap in the magnetic field analysis. During the thermal degradation, its volume expands, and its color changes from the black to the white. So the equivalent air-gap length g increases gradually, which leads to a decrease of the primary inductance and resistance.

The second explanation is that the core loss density and permeability of the core material decrease during degradation, which leads to the decrease of the primary inductance and resistance at the same time. The ac resistance of the winding increases; however, the core loss decreases so much that the overall primary resistance decreases.

5.3.3 PCB Winding Degradation

In Fig. 5.5, the degraded PCB boards turn from green to black, become soft, and have cracks. In some places, the solder masks are resolved and evaporated, leaving the copper trace exposed to air, which can lead to the partial discharge, change of the stray capacitance, and internal short-circuit or open-circuit.

The test results related to the PCB board are shown in Fig. 5.7(e, f, g, h), including the leakage inductance $L_{1\sigma} + L_{2\sigma}$ and short-circuit resistance $R_{1\sigma} + R_{2\sigma}$. The leakage inductance of each transformer does almost not change during the test. The leakage inductance mainly depends on the transformer winding configuration, core dimension, and also the permeability of the insulation material. The air-gap in the transformer does not affect the leakage flux significantly. The structure of the transformer keeps the same, and the relative permeability of the insulation material is close to one during the degradation. Those factors result in a relatively stable leakage inductance during the whole test.

Finally, the short-circuit resistance increases 30% and 10% at 200°C and 180°C thermal stresses after 2500 hours testing, respectively. The leakage inductance in the short-circuit test does not change significantly. Therefore, the leakage field does not

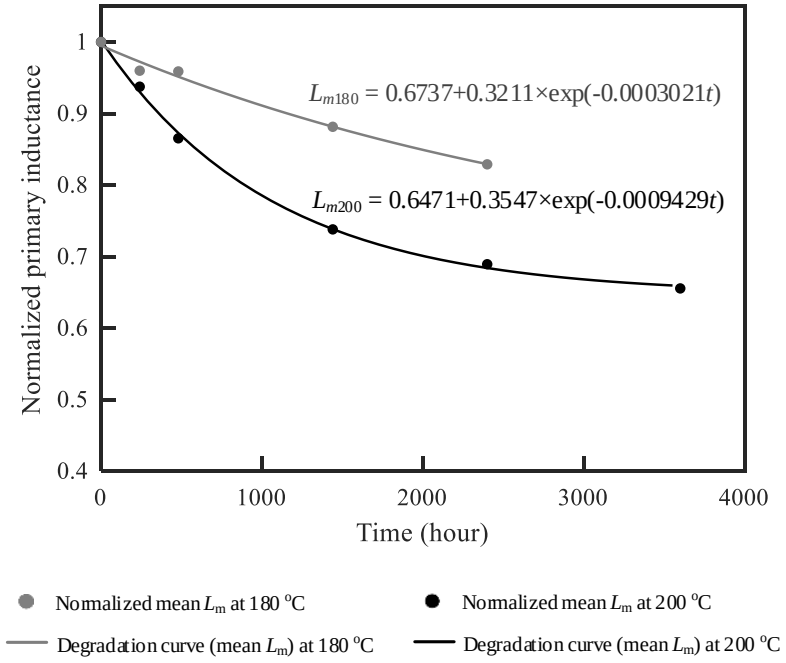

Fig. 5.8: Normalized mean primary inductance at 180 and 200 °C and their curve fitting results as the degradation curve. [C4], [76]

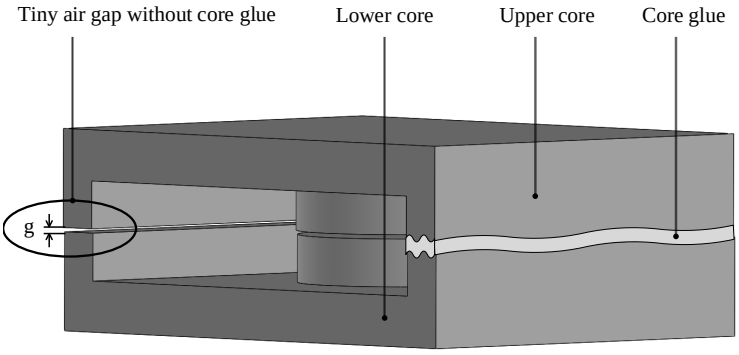

Fig. 5.9: The upper and lower cores of a planar transformer and the core glue to assemble them. Due to the core glue in between, the transformer is equivalent to have a tiny air-gap length g. In the left limb the core glue is not drawn to show the air gap. [C4], [76]

change too much even with the increase of the air-gap. The short-circuit resistance and leakage induce are induced by the same leakage field. So the increase of the short-circuit resistance is unlikely related to the increase of the air-gap. The most likely explanation is because of the oxidation of the copper trace in the PCB and the one-turn metal winding. The metal winding in Fig. 5.5 also becomes darker, which further verifies the explanation.

5.4 Lifetime Modeling

5.4.1 End-of-Life Criteria

The lifetime modeling procedure requires to determine the appropriate degradation indicator, end-of-life criteria, and lifetime models. Those are open questions, which highly depends on the degradation mechanism and application requirements.

For the degradation indicator, there are various candidates, which probably can affect the performance of magnetics and the operation of the circuit, including the winding resistance, core loss, stray capacitance, primary inductance, and leakage inductance, etc. For different application and design scenarios, there are various degradation indicators available. Usually, the impedance of magnetics is important to the circuit operation and current shape; the stray capacitance can result in high-frequency oscillation; and the resistive and core loss impacts the thermal performance and efficiency of magnetics.

The candidates for the end-of-life criteria include the absolute value, increase or decrease in percentage, and slope of change, respectively. Applying which type of criteria requires the understanding of failure mechanism and magnetic character. Usually, the core materials are with relative large variances between each other, even for the same type and batch. Therefore, there is a significant difference in the tolerances of the products from different suppliers, e.g., 3% to 40% tolerances on the permeability and loss density. The wiring and assembling process of magnetics can also introduce variances. For instance, when assembling two half cores, there are small air-gap g between them due to the core glue and the coarse core surfaces. Although the air-gap length g is small, its variance is with significant impact on the primary inductance value. Taking this into consideration, the type of absolute value criteria is not appropriate. Besides, the slope of change of most parameters in Fig. 5.7 is decreasing during degradation, which is different from the scenarios where this kind of criteria is applied. Normally the slope of change of parameter curves increases with the degradation, which is with physical meaning and indicates the accelerated aging during degradation. Therefore this type of criteria is also not suitable here. Finally, without specific application requirements, the degradation indicator and end-of-life criteria are chosen based on the assumptions in this study. The primary inductance is chosen as the indicator. Its decrease percentage α_{d} is chosen as the criteria. The assumed application criteria require a relatively stable primary inductance range to limit the current ripple and for enable the circuit operation. α_{d}=10% and 20% are chosen as the end-of-life criteria, respectively.

5.4.2 Lifetime Model

In 1889, Svante Arrhenius proposed a lifetime model for thermal degradation. It is based on the assumption that the temperature-dependent chemical reaction leads the wear-out of the device, and is widely adopted with the form of [34]

$$L = L_0 \times \exp[(\frac{E_a}{K_B})(\frac{1}{T+273} - \frac{1}{T_0+273})] \tag{5.5}$$

where K_B is the Boltzmann's constant and equals to $8.62 \times 10^{-5} eV/K$, E_a is the activation energy, T, T_0, L, and L_0 are the real and rated temperature and lifetime of the device, respectively. The formula itself gives an empirical relationship, while E_a is usually obtained from curve fitting of the field data.

The lifetime modeling steps of planar transformers are illustrated below:

- Degradation indicator and end-of-life criteria

  Based on the analysis and assumptions mentioned before, the primary inductance is chosen as the indicator, and 10% and 20% primary inductance drop are selected as the end-of-life criteria.

- End-of-life time

  Curve fit all primary inductance in Fig. 5.7(a, b) using equation $L_m = a_L + b_L \times \exp(-c_L \times t)$, where a_L, b_L, and c_L are coefficients. For each sample, find the time where the primary inductance drops α_d = 10% and 20% as the end-of-life time.

- Weibull probability plot

  Based on the end-of-life time of each sample, plot the Weibull paper. The α_d=10% case is exampled in Fig. 5.10.

- B1/B10 lifetime

  The B1/B10 lifetime means 1%/10% of the devices fail when devices reach the end-of-life time. On the Weibull paper, the B1/B10 lifetime is the interaction point between the 1%/10% unreliability line and the plotted probability line. As an example, the B10 lifetime points at 200°C and 180°C are shown in Fig. 5.10.

- Lifetime model

  Based on the B1/B10 lifetime obtained in Fig. 5.10, use the Arrhenius equation (5.5) to curve fit the lifetime model. The B10 lifetime results are illustrated in Fig. 5.11.

With the lifetime modeling procedure, the calculated B10 lifetime with the end-of-life criteria α_d = 10% is

$$L = 240 \times \exp[(\frac{1.1}{K_B})(\frac{1}{T+273} - \frac{1}{473})] \tag{5.6}$$

while with the criteria α_d = 20% is

$$L = 770 \times \exp[(\frac{1.1}{K_B})(\frac{1}{T+273} - \frac{1}{473})] \tag{5.7}$$

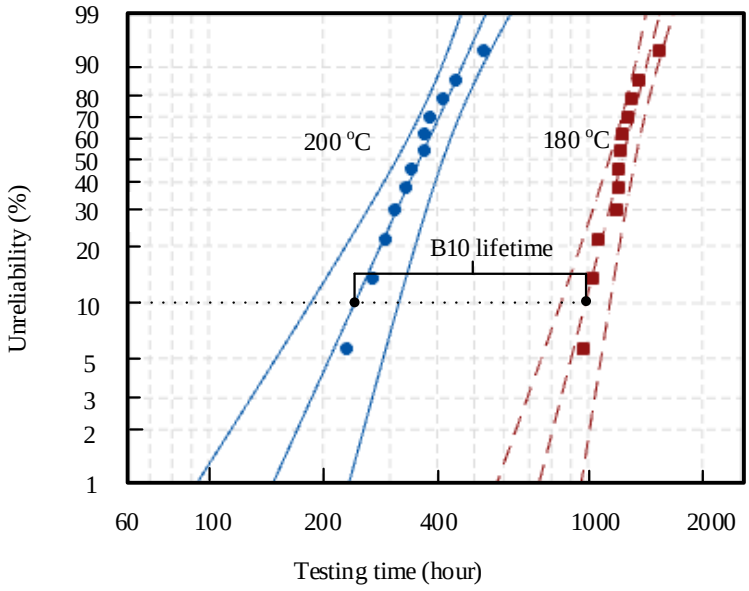

Fig. 5.10: The Weibull probability plot of tested transformers, with the end-of-life criteria α_d = 10%. The data is obtained from Fig. 5.7(a, b). The Weibull distribution and the two-sided confidence interval with 95% confidence level are also presented. From the plot, the B10 lifetime are 240 hours and 980 hours at 200°C and 180°C, respectively. [C4], [76]

where the temperature T and lifetime L are with the unit of Celsius and hours, respectively. For α_d = 10% criteria lifetime, the rated lifetime $L_0 = 240$ hours; for α_d = 20% criteria, $L_0 = 770$ hours. Both of them are with the rated temperature $T_0 = 200°C$.

With the calculated lifetime model, the lifetime of tested transformers in the temperature range of $180°C$ and $200°C$ is with validation, therefore it is with a solid line in Fig. 5.11. Out of this range is with the dotted line, and the calculated lifetime is of a reference value.

At 140°C which is the maximum tolerance temperature of most FR4 PCB, the calculated lifetime of tested transformers is 10,800 hours (1.2 years) with 10% primary inductance drop criteria, while it increases to 34,800 hours (4.0 years) with 20% criteria. So the lifetime model is also heavily impacted by the selected end-of-life criteria.

In general, the determination of appropriate degradation indicator, end-of-life criteria, and lifetime model is essential in the lifetime modeling procedure, and the variance of those factors causes significant differences in final results. A proper lifetime modeling requires the understanding of the failure mechanism and field requirements, e.g., functionality, efficiency, and parameter control, etc.

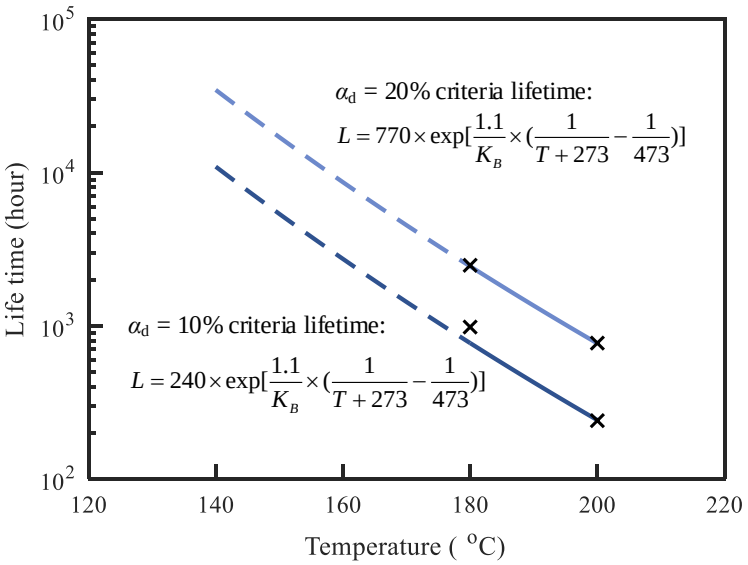

Fig. 5.11: B10 lifetime of tested transformers with 50% confidence level, α_d = 10% and 20% end-of-life criteria. E_a = 1.1eV is the same for two lifetime models and is obtained from the curve fitting of Arrhenius equation. $K_B = 8.62 \times 10^{-5} eV/K$ is the Boltzmann's constant. [C4], [76]

5.5 Conclusions

This chapter studies the Accelerated Lifetime Testing (ALT) and degradation analysis of planar transformers. Various parameters, e.g., the inception voltage, primary inductance, primary resistance, leakage inductance, and short-circuit resistance, are measured in the partial discharge and impedance tests. Based on the up-to-date data and optical comparison, the likely degradation mechanisms of the insulation, core, and PCB winding are studied. With assumed end-of-life criteria of the inductance drop percentage, the lifetime modeling procedure of planar magnetics is proposed, and the lifetimes of the tested transformer under different temperatures are obtained. In general, this chapter is with four major contributions:

- Introduce the reliability test setups for the planar transformer and its corresponding testing parameters;
- Report the up-to-date reliability degradation tests results;
- Analyze the degradation mechanism;
- Based on the assumed degradation indicator and end-of-life criteria, propose a lifetime modeling procedure for planar magnetics.

Chapter 6

Conclusions: Summary and Outlook

6.1 Summary and Main Contributions

Current and future industry demands of high-density, high-frequency, and high-efficiency power electronics require precise models of magnetic components, especially in emerging applications, e.g., automotive, more electric aircraft, and renewable energy. Moreover, there is more and more pressure for cost reduction, which limits the design margin and reduces the reliability of magnetics. Therefore a re-visit of the magnetic components modeling and exploration of the reliability are necessary and have been done in this thesis.

This thesis studies the electric field, magnetic field, thermal modeling, and the reliability of magnetics. Parasitic parameters of transformers, inductors, and special winding configurations are extracted. The thermal network of planar magnetics is modeled. Long-term Accelerated Lifetime Testing (ALT) is performed for the degradation analysis of a series of planar transformers. The main contributions of this project are:

- M1: An improved stray capacitance model for inductors

  A closed-form equation for the stray capacitance of inductors is proposed. It considers the core/shield-related capacitance, i.e., the central limb, side limb, and yoke capacitance, and also the core/shield grounded and floating case. The model is verified by the electrical field simulations and experiments. Moreover, the criteria to determine the core/shield-related capacitance is presented. As a rule of thumb, the stray capacitance modeling of inductors should consider the core/shield-related capacitance when the inductor is with one layer, or with a shield, or with the ETD and P shape cores where the winding exceeds 50% of the core window width.
- M2: Parasitic parameters models of orthocyclic windings

The orthocyclic winding and its impact on the winding parasitics, i.e., the ac resistance, leakage inductance, and winding capacitance, are investigated. Although the normal winding placement is usually considered in the design phase, the orthocyclic winding is more common when wiring round wire winding in reality. To consider its affect on the analytical modeling, the compensation equations are used for calculating the stray capacitance formula, and the orthocyclic coefficient and the re-defined inter-layer distance are used to modify the ac resistance and leakage inductance formula. Moreover, the proposed modifications are verified by FEM simulations and experiments. Finally, the maximum variation range of the compact orthocyclic winding compared with the compact normal winding is also studied, the stray capacitance increases 118% or decreases 20% at most; the ac resistance decreases up to 20%; and the leakage inductance decreases 35% at most.

- M3: Power loss model of partial layer windings

  The ac resistance model of the partial layer winding is presented. An original equation and an approximation model are derived. Those equations are verified by simulation and experiments and are used for winding loss optimization to control the winding turns precisely.

- M4: Thermal model of planar transformers

  A thermal impedance network model of planar transformers is proposed. With certain numbers of Computational Fluid Dynamics (CFD) simulation or analytical calculations, a thermal matrix model is obtained using this method. Through this, the temperature distribution of the transformer is obtained and verified in a MHz planar transformer.

- M5: Long-term Accelerated Lifetime Testing (ALT) of planar transformers

  The degradation testing of planar transformers with thermal stress is performed in this project. It is the first ALT of planar transformers to the best knowledge. Twenty-four pieces of one type planar transformers are used as specimens. Transformer parasitics, e.g., primary impedance and resistance, leakage inductance, and short-circuit resistance, are tested and recorded during the degradation stage. The inception voltage is also measured in the partial discharge test to evaluate the insulation.

- M6: Degradation analysis and Lifetime modeling of planar transformers

  Based on the degradation testing results, the likely degradation mechanisms of one kind of planar transformers are analyzed. The drop of the primary inductance and resistance is likely due to the degradation of the core glue or core material; the increase of the short-circuit resistance results from the copper layer oxidation; there is no significant change of the leakage inductance and inception voltage. Moreover, the primary inductance is chosen as the degradation indicator, and the primary inductance drop percentage is chosen as the end-of-life criteria. Finally, the lifetimes of the planar transformer at different temperatures are calculated based on the Arrhenius model.

The main contribution M1, M2, and M3 are the modeling study in the electromagnetic field, which answers the study question Q1 and realizes the objective O1

as listed in Chapter 1 Introduction. M4 is the thermal modeling work raised by the study question Q2 and objective O2. In the reliability modeling part, M5 performs the long-term ALT for Q3 and O3, while M6 is the degradation analysis for Q4 and O4.

In general, the magnetic component modeling work in this thesis answers several study questions which are urgently demanded by the emerging and future power electronics. Most proposed models in the electric field, magnetic field, and thermal modeling are generic, while the degradation analysis and lifetime modeling of the studied planar transformers are also of significant reference value to other kinds of planar transformers and even wiring magnetics.

6.2 Research Outlook

This Ph.D. project has investigated the modeling of power electronics magnetic components in different aspects, and also identified research opportunities and challenges for the future study:

- R1: Stray capacitance network of planar transformers

  Planar magnetics are widely applied in hundreds of kHz to MHz range, where the stray capacitance modeling is essential. There have been studies to design the PCB layout for a smaller stray capacitance, and to decrease the impact of the stray capacitance to the circuit. However, a systematic modeling of the stray capacitance network considering the layout and core is still missing, which is crucial to the capacitance calculation and model-based design.

- R2: Degradation and failure mechanisms

  The likely degradation mechanisms of planar magnetics are investigated in this project. However, the final confirmation is needed. Current degradation analysis is based on the electrical parameters, e.g., impedance and phase of magnetics. Further study can perform the sample compound tests, e.g., *x*-ray diffraction and secondary ion mass analysis. Besides, more types of magnetic components with the different core materials, core shapes, core glue, insulation, wires, etc., are under analysis for a global picture of the problem. Finally, degradation and failure caused by other stressors, e.g., humidity, voltage, high-frequency pulse, are also worth investigation.

- R3: Magnetic components testing in power-electronic-system-level

  Current ALT focuses only on thermal degradation where the electric stressors are not applied. In reality, magnetic components are under the high-frequency current and voltage excitation in power electronic circuits, under which environments the ideal single reliability stressors can not emulate. Therefore, system-level degradation tests are of significant importance, especially according to different application scenarios.

- R4: Lifetime modeling and prediction

  The lifetime model obtained in our work is based on an assumed failure indicator and end-of-life criteria. To be applicable for field applications, a proper

choice of the indicator and criteria based on application requirements and failure mechanisms are needed. Moreover, lifetime models other than the Arrhenius equations may be necessary for different degradation mechanisms. Finally, for the lifetime prediction under the long-term mission profile, there are three major steps: the electro-thermal loading analysis, damage accumulation, and variation analysis. The reliability-related models and coefficients in those procedures require further investigation.

- R5: Reliability-oriented design and optimization

  With the lifetime model and prediction procedure, the reliability-oriented design and optimization of power electronic magnetics can be performed in the future. The existing design philosophy follows the electric-magnetic-thermal design procedure and includes feedback among them. It uses design restrictions such as the efficiency, cost, temperature rise, insulation voltage stress, impedance range, etc. However, restrictions like temperature rise and voltage stress are based on the lifetime estimation under constant loading conditions. Therefore, the empirical coefficients are necessary to provide sufficient margins in the design. It is not economical when overestimated or easy-to-fail when underestimated. Taking the reliability perspective into consideration, the design procedure of electro-magnetic-thermal-reliability can be proposed. With the required lifetime as one of the design target, those temperature rise and voltage stress design margins can be minimized confidently to reduce the cost while fulfilling the reliability and performance requirements.

Appendix A

Appendix

This appendix presents the detailed derivation process of the electro-magnetic modeling in this report. Appendix A.1 and A.2 are for the stray capacitance model in Chapter 2. Appendix A.1 derives core-related coefficients for the core-related capacitance. The analytical derivation of the core and shield potential in an inductor is given in Appendix A.2. The derivation procedure of the winding power loss in the partial layer for Chapter 3 is in Appendix A.3, it is originally for the rectangle wire, and is extended to the foil, square shape wire, and round wire with the equivalent thickness transformation.

A.1 Core-related Coefficients

The inherent capacitance C_x with (2.2) is with uniform voltage distribution in each electrode. If the voltage distributes linearly along the electrodes, the stored energy of the system is [56]

$$W = \frac{C_x}{6}(U_{D1}^2 + U_{D1}U_{D2} + U_{D2}^2) \tag{A.1}$$

where U_{D1} and U_{D2} are the voltages between the two ends of electrodes, respectively. The voltage between the winding and the core is assumed linear as Fig. 2.4(a). With eq. (A.1), the energy stored in A1, A2, A3 of Fig. 2.1(b, c) are W_1, W_1, and W_3

$$W_1 = C_{\mathrm{cw1}}\frac{U_{\mathrm{d}}^2 + U_{\mathrm{d}}(U_{\mathrm{d}} + U_{\mathrm{t}}) + (U_{\mathrm{d}} + U_{\mathrm{t}})^2}{6} \tag{A.2}$$

$$W_2 = C_{\mathrm{cw2}}\frac{[U_{\mathrm{d}} + (p-1)U_{\mathrm{t}}]^2 + (U_{\mathrm{d}} + pU_{\mathrm{t}})^2 + [U_{\mathrm{d}} + (p-1)U_{\mathrm{t}}](U_{\mathrm{d}} + pU_{\mathrm{t}})}{6} \tag{A.3}$$

$$W_3 = C_{\mathrm{cw3}}\frac{U_{\mathrm{d}}^2 + U_{\mathrm{d}}[U_{\mathrm{d}} + (p-1)U_{\mathrm{t}}] + [U_{\mathrm{d}} + (p-1)U_{\mathrm{t}}]^2 + (U_{\mathrm{d}} + U_{\mathrm{t}})^2 + (U_{\mathrm{d}} + pU_{\mathrm{t}})^2 + (U_{\mathrm{d}} + U_{\mathrm{t}})(U_{\mathrm{d}} + pU_{\mathrm{t}})}{6} \tag{A.4}$$

or

$$W_3 = C_{cw3}\frac{U_d^2 + U_d(U_d + pU_t) + (U_d + pU_t)^2 + (U_d + U_t)^2 + [U_d + (p-1)U_t]^2 + (U_d + U_t)[U_d + (p-1)U_t]}{6} \tag{A.5}$$

(A.5) is for the gray letter case in Fig. 2.4(a) with different winding terminal direction.

The total stored energy is also expressed by the core-related capacitance C_{cwT}

$$W_{cwT} = \frac{C_{cwT}}{2}(pU_t)^2 \tag{A.6}$$

Equaling $W_{cw} = W_1 + W_2 + W_3$ obtains the potential coefficients k_{cwi}, as given in (2.10).

A.2 Potential of the Core/Shield

To derive the core/shield potential, the problem is mapped from the electric field to the electric circuit, which is explained in Fig. 2.5(a). The first turn voltage is defined as U_1, and the voltage of the last turn in the first layer is U_T. The voltage of each turn in the first layer is

$$U_y = U_1 + (U_T - U_1)\frac{y}{h_w} \tag{B.1}$$

where, h_w is the whole winding height, y is the length from the considered turn to the first turn. The unit-length central-limb capacitance along y is

$$C_y = \alpha_{cw1} \cdot \varepsilon_0 \varepsilon_{cw1}\frac{2\pi r_{cw1}\mathrm{d}y}{d_{cw1}} \tag{B.2}$$

The current from the first layer to core central limb is

$$i_1 = \int_0^{h_w}(U_y - U_c)C_y = \frac{U_1 + U_T - 2U_c}{2}C_{cw1} \tag{B.3}$$

With a similar procedure, i_2, i_{31}, and i_{32} are derived as

$$\begin{aligned} i_2 &= \frac{U_1 + pU_t + U_1 + (p-1)U_t - 2U_c}{2}C_{cw2} \\ i_{31} &= \frac{U_1 + U_1 + (p-1)U_t - 2U_c}{2}C_{cw3} \\ i_{32} &= \frac{U_T + U_1 + pU_t - 2U_c}{2}C_{cw3} \end{aligned} \tag{B.4}$$

Using Kirchhoff's Current Law (KCL):

$$i_1 + i_2 + i_{31} + i_{32} = 0 \tag{B.5}$$

the core potential U_c is derived as

$$U_c = U_1 + \frac{C_{cw1} + (2p-1)C_{cw2} + 2pC_{cw3}}{2C_{cw1} + 2C_{cw2} + 4C_{cw3}} U_t \tag{B.6}$$

The coefficient k_U is calculated by

$$k_U = \frac{U_d}{U_t} = \frac{U_1 - U_c}{U_t} = -\frac{C_{cw1} + (2p-1)C_{cw2} + 2pC_{cw3}}{2C_{cw1} + 2C_{cw2} + 4C_{cw3}} \tag{B.7}$$

For the gray voltage distribution case in Fig. 2.4(a), i_{31} and i_{32} in the equations exchange accordingly, and the final result is the same.

A.3 Partial Layer Winding Losses

Simplifying Maxwell equations with the one-dimensional field assumptions in Section 3.2.1 obtains

$$\frac{\mathrm{d}^2 H_z}{\mathrm{d}\, y^2} = j\sigma\omega\mu H_z = \gamma^2 H_z \tag{C.8}$$

with:

$$\gamma = \frac{1+j}{\delta} \tag{C.9}$$

where H_z is the magnetic field intensity, μ and δ are the permeability and skin depth, respectively.

With the internal skin effect magnetic field intensity H'_{int1} and H'_{int2} derived in (3.12) as the boundary condition, solving (C.8) obtains the skin effect magnetic field intensity H'_{sz}

$$H'_{sz} = \frac{kF_m \sinh \gamma y}{2h_c \sinh \frac{\gamma d_w}{2}} \tag{C.10}$$

H'_{sz} induces the current density J'_{sx}

$$J'_{sx} = \frac{\mathrm{d}\, H'_{sz}}{\mathrm{d}\, y} = \frac{\gamma k F_m \cosh \gamma y}{2h_c \sinh \frac{\gamma d_w}{2}} \tag{C.11}$$

J'_{sx} induces the skin effect losses in the partial layer

$$P'_s = t_0 \frac{l_{MLT} \frac{h'_w}{t_0}}{2\sigma} \int_0^{d_w} \left|J'_{sx}\right|^2 \mathrm{d}\, y = \frac{kF_m^2}{4h_c\sigma\delta}\nu \tag{C.12}$$

where

$$\nu = \frac{\sinh\triangle + \sin\triangle}{\cosh\triangle - \cos\triangle} \tag{C.13}$$

l_{MLT} is the Mean Length Turn (MLT).

With the average external proximity field intensity H'_{ext1} and H'_{ext2} derived in (3.13) as the boundary condition, solving Eq. (C.8) again obtains the proximity effect magnetic field intensity H'_{pz}

$$H'_{\mathrm{pz}} = \frac{\cosh\gamma y}{\cosh\frac{\gamma d_{\mathrm{w}}}{2}} H'_{\mathrm{ext1}} \tag{C.14}$$

H'_{pz} induces the proximity current density $J'_{\mathrm{p}x}$

$$J'_{\mathrm{p}x} = \frac{\mathrm{d}\, H'_{\mathrm{pz}}}{\mathrm{d}\, y} = \frac{\gamma \sinh\gamma y}{\cosh\frac{\gamma d_{\mathrm{w}}}{2}} H'_{\mathrm{ext1}} \tag{C.15}$$

and the proximity effect losses of the partial layer

$$P'_{\mathrm{P}} = t_0 \frac{l_{\mathrm{MLT}}\frac{h'_{\mathrm{w}}}{t_0}}{2\sigma} \int_0^{d_{\mathrm{w}}} \left|J'_{\mathrm{p}x}\right|^2 \mathrm{d}\, y = \frac{k l_{\mathrm{MLT}} F_{\mathrm{m}}^2 (2p+k)^2}{4 h_{\mathrm{c}} \sigma \delta} \xi \tag{C.16}$$

where

$$\xi = \frac{\sinh\triangle - \sin\triangle}{\cosh\triangle + \cos\triangle} \tag{C.17}$$

Adding the loss of the p full layers P_{p} and partial layer P'_{s} and P'_{p} obtains the total loss P_{ori}

$$P_{\mathrm{ori}} = P_{\mathrm{p}} + P'_{\mathrm{s}} + P'_{\mathrm{p}} = \frac{l_{\mathrm{MLT}} F_{\mathrm{m}}^2}{h_{\mathrm{c}} \sigma \delta} \left(\frac{p}{4}\nu + \frac{4p^3 - p}{12}\xi + \frac{k}{4}\nu + \frac{k(2p+k)^2}{4}\xi\right) \tag{C.18}$$

Using the mathematical identities

$$\frac{\nu + \xi}{2} = \frac{\sinh(2\triangle) + \sin(2\triangle)}{\cosh(2\triangle) - \cos(2\triangle)} = \varsigma \tag{C.19}$$

Eq. (C.18) is transferred to

$$P_{\mathrm{ori}} = \frac{l_{\mathrm{MLT}} F_{\mathrm{m}}^2}{h_{\mathrm{c}} \sigma \delta} \frac{(p+k)}{2} \varsigma + \frac{l_{\mathrm{MLT}} F_{\mathrm{m}}^2}{h_{\mathrm{c}} \sigma \delta} \frac{4p^3 - 4p - 3k + 3k(2p+k)^2}{12} \xi \tag{C.20}$$

and the ac resistance of the original partial layer equation is

$$R_{\mathrm{ori}} = \frac{p+k}{h_{\mathrm{w0}} \sigma \delta} l_{\mathrm{MLT}} t \varsigma + \frac{4p^3 - 4p - 3k + 3k(2p+k)^2}{6 h_{\mathrm{w0}} \sigma \delta} l_{\mathrm{MLT}} t \xi \tag{C.21}$$

The dc resistance is

$$R_{\mathrm{dc}} = \frac{(pt + t')l_{\mathrm{MLT}}}{h_{\mathrm{w0}}\sigma d_{\mathrm{w}}} = \frac{t(p+k)l_{\mathrm{MLT}}}{h_{\mathrm{w0}}\sigma d_{\mathrm{w}}} \tag{C.22}$$

So the ac resistance factor F_{ori} for rectangle wire is

$$F_{\mathrm{ori}} = \Delta\varsigma + \frac{4p^3 - 4p - 3k + 3k(2p+k)^2}{6(p+k)}\Delta\xi \tag{C.23}$$

The square shape wire winding follows the similar process except that the height of the rectangle wire h_{w0} is replaced by the height of the square d_{w}

$$h_{\mathrm{w0}} = d_{\mathrm{w}} \tag{C.24}$$

The calculated ac resistance factor F_{ori} is with the same form.

With the equivalent thickness transformation from the diameter d_{i} to equivalent d_{w} by (3.6), F_{ori} is also applicable for the round wire partial layer windings.

Appendix A. Appendix

Appendix B

Bibliography

References

[1] W. G. Hurley and W. H. Wölfle, *Transformers and inductors for power electronics: theory, design and applications*. West Sussex, UK: John Wiley & Sons, 2013.

[2] C. W. T. McLyman, *Transformer and inductor design handbook*. New York, NY, USA: Marcel Dekker, Inc., 2009.

[3] V. C. Valchev and A. Van den Bossche, *Inductors and transformers for power electronics*. Boca Raton, FL, USA: CRC Press, 2005.

[4] R. De Doncker, D. Divan, and M. Kheraluwala, "A three-phase soft-switched high-power-density dc/dc converter for high-power applications," *IEEE Trans. Ind. Appl.*, vol. 27, no. 1, pp. 63–73, Jan. 1991.

[5] Y. Guan, Y. Wang, D. Xu, and W. Wang, "A 1 MHz half-bridge resonant dc/dc converter based on GaN fets and planar magnetics," *IEEE Trans. Power Electron.*, vol. 32, no. 4, pp. 2876–2891, Apr. 2017.

[6] Y. Shen, H. Wang, Z. Shen, Y. Yang, and F. Blaabjerg, "A 1-MHz series resonant dc–dc converter with a dual-mode rectifier for pv microinverters," *IEEE Trans. Power Electron.*, vol. 34, no. 7, pp. 6544–6564, Jul. 2018.

[7] T. C. Neugebauer, J. W. Phinney, and D. J. Perreault, "Filters and components with inductance cancellation," *IEEE Trans. Ind. Appl.*, vol. 40, no. 2, pp. 483–491, Mar. 2004.

[8] R. S. Balog and P. T. Krein, "Coupled-inductor filter: A basic filter building block," *IEEE Trans. Power Electron.*, vol. 28, no. 1, pp. 537–546, Jan. 2013.

[9] Z. Ouyang and M. A. E. Andersen, "Overview of planar magnetic technology —fundamental properties," *IEEE Trans. Power Electron.*, vol. 29, no. 9, pp. 4888–4900, Sep. 2014.

[10] R. Shafaei, M. Ordonez, and M. A. Saket, "Three-dimensional frequency-dependent thermal model for planar transformers in LLC resonant converters," *IEEE Trans. Power Electron.*, vol. 34, no. 5, pp. 4641–4655, May 2018.

[11] B. Li, Q. Li, and F. C. Lee, "High-frequency PCB winding transformer with integrated inductors for a bi-directional resonant converter," *IEEE Trans. Power Electron.*, vol. 34, no. 7, pp. 6123–6135, Jul. 2019.

[12] M. Chen, S. Chakraborty, and D. J. Perreault, "Multitrack power factor correction architecture," *IEEE Trans. Power Electron.*, vol. 34, no. 3, pp. 2454–2466, Mar. 2019.

[13] W. X. Zhong, X. Liu, and S. Y. R. Hui, "A novel single-layer winding array and receiver coil structure for contactless battery charging systems with free-positioning and localized charging features," *IEEE Trans. Ind. Electron.*, vol. 58, no. 9, pp. 4136–4144, Sep. 2011.

[14] S. Li and C. C. Mi, "Wireless power transfer for electric vehicle applications," *IEEE Trans. Emerg. Sel. Topics Power Electron.*, vol. 3, no. 1, pp. 4–17, Mar. 2015.

[15] C. O. Mathúna, N. Wang, S. Kulkarni, and S. Roy, "Review of integrated magnetics for power supply on chip (PwrSoC)," *IEEE Trans. Power Electron.*, vol. 27, no. 11, pp. 4799–4816, Nov. 2012.

[16] F. C. Lee and Q. Li, "High-frequency integrated point-of-load converters: Overview," *IEEE Trans. Power Electron.*, vol. 28, no. 9, pp. 4127–4136, Sep. 2013.

[17] D. J. Perreault, J. Hu, J. M. Rivas, Y. Han, O. Leitermann, R. C. N. Pilawa-Podgurski, A. Sagneri, and C. R. Sullivan, "Opportunities and challenges in very high frequency power conversion," in *Proc. IEEE APEC Exposit.*, Feb. 2009, pp. 1–14.

[18] A. J. Hanson, J. A. Belk, S. Lim, C. R. Sullivan, and D. J. Perreault, "Measurements and performance factor comparisons of magnetic materials at high frequency," *IEEE Trans. Power Electron.*, vol. 31, no. 11, pp. 7909–7925, Nov. 2016.

[19] *Military Handbook: Reliability Prediction of Electronic Equipment*, Standard MIL-HDBK-217F Std., Dec. 1991.

[20] S. Yang, A. Bryant, P. Mawby, D. Xiang, L. Ran, and P. Tavner, "An industry-based survey of reliability in power electronic converters," *IEEE Trans. Ind. Appl.*, vol. 47, no. 3, pp. 1441–1451, May 2011.

[21] Micrometals, "Power conversion & line filter applications," https://www.micrometals.com, Tech. Rep., 2007.

[22] T. Matsmura, K. Nagayama, S. Hagimura, and M. Higaki, "Long term reliability of iron-based amorphous alloy cores for oil-immersed transformer," *IEEE Trans. Magn.*, vol. 26, no. 5, pp. 1993–1995, Sep. 1990.

[23] Micrometals, "Core loss increase due to thermal aging in iron powder cores," https://www.micrometals.com, Tech. Rep., 2007.

[24] Manz Electronic Systeme, "HTC iron powder cores: Thermal aging problems of iron powder cores," https://www.manz−electronic.com, Tech. Rep., 2019.

[25] CoilCraft, "Notes on thermal aging in inductor cores," https://www.coilcraft.com/pdfs/Doc1192_Notes_on_thermal_aging.pdf, Tech. Rep., 2014.

[26] S. S. Gorelik, B. E. Levin, L. M. Letyuk, and A. P. Nikol'skii, "Mechanism of aging in magnesium-manganese-zinc ferrite," *Soviet Phys. J.*, vol. 10, no. 7, p. 14, Jul. 1967.

[27] TDK Corporation, "Ferrite for telecommunication summary," Tech. Rep., Apr. 2011.

[28] C. A. Stergiou and V. Zaspalis, "Cobalt-induced performance instabilities of Mn–Zn ferrite cores," *IEEE Trans. Magn.*, vol. 54, no. 8, pp. 1–8, Aug. 2018.

[29] M. de Graaf, L. Dortmans, and A. Shpilman, "Mechanical reliability of ferrite cores used in inductive components," in *Proc. :Elec. Electron. Insul. Conf. Elec. Manufacturing Coil Winding Conf*, Sep. 1995, pp. 485–488.

[30] M. Donners, "Fracture of MnZn ferrites," Ph.D. dissertation, Eindhoven, The Netherlands: Technische Universiteit Eindhoven, 1999.

[31] Ferroxcube, "Gluing of ferrite cores: Application note," https://www.ferroxcube.com, Tech. Rep., Apr. 2002.

[32] S. Murray, C. Hillman, and M. Pecht, "Environmental aging and deadhesion of polyimide dielectric films," *J. Electron. Packag.*, vol. 126, no. 3, pp. 390–397, Oct. 2004.

[33] Z. Chun, "A study of polyimide thin films-physical aging and plasticization behaviors," Ph.D. dissertation, Singapore: National University of Singapore, 2003.

[34] G. C. Montanari and L. Simoni, "Aging phenomenology and modeling," *IEEE Trans. Electr. Insul.*, vol. 28, no. 5, pp. 755–776, Oct. 1993.

[35] S. Akbari, A. Lövberg, P.-E. Tegehall, K. Brinkfeldt, and D. Andersson, "Effect of PCB cracks on thermal cycling reliability of passive microelectronic components with single-grained solder joints," *Microelectron. Reliab.*, vol. 93, pp. 61–71, Jan. 2019.

[36] C.-Y. Huang, M.-S. Li, S.-Y. Huang, C.-I. Chang, and M.-H. Huang, "Material characterization and failure analysis for microelectronics assembly processes," in *Wide Spectra Quality Ctrl.* IntechOpen, 2011.

[37] S. Zhan, M. H. Azarian, and M. Pecht, "Reliability of printed circuit boards processed using no-clean flux technology in temperature–humidity–bias conditions," *IEEE Trans. Device Mater. Rel.*, vol. 8, no. 2, pp. 426–434, Jun. 2008.

[38] P. F. Fuchs, G. Pinter, and T. Krivec, "Design independent lifetime assessment method for PCBs under low cycle fatigue loading conditions," *Proc. Int. Conf. Therm. Mech. Multi-Physics Simul. Exp. Microelectron. Microsystems*, pp. 4–8, Apr. 2014.

[39] A. White, "The desired properties and their effect on the life history of insulating papers used in a fluid-filled power transformer," in *Proc. IEE Colloq. Assmnt. Degradation Trafo. Insul. Sys.*, Dec. 1991, pp. 4/1–4/4.

[40] X. Zhang, E. Gockenbach, V. Wasserberg, and H. Borsi, "Estimation of the lifetime of the electrical components in distribution networks," *IEEE Trans. Power Del.*, vol. 22, no. 1, pp. 515–522, Jan. 2007.

[41] A. van Schijndel, "Power transformer reliability modelling," Ph.D. dissertation, Eindhoven, Netherlands: Eindhoven University of Technology, 2010.

[42] Q. Zhong, "Power transformer end-of-life modelling: Linking statistics with physical ageing," Ph.D. dissertation, Manchester, UK: The University of Manchester, 2012.

[43] IEEE Power & Energy Society, *IEEE Guide for Loading Mineral-Oil-Immersed Transformers and Step-Voltage Regulators*, IEEE Std., Mar. 2012.

[44] J. K. Nelson, S. Azizi-Ghannad, and H. Li, "Theory and application of dynamic aging for life estimation in machine insulation," *IEEE Trans. Dielectr. Electr. Insul.*, vol. 7, no. 6, pp. 773–782, Dec. 2000.

[45] M. Kaufhold, H. Aninger, M. Berth, J. Speck, and M. Eberhardt, "Electrical stress and failure mechanism of the winding insulation in PWM-inverter-fed low-voltage induction motors," *IEEE Trans. Ind. Electron.*, vol. 47, no. 2, pp. 396–402, Apr. 2000.

[46] M. Kaufhold, K. Schafer, K. Bauer, A. Bethge, and J. Risse, "Interface phenomena and in stator and winding insulation-challenges and in design and diagnosis and service and experience," *IEEE Electr. Insul. Mag.*, vol. 18, no. 2, pp. 27–36, Mar. 2002.

[47] N. Lahoud, J. Faucher, D. Malec, and P. Maussion, "Electrical aging of the insulation of low-voltage machines: Model definition and test with the design of experiments," *IEEE Trans. Ind. Electron.*, vol. 60, no. 9, pp. 4147–4155, Feb. 2013.

[48] P. Mancinelli, S. Stagnitta, and A. Cavallini, "Lifetime analysis of an automotive electrical motor with hairpin wound stator," in *Proc. IEEE Conf. Electrical Insul. Dielectric Phenomena*, Oct. 2016, pp. 877–880.

[49] C. Sciascera, M. Galea, P. Giangrande, and C. Gerada, "Lifetime consumption and degradation analysis of the winding insulation of electrical machines," in *Proc. IET Int. Conf. Power Electron. Machines Drives*, Apr. 2016, pp. 1–5.

[50] H. Wang, M. Liserre, F. Blaabjerg, P. De Place Rimmen, J. B. Jacobsen, T. Kvisgaard, and J. Landkildehus, "Transitioning to physics-of-failure as a reliability driver in power electronics," *IEEE J. Emerg. Sel. Top. Power Electron.*, vol. 2, no. 1, pp. 97–114, Mar. 2014.

[51] Z. Shen, Q. Wang, Y. Shen, and H. Wang, "First observations in degradation testing of planar magnetics," in *Proc. IEEE APEC Exposit.*, Mar. 2019, pp. 1436–1443.

[52] Pulse Electronics, "Introduction to transforemr and magnetics," https://www.networking.pulseelectronics.com/, Tech. Rep., 2018.

[53] M. Mogorovic and D. Dujic, "100 kW, 10 kHz medium-frequency transformer design optimization and experimental verification," *IEEE Trans. Power Electron.*, vol. 34, no. 2, pp. 1696–1708, Feb. 2019.

[54] M. A. Saket, N. Shafiei, and M. Ordonez, "LLC converters with planar transformers: issues and mitigation," *IEEE Trans. Power Electron.*, vol. 32, no. 6, pp. 4524–4542, Jun. 2017.

[55] W. T. Duerdoth, "Equivalent capacitances of transformer windings," *Wireless Eng.*, vol. 23, no. 161-167, Jun. 1946.

[56] E. Snellinq, *SoftFerrites: Properties and Applications*. London, U.K.: Iliffe books Ltd, 1988.

[57] F. Blache, J. P. Keradec, and B. Cogitore, "Stray capacitances of two winding transformers: equivalent circuit, measurements, calculation and lowering," in *Proc. IEEE Ind. Appl. Soc. Ann. Meeting*, vol. 2, Oct. 1994, pp. 1211–1217.

[58] W. Shen, "Design of high-density transformers for high-frequency high-power converters," Ph.D. dissertation, Blacksburg, VA, USA: Virginia Tech, 2006.

[59] T. Duerbaum and G. Sauerlaender, "Energy based capacitance model for magnetic devices," in *Proc. IEEE APEC Exposit.*, Mar. 2001, pp. 109–115.

[60] K. Nguyen-Duy, Z. Ouyang, A. Knott, and M. A. E. Andersen, "Minimization of the transformer inter-winding parasitic capacitance for modular stacking power supply applications," in *Proc. Eur. Conf. Power Electron. Appl.*, Aug. 2014, pp. 1–10.

[61] M. A. Saket, M. Ordonez, and N. Shafiei, "Planar transformers with near-zero common-mode noise for flyback and forward converters," *IEEE Trans. Power Electron.*, vol. 33, no. 2, pp. 1554–1571, Feb. 2018.

[62] D. Leuenberger and J. Biela, "Accurate and computationally efficient modeling of flyback transformer parasitics and their influence on converter losses," in *Proc. Eur. Conf. Power Electron. Appl.*, Sep. 2015, pp. 1–10.

[63] J. Biela and J. W. Kolar, "Using transformer parasitics for resonant converters-a review of the calculation of the stray capacitance of transformers," *IEEE Trans. Ind. Appl.*, vol. 44, no. 1, pp. 223– 233, Jan. 2008.

[64] A. Massarini and M. K. Kazimierczuk, "Self-capacitance of inductors," *IEEE Trans. Power Electron.*, vol. 12, no. 4, pp. 671–676, Jul. 1997.

[65] G. Grandi, M. K. Kazimierczuk, A. Massarini, and U. Reggiani, "Stray capacitances of single-layer solenoid air-core inductors," *IEEE Trans. Ind. Appl.*, vol. 35, no. 5, pp. 1162–1168, Sep. 1999.

[66] M. Kovacic, Z. Hanic, S. Stipetic, S. Krishnamurthy, and D. Zarko, "Analytical wideband model of a common-mode choke," *IEEE Trans. Power Electron.*, vol. 27, no. 7, pp. 3173–3185, Jul. 2012.

[67] C. P. Steinmetz, "On the law of hysteresis," *Trans. Am. Inst. Electr. Eng.*, vol. IX, no. 1, pp. 1–64, Jan. 1892.

[68] J. Reinert, A. Brockmeyer, and R. W. A. A. D. Doncker, "Calculation of losses in ferro- and ferrimagnetic materials based on the modified steinmetz equation," *IEEE Trans. Ind. Appl.*, vol. 37, no. 4, pp. 1055–1061, Jul. 2001.

[69] J. Li, T. Abdallah, and C. R. Sullivan, "Improved calculation of core loss with nonsinusoidal waveforms," in *Proc. IEEE Ind. Appl. Conf.*, vol. 4, Sep. 2001, pp. 2203–2210 vol.4.

[70] K. Venkatachalam, C. R. Sullivan, T. Abdallah, and H. Tacca, "Accurate prediction of ferrite core loss with nonsinusoidal waveforms using only steinmetz parameters," in *Proc. IEEE Wksp. Comp. Power Electron.*, Jun. 2002, pp. 36–41.

[71] A. V. den Bossche, V. C. Valchev, and G. B. Georgiev, "Measurement and loss model of ferrites with non-sinusoidal waveforms," in *Proc. IEEE Annual Power Electron. Spclst. Conf.*, vol. 6, Jun. 2004, pp. 4814–4818 Vol.6.

[72] D. Lin, P. Zhou, W. N. Fu, Z. Badics, and Z. J. Cendes, "A dynamic core loss model for soft ferromagnetic and power ferrite materials in transient finite element analysis," *IEEE Trans. Magn.*, vol. 40, no. 2, pp. 1318–1321, Mar. 2004.

[73] W. Shen, F. Wang, D. Boroyevich, and C. W. Tipton, "Loss characterization and calculation of nanocrystalline cores for high-frequency magnetics applications," in *Proc. IEEE APEC Exposit.*, Feb. 2007, pp. 90–96.

[74] K. Chen, "Iron-loss simulation of laminated steels based on expanded generalized steinmetz equation," in *Proc. Asia-Pacific Power Energy Eng. Conf.*, Mar. 2009, pp. 1–3.

[75] M. Mu, Q. Li, D. J. Gilham, F. C. Lee, and K. D. T. Ngo, "New core loss measurement method for high-frequency magnetic materials," *IEEE Trans. Power Electron.*, vol. 29, no. 8, pp. 4374–4381, Aug. 2014.

[76] Z. Shen, Q. Wang, and H. Wang, "Degradation analysis of planar magnetics," in *Proc. IEEE APEC Exposit.*, Mar. accepted, 2020.

[77] P. Dowell, "Effects of eddy currents in transformer windings," *Proc. Inst. Electr. Eng.*, vol. 113, no. 8, pp. 1387–1394, Aug. 1966.

[78] Z. Shen, H. Wang, Y. Shen, Z. Qin, and F. Blaabjerg, "An improved stray capacitance model for inductors," *IEEE Trans. Power Electron.*, vol. 34, no. 11, pp. 11 153–11 170, Nov. 2019.

[79] Z. Shen and H. Wang, "Parasitics of orthocyclic windings in inductors and transformers," *IEEE Trans. Power Electron.*, under review, 2020.

[80] X. Liu, Y. Wang, J. Zhu, Y. Guo, G. Lei, and C. Liu, "Calculation of capacitance in high-frequency transformer windings," *IEEE Trans. Magn.*, vol. 52, no. 7, pp. 1–4, Jul. 2016.

[81] R. Chattopadhyay, M. A. Juds, P. R. Ohodnicki, and S. Bhattacharya, "Modelling, design and analysis of three limb high frequency transformer including transformer parasitics, for SiC mosfet based three port DAB," in *Proc. Annu. Conf. IEEE Ind. Electron. Soc.*, Oct. 2016, pp. 4181–4186.

[82] W. Tan, "Modeling and design of passive planar components for EMI filters," Ph.D. dissertation, Lille, France: Ecole Centrale de Lille, 2012.

[83] Z. Shen, H. Wang, Y. Shen, Z. Qin, and F. Blaabjerg, "Winding design of series ac inductor for dual active bridge converters," in *Proc. IEEE APEC Exposit.*, Mar. 2018, pp. 565–570.

[84] J. Koch, "Berechnung der kapazität von spulen, insbesondere in schalenkernen," *Valvo Berichte*, vol. 14, no. 3, pp. 99–119, 1968.

[85] M. Aghaei and S. Kaboli, "On the effect of disorder on stray capacitance of transformer winding in high-voltage power supplies," *IEEE Trans. Ind. Electron.*, vol. 64, no. 5, pp. 3608–3618, May 2017.

[86] W. H. Hayt and J. A. Buck, *Engineering electromagnetics*. New York City, NY, USA: McGraw-Hill, 2001.

[87] W. Schroder, "Berechnung der eigenschwingungen der doppellagigen langen spule," *Arch. Elektrotechnik*, vol. Band XI, Heft 6, pp. 203–229, 1922.

[88] L. Dalessandro, F. da Silveira Cavalcante, and J. W. Kolar, "Self-capacitance of high-voltage transformers," *IEEE Trans. Power Electron.*, vol. 22, no. 5, pp. 2081–2092, Sep. 2007.

[89] Ferroxcube, "Soft ferrites and accessories," http://www.ferroxcube.home.pl/appl/info/HB2009.pdf, Tech. Rep., Sep. 2008.

[90] A. Hoke and C. Sullivan, "An improved two-dimensional numerical modeling method for E-core transformers," in *Proc. IEEE APEC Exposit.*, Aug. 2002, pp. 151–157.

[91] H. Zuhrt, "Simple approximate formulas for the self capacitance of multi-layer coils," *Elekrotech. Zeitschrift*, vol. 55, pp. 662–665, Jul. 1934.

[92] D. Meeker, *Finite Element Method Magnetics (FEMM)*. Version 4.2, Jan. 2016.

[93] R. Prieto, L. Ostergaard, J. A. Cobos, and J. Uceda, "Axisymmetric modeling of 3D magnetic components," in *Proc. IEEE APEC Exposit.*, Mar. 1999, pp. 213–219.

[94] H. Y. Lu, J. G. Zhu, and S. Y. R. Hui, "Experimental determination of stray capacitances in high frequency transformers," *IEEE Trans. Power Electron.*, vol. 18, no. 5, pp. 1105–1112, Sep. 2003.

[95] C. Cuellar, W. Tan, X. Margueron, A. Benabou, and N. Idir, "Measurement method of the complex magnetic permeability of ferrites in high frequency," in *Proc. IEEE Int. Inst. Meas. Tech. Conf.*, May 2012, pp. 63–68.

[96] Z. Shen, Z. Li, L. Jin, and H. Wang, "An ac resistance optimization method applicable for inductor and transformer windings with full layers and partial layers," in *Proc. IEEE APEC Exposit.*, Mar. 2017, pp. 2542–2548.

[97] Z. Shen, Z. Li, and L. J. H. Wang, "An approximation model of ac resistance for inductor and transformer windings with partial layers," *IEEJ Trans. Ind Appl.*, under review, 2020.

[98] W. Hurley, E. Gath, and J. Breslin, "Optimizing the AC resistance of multilayer transformer windings with arbitrary current waveforms," *IEEE Trans. Power Electron.*, vol. 15, no. 2, pp. 369–376, Mar. 2000.

[99] M. K. Kazimierczuk, *High-frequency magnetic components*. West Sussex, UK: John Wiley & Sons, 2009.

[100] M. Kaymak, Z. Shen, and R. W. D. Doncker, "Comparison of analytical methods for calculating the AC resistance and leakage inductance of medium-frequency transformers," in *Proc. IEEE Wksh. Contr. Modeling Power Electron.*, Jun. 2016, pp. 1–8.

[101] J. Lammeraner and M. Štafl, *Eddy currents*. London, U.K.: Iliffe, 1966.

[102] J. Ferreira, "Appropriate modelling of conductive losses in the design of magnetic components," in *Proc. IEEE Power Electron. Spclst. Conf.*, Jun. 1990, pp. 780–785.

[103] G. Dimitrakakis, E. Tatakis, and E. Rikos, "A new model for the determination of copper losses in transformer windings with arbitrary conductor distribution under high frequency sinusoidal excitation," in *Proc. Eur. Conf. Power Electron. Appl.*, 2007, pp. 1–10.

[104] C. Sullivan, "Optimal choice for number of strands in a litz-wire transformer winding," *IEEE Trans. Power Electron.*, vol. 14, no. 2, pp. 283–291, Mar. 1999.

[105] R. Wojda and M. K. Kazimierczuk, "Winding resistance of litz-wire and multi-strand inductors," *IET Power Electron.*, vol. 5, no. 2, pp. 257–268, Feb. 2012.

[106] E. Barrios, A. Ursua, L. Marroyo, and P. Sanchis, "Analytical design methodology for litz-wired high-frequency power transformers," *IEEE Trans. Ind. Electron.*, vol. 62, no. 4, pp. 2103–2113, Apr. 2015.

[107] C. Sullivan, "Computationally efficient winding loss calculation with multiple windings, arbitrary waveforms, and two-dimensional or three-dimensional field geometry," *IEEE Trans. Power Electron.*, vol. 16, no. 1, pp. 142–150, Jan. 2001.

[108] X. Nan and C. R. Sullivan, "Simplified high-accuracy calculation of eddy-current loss in round-wire windings," in *Proc. IEEE Power Electron. Spclst. Conf.*, vol. 2, Jun. 2004, pp. 873–879.

[109] M. Bahmani, T. Thiringer, and H. Ortega, "An accurate pseudoempirical model of winding loss calculation in HF foil and round conductors in switchmode magnetics," *IEEE Trans. Power Electron.*, vol. 29, no. 8, pp. 4231–4246, Aug. 2014.

[110] D. Leuenberger and J. Biela, "Semi-numerical method for calculation of loss in foil windings exposed to an air-gap field," *IEEJ J. Ind Appl.*, vol. 4, no. 4, pp. 301–309, Jul. 2015.

[111] D. Whitman and M. K. Kazimierczuk, "An analytical correction to Dowell's equation for inductor and transformer winding losses using cylindrical coordinates," *IEEE Trans. Power Electron.*, vol. 34, no. 11, pp. 10 425–10 432, Nov. 2019.

[112] N. H. Kutkut, "A simple technique to evaluate winding losses including two-dimensional edge effects," *IEEE Trans. Power Electron.*, vol. 13, no. 5, pp. 950–958, Sep. 1998.

[113] A. Reatti and M. Kazimierczuk, "Comparison of various methods for calculating the AC resistance of inductors," *IEEE Trans. Magn.*, vol. 38, no. 3, pp. 1512–1518, May 2002.

[114] J. Ferreira, "Improved analytical modeling of conductive losses in magnetic components," *IEEE Trans. Power Electron.*, vol. 9, no. 1, pp. 127–131, Jan. 1994.

[115] X. Nan and C. R. Sullivan, "An improved calculation of proximity-effect loss in high-frequency windings of round conductors," in *Proc. IEEE Power Electro. Spclst. Conf.*, vol. 2, Jun. 2003, pp. 853–860.

[116] R. Wojda and M. Kazimierczuk, "Analytical optimization of solid–round-wire windings," *IEEE Trans. Ind. Electron.*, vol. 60, no. 3, pp. 1033–1041, Mar. 2013.

[117] N. Mohan, T. M. Undeland, and W. P. Robbins, *Power electronics: converters, applications, and design*. Hoboken, NJ, USA: John Wiley & Sons, 2007.

[118] Z. Ouyang, J. Zhang, and W. G. Hurley, "Calculation of leakage inductance for high-frequency transformers," *IEEE Trans. Power Electron.*, vol. 30, no. 10, pp. 5769–5775, Oct. 2015.

[119] M. A. Bahmani and T. Thiringer, "Accurate evaluation of leakage inductance in high-frequency transformers using an improved frequency-dependent expression," *IEEE Trans. Power Electron.*, vol. 30, no. 10, pp. 5738–5745, Oct. 2015.

[120] I. Villar, "Multiphysical characterization of medium-frequency power electronic transformers," Ph.D. dissertation, Lausanne, Switzerland: École Polytechnique Fédérale de Lausanne, 2010.

[121] M. Mogorovic and D. Dujic, "Medium frequency transformer leakage inductance modeling and experimental verification," in *Proc. IEEE ECCE*, Sep. 2017, pp. 419– 424.

[122] Z. Shen, Y. Shen, B. Liu, and H. Wang, "Thermal coupling and network modeling for planar transformers," in *IEEE ECCE*, Sep. 2018, pp. 3527–3533.

[123] Z. Ouyang, O. C. Thomsen, and M. A. E. Andersen, "Optimal design and tradeoff analysis of planar transformer in high-power dc-dc converters," *IEEE Trans. Ind. Electron.*, vol. 59, no. 7, pp. 2800–2810, Jul. 2012.

[124] A. Lewaiter and B. Ackermann, "A thermal model for planar transformers," in *Proc. IEEE Int. Conf. Power Electron. Drive Sys.*, vol. 2, Oct. 2001, pp. 669–673.

[125] I. Villar, U. Viscarret, I. Etxeberria-Otadui, and A. Rufer, "Transient thermal model of a medium frequency power transformer," in *Proc. Annual Conf. IEEE Ind. Electron.*, Nov. 2008, pp. 1033–1038.

[126] P. Svasta, C. Ionescu, N. D. Codreanu, and V. Golumbeanu, "Thermal characterisation of planar transformers," in *Proc. Int. Spring Sem. Electron. Technol.: Meeting Challenges Electron. Technol. Progress*, vol. 2, May 2004, pp. 280–286.

[127] C. Buccella, C. Cecati, and F. de Monte, "Investigation about the electro-thermal behavior of high power/high frequency planar transformers," in *Proc. IEEE Int. Symp. Ind. Electron.*, Jun. 2008, pp. 374–379.

[128] L. A. R. Tria, D. Zhang, and J. E. Fletcher, "Electromagnetic and thermal characterisation of PCB planar transformer," in *Proc. IEEE Int. Conf. Power Electron. Drive Sys.*, Jun. 2015, pp. 1024–1028.

[129] C. Ropoteanu, P. Svasta, and C. Ionescu, "Electro-thermal simulation study of different core shape planar transformer," in *Proc. IEEE Int. Symp. Design Tech. Electron. Pkg.*, Oct. 2016, pp. 209–212.

[130] R. Bakri, J. S. N. Teu, X. Margueron, P. L. Moigne, and N. Idir, "Planar transformer equivalent thermal resistance variation with ambient temperature and power losses," in *Proc. Eur. Conf. Power Electron. Appl.*, Sep. 2016, pp. 1–9.

[131] M. Fu, C. Fei, Y. Yang, Q. Li, and F. Lee, "Optimal design of planar magnetic components for a two-stage GaN-based DC/DC converter," *IEEE Trans. Power Electron.*, vol. 34, no. 4, pp. 3329–3338, Apr. 2018.

[132] A. Buettner, A. Nysveen, and M. Hernes, "Thermal loss measurements of high frequency planar transformers," in *Proc. Eur. Conf. Power Electron. Appl.*, Sep. 2009, pp. 1–7.

[133] K. Gorecki and K. Gorski, "Compact thermal model of planar transformers," in *Proc. Int. Conf. Mixed Desg. Integ. Ckt. Sys.*, Jun. 2017, pp. 345–350.

[134] K. Gorecki and K. Gorski, "Non-linear thermal model of planar transformers," in *Proc. Eur. Microelectron. Pkg. Conf. Exhibition*, Sep. 2017, pp. 1–5.

[135] J. Muehlethaler, "Modeling and multi-objective optimization of inductive power components," Ph.D. dissertation, Zurich, Switzerland: ETH Zurich, 2012.

[136] Y. A. Cengel, R. H. Turner, J. M. Cimbala, and M. Kanoglu, *Fundamentals of thermal-fluid sciences*. New York, NY, USA: McGraw-Hill, 2008.

[137] Y. Shen, A. Chub, H. Wang, D. Vinnikov, E. Liivik, and F. Blaabjerg, "Wear-out failure analysis of an impedance-source PV microinverter based on system-level electro-thermal modeling," *IEEE Trans. Ind. Electron.*, vol. 66, no. 5, pp. 3914–3927, May 2018.

[138] X. Hu, S. Lin, S. Stanton, and W. Lian, "A foster network thermal model for HEV/EV battery modeling," *IEEE Trans. Ind. Appl.*, vol. 47, no. 4, pp. 1692–1699, Jul. 2011.

[139] D. T. Billings and R. P. Stout, "Using linear superposition to solve multiple heat source transient thermal problems," in *Proc. ASME 2007 InterPACK Conf. collocated with ASME/JSME 2007 Thermal Eng. Heat Transfer Summer Conf.*, no. 791-799, Jul. 2007, pp. 791–799.

[140] E. Kuffel, W. Zaengl, and J. Kuffel, *High Voltage Engineering: Fundamentals*. Oxford, UK: Newnes, 2000.

[141] International Electrotechnical Commission, *IEC Standard 60270. High-voltage test techniques - Partial discharge measurements*, IEC Std., 2000.

ISSN (online): 2446-1636
ISBN (online): 978-87-7210-600-7

AALBORG UNIVERSITY PRESS